FIGNL1 AAA+ ATPase remodels RAD51 and DMC1 filaments in pre-meiotic DNA replication and meiotic recombination

Masaru Ito[1]*, Asako Furukohri[1], Kenichiro Matsuzaki[1, 2], Yurika Fujita[1], Atsushi Toyoda[3], and Akira Shinohara[1]*

[1]Institute for Protein Research, Osaka University, Suita, Osaka 565-0871, Japan
[2]Department of Advanced Bioscience, Graduate School of Agriculture, Kindai University, Nara, Nara 631-8505, Japan
[3]Advanced Genomics Center, National Institute of Genetics, Mishima, Shizuoka 411-8540, Japan

Running title: Suppression of RAD51/DMC1 assembly by FIGNL1

Keywords: meiosis; homologous recombination; FIGNL1; RAD51; DMC1

*Corresponding author:
Masaru Ito; msrito2@protein.osaka-u.ac.jp
Akira Shinohara; ashino@protein.osaka-u.ac.jp

Lead contact:
Akira Shinohara
Institute for Protein Research, Osaka University,
3-2 Yamadaoka, Suita, Osaka 565-0871 JAPAN
Phone: 81-6-6879-8624
FAX: 81-6-6879-8626
E-mail: ashino@protein.osaka-u.ac.jp
ORCID: 0000-0003-4207-8247

Abstract

The formation of RAD51/DMC1 filaments on single-stranded (ss)DNAs essential for homology search and strand exchange in DNA double-strand break (DSB) repair is tightly regulated. FIGNL1 AAA+++ ATPase controls RAD51-mediated recombination in human cells. However, its role in gametogenesis remains unsolved. Here, we characterized a germ-line-specific conditional knockout (cKO) mouse of *FIGNL1*. *Fignl1* cKO male mice showed defective chromosome synapsis and impaired meiotic DSB repair with the accumulation of RAD51/DMC1 on meiotic chromosomes, supporting a positive role of FIGNL1 in homologous recombination at a post-assembly stage of RAD51/DMC1 filaments. *Fignl1* cKO spermatocytes also accumulate RAD51/DMC1 on chromosomes in pre-meiotic S-phase. These RAD51/DMC1 assemblies are independent of meiotic DSB formation. We also showed that purified FIGNL1 dismantles RAD51 filament on double-stranded (ds)DNA as well as ssDNA. These results suggest an additional role of FIGNL1 in limiting the non-productive assembly of RAD51/DMC1 on native dsDNAs during pre-meiotic S-phase and meiotic prophase I. (149 words)

Introduction

RAD51 is a central player in homologous recombination in eukaryotes by catalyzing homology-directed repair such as the repair of DNA double-strand breaks (DSBs) in both somatic and meiotic cells. RAD51 also plays a role in S-phase for the protection of stalled DNA replication forks [1, 2], which is independent of RAD51-mediated strand exchange [3, 4]. As an active form for homology search and strand exchange, multiple protomers of RAD51 bind to single-stranded (ss)DNAs in the presence of ATP to form a right-handed helical filament termed RAD51 nucleofilament, in which ssDNAs are extended 1.5-2.0-fold relative to the B-form DNA [5-8]. RAD51 nucleofilament is highly dynamic; its assembly and disassembly are controlled by multiple proteins/complexes. The RAD51 mediator promotes the assembly of RAD51 nucleofilament on the ssDNAs coated with an ssDNA-binding protein, RPA (Replication protein A), which hampers RAD51 binding to the ssDNA. The RAD51 mediator in humans includes BRCA2(-PALB2-DSS1) [9], BRCA1-BARD1 [10], RAD52 [11-13], SWI5-SFR1/MEI5 [14, 15], and five RAD51 paralogs (RAD51B, -C, -D, XRCC2, and -3) in vertebrates including humans. The RAD51 paralogs form two distinct complexes: RAD51C-XRCC3 and RAD51B-RAD51C-RAD51D-XRCC2 [16]. SWSAP1 is a distinct member of a RAD51 paralog [17-19], which forms a complex with SWS1 and SPIDR. At the post-assembly stage, RAD51 nucleofilament works together with the SWI2/SNF2 family, RAD54 and RAD54B [20, 21], and RAD51AP1 [22-24] for efficient homology search and strand exchange with a target double-stranded DNA (dsDNA) for the formation of displacement (D)-loop. RAD51-mediated strand invasion provides a template for DNA synthesis for further processing of the intermediates for the completion of the repair.

The dynamics of the RAD51 filament are also negatively regulated by proteins that disassemble the filament. Various DNA helicases are involved in the disassembly of RAD51 filament, which include BLM [25-27], FANCJ [28], RECQ5 [29, 30], and FBH1 [31, 32] as well as a degenerate DNA helicase, PARI [33]. RAD51-mediated invasion intermediates are also remodeled by other DNA helicases such as WRN, RTEL1, FANCM, and RECQ1 [34]. RAD54 translocase also disassembles RAD51 from dsDNA in recombination intermediates [35]. The stabilization and destabilization of RAD51 filaments are associated with the choice of a homologous recombination pathway [36].

Meiosis is a specialized cell division that produces haploid gametes. Homologous recombination, specifically crossing-over, is essential for

85 chromosome segregation of homologous chromosomes during meiosis I. To
86 ensure the crossover (CO) formation in meiosis, highly programmed regulation is
87 implanted on the recombination pathway [37-39]. A meiosis-specific RAD51 cousin,
88 DMC1, is critical for homology search in meiotic recombination in many species
89 [40]. The cooperation of RAD51 and DMC1 promotes homology search between
90 homologous chromosomes rather than sister chromatids whose mechanism is
91 one big enigma in the field [41, 42]. RAD51/DMC1-mediated recombination requires
92 meiosis-specific proteins as well as proteins playing a role in somatic cells.
93 Knockout (KO) of the most of genes necessary for homologous recombination,
94 *Rad51* and RAD51 mediators (*Brca2*, *Rad51B*, *-C*, *-D*, *Xrcc2*, and *-3*), in mice
95 leads to embryonic lethality [43-49]. *Swsap1* (and *Sws1* and *Spidr*) KO mice are
96 viable but are sterile, with an exception of *Spidr* KO female mice being sub-fertile
97 [17, 50, 51]. Indeed, SWSAP1-SWS1-SPIDR is necessary for the efficient formation
98 of RAD51/DMC1 focus, which is a cytologically detectable immuno-stained
99 structure, in male meiosis [17, 50-52]. Like RAD51 mediators, KO mice of some
100 negative regulators such as BLM are also embryonically lethal [53] while *Rad54* KO
101 mice are viable and fertile [54].
102 A recently identified recombination regulator, FIGNL1, encodes an AAA+
103 ATPase which belongs to microtubule severing proteins including Katanin,
104 Spastin, and Fidgetin with an N-terminal microtubule-binding domain [55]. FIGNL1
105 was identified as a RAD51-interacting protein and is required for homologous
106 recombination in human somatic cells [56]. FIGNL1 knockdown does not affect
107 DSB-induced RAD51 focus formation [51, 56], suggesting its role in the post-RAD51
108 assembly step. Despite its positive role in homologous recombination, FIGNL1
109 functions as a negative regulator for RAD51 assembly. FIGNL1 depletion rescues
110 defective RAD51-focus formation in human cells depleted for SWSAP1 or SWS1,
111 but not for RAD51C [51]. Moreover, purified FIGNL1 promotes the dissociation of
112 RAD51 protein from ssDNAs, which is suppressed by SWSAP1 [51]. In *Arabidopsis*
113 *thaliana* meiosis, a mutant of *FIGL1*, FIGNL1 ortholog, as well as its partner, *FLIP*,
114 shows increased frequencies of COs during meiosis, indicating a role as an anti-
115 CO factor [57, 58]. The role of FIGL1-FLIP as the anti-CO factor is also seen in rice
116 meiosis [59, 60]. Importantly, the *figl1* mutation can suppress defective
117 RAD51/DMC1 focus formation in *brca2* mutant meiocytes, indicating antagonism
118 of FIGL with the RAD51 mediator [61]. These suggest that RAD51 mediators might
119 play a distinct function in different recombination pathways. Although FIGNL1
120 plays a role in homologous recombination by regulating the SWSAP1 complex in

121 somatic cells [51], it remains unknown how FIGNL1 regulates recombination and
122 works together with SWSAP1 during meiosis.
123 In this study, we analyzed the role of FIGNL1 in mice in meiosis, by
124 constructing a germ-cell specific conditional knockout (cKO) mouse and found
125 that *Fignl1* depletion in the testis led to defective spermatogenesis. Meiotic
126 chromosome spreads from *Fignl1* cKO spermatocytes showed a two-fold
127 increase in the numbers of RAD51 and DMC1 foci relative to controls, suggesting
128 the role of FIGNL1 in the post-assembly stage of not only RAD51 filament but
129 also DMC1 filament. This defective disassembly results in the impaired loading
130 of proteins necessary for CO formation. We also found that FIGNL1 suppresses
131 RAD51 and DMC1 assembly in pre-meiotic S-phase and early leptonema, which
132 are independent of meiotic DSB formation. Moreover, *Fignl1* cKO ameliorates
133 defective RAD51- and DMC1-focus formation in KO spermatocytes of *Swasp1,* a
134 RAD51/DMC1 mediator, supporting the antagonistic role of FIGNL1 to SWSAP1
135 in the assembly of both RAD51 and DMC1. Together, our study establishes a
136 dual role of FIGNL1 in mammalian male meiosis. The same conclusion was
137 obtained by Baudat's group by characterizing the *Fignl1* cKO as well as *Firrm*
138 cKO (FIRRM is a FIGNL1-interacting protein, accompanying paper).
139
140 **Results**
141 ***Fignl1* is essential for early mouse embryogenesis**
142 To determine the functions of FIGNL1 in mice, we created a conditional allele of
143 *Fignl1* gene, $Fignl1^{flox}$, in which the exon 3 encoding an open reading frame of
144 the full-length protein is flanked by the *loxP* sites (Fig. 1a) in C57BL/6 background.
145 A null allele of the gene, $Fignl1^{\Delta}$, was obtained by breeding with *CAG-Cre+* mice
146 that constitutively express Cre recombinase. $Fignl1^{\Delta/+}$ heterozygous mice grew
147 normally and did not show any apparent defects. Breeding between male and
148 female of $Fignl1^{\Delta/+}$ produced $Fignl1^{+/+}$ and $Fignl1^{\Delta/+}$ pups, but no $Fignl1^{\Delta/\Delta}$
149 homozygous pups (0/186 from 38 litters), showing that $Fignl1^{\Delta/\Delta}$ mice are not
150 viable. This is consistent with the reported lethality of *Fignl1* knockout (KO) mice
151 in the International Mouse Phenotyping Consortium (IMPC)
152 (https://www.mousephenotype.org). In a detailed analysis of different embryonic
153 stages by the breeding of heterozygous parents, we could not obtain $Fignl1^{\Delta/\Delta}$
154 homozygous embryo at both E7.5 and E13.5 stages (0/29 and 0/37, respectively),
155 showing very early lethality of mice homozygous for *Fignl1* deletion. Early
156 embryonic lethality in mice homozygous for the homologous recombination

157 genes has been reported; *Rad51* [49], *Brca2*, [62] and Rad51 paralogs (*Rad51B*, *-C*,
158 *-D*, *Xrcc2*, and *-3*) [43-48].
159
160 ***Fignl1* conditional knockout mice are defective in spermatogenesis**
161 To know the role of FIGNL1 in male meiosis, we generated *Fignl1*$^{flox/\Delta}$ mice
162 harboring a germ-line specific Cre recombinase gene, *Stra8-Cre*. The *Stra8-Cre*
163 gene ensured the expression of Cre not only in spermatocytes (meiotic cells) but
164 also in spermatogonia [63]. *Fignl1*$^{flox/\Delta}$ *Stra8-Cre*$^{+}$*,* hereafter *Fignl1* conditional
165 knockout *(*cKO), male mice were characterized for spermatogenesis. *Fignl1* cKO
166 adult male mice showed normal body weight without any morphological defects
167 but reduced sizes of the testis by ~50% relative to controls (*Fignl1*$^{+/+}$*, Fignl1*$^{flox/\Delta}$*,*
168 and *Fignl1*$^{+/+}$ *Stra8-Cre*$^{+}$), which is a characteristic of mutants with defective
169 spermatogenesis (Fig. 1b, c). Western blotting analysis confirmed decreased
170 amounts of FIGNL1 protein in whole testis extracts (Fig. 1d). The level of residual
171 FIGNL1 protein is consistent with the efficiency of Stra8-Cre-mediated excision
172 of *Fignl1*^{flox} allele estimated by the transmission of *Fignl1*$^{\Delta}$ allele from *Fignl1*$^{flox/+}$
173 *Stra8-Cre*$^{+}$ male mice (91.3%; 116/127). Sperm counts were ~6-fold lower in
174 *Fignl1* cKO relative to controls (Fig. 1e). Residual sperms in *Fignl1* cKO might
175 come from *Fignl1*$^{flox/\Delta}$ cells where Stra8-Cre recombinase failed excision of the
176 *Fignl1*^{flox} allele. Histological analysis showed that seminiferous tubules in *Fignl1*
177 cKO testes contained decreased numbers of late spermatocytes and spermatids
178 (Fig. 1f). These indicate a critical role of FIGNL1 in spermatogenesis. Consistent
179 with this, FIGNL1 expression was detected in PLZF-positive spermatogonia and
180 SYCP3-positive spermatocytes, but not in Sertoli cells and round spermatids
181 (Supplementary Fig. 1a).
182 To analyze meiotic defects in *Fignl1* cKO male mice, we prepared surface-
183 spread chromosomes of spermatocytes and immuno-stained for meiosis-specific
184 chromosomal proteins, SYCP3(Scp3) and SYCP1(Scp1), which are components
185 of lateral/axial elements and central region of the synaptonemal complex (SC),
186 respectively [64-66]. In leptonema of control spermatocytes, SYCP3 shows thin-line
187 staining structures that correspond to elongating chromosome axes (from short
188 to long lines). In zygonema, regions of two thin chromosome axes are paired
189 locally to form a thick line of SYCP3, where SYCP1 proteins are deposited for the
190 assembly of the SC central region. From early zygonema to early pachynema,
191 SC elongates along entire chromosomes, resulting in pachytene chromosome
192 configuration with 19 fully-paired thick SYCP3 lines colocalized with SYCP1 and

193 partially-paired X-Y bivalent. In *Fignl1* cKO spermatocytes, like in controls,
194 SYCP3-positive short and long lines were formed in leptonema, and short lines
195 of SYCP1 in zygonema were also observed. However, there were fewer
196 pachytene and diplotene cells in *Fignl1* cKO relative to controls (22.6±2.4% and
197 11.4±6.2% compared to 44.7±11.0% and 24.3±7.7%, respectively; Fig. 1g). We
198 also evaluated the expression of FIGNL1 protein in testicular cell squashes by
199 categorizing SYCP3-positive meiotic cells into two: cells before pachynema (i.e.
200 leptonema and zygonema) with a pan-nuclear γH2AX staining and those after
201 pachynema (i.e. pachynema and diplonema) with a dense γH2AX staining on the
202 X-Y pair (the sex body) [67] (Supplementary Fig. 1b). In controls, cells both before
203 and after pachynema were 100% positive for FIGNL1 staining. In contrast, while
204 only ~25% of cells prior to pachynema were positive for FIGNL1, cells after
205 pachynema were nearly 100% positive in *Fignl1* cKO (Fig. 1h). This indicates that
206 *Fignl1*$^{\Delta/\Delta}$ cells are fully lost before pachynema from *Fignl1* cKO testes and only
207 *Fignl1*$^{flox/\Delta}$ cells where Stra8-Cre recombinase failed excision of the *Fignl1*^{flox}
208 allele progress further to complete spermatogenesis. Further analysis of surface-
209 spread chromosomes revealed abnormal SC formation such as synapsis
210 between non-homologous chromosomes (67.7±2.0% of cells compared to
211 13.6±4.1% in controls) and multivalent synapsis (26.8±10.9 % of cells compared
212 to 3.1±2.7% in controls) in *Fignl1* cKO (Fig. 1i, j), which could be defined as
213 "pachytene-like" stage as seen in other meiotic recombination defective mutants
214 such as *Dmc1* and *Meiob* KO, etc. [68-70]. These results show that FIGNL1 is
215 necessary for full synapsis of homologous chromosomes in late zygonema and/or
216 early pachynema and that most of the FIGNL1-depleted cells seem to die at these
217 stages or do not progress further.
218
219 **Compromised meiotic recombination in *Fignl1* cKO**
220 ssDNA-binding proteins such as RPA and MEIOB-SPATA22 play a role in the
221 early/middle stage of meiotic recombination both before and after the RAD51 and
222 DMC1 assembly. To know the effect of *Fignl1* cKO on meiotic recombination, we
223 examined the localization of RPA2, a middle-subunit of RPA, on chromosome
224 spreads of spermatocytes, together with SYCP3 as a marker for the progression
225 of meiotic prophase I. In control spermatocytes, RPA2 foci appear from
226 leptonema with 200-300 foci on average in mid/late leptonema (223±73 foci; Fig.
227 2a, b). The number of RPA2 foci increased up to ~400 foci in zygonema (376±45
228 foci in mid-zygonema) and persisted throughout zygonema (332±59 foci in late

229 zygonema). The RPA2-focus number in *Fignl1* cKO mid/late leptonema was
230 increased up to 300-400 foci (368±100 foci) and a similar number persisted in the
231 early zygotene stage (409±59 foci). The number of RPA2 foci in *Fignl1* cKO
232 gradually decreased from mid-zygonema and was significantly lower than
233 controls in late zygonema (281±48 foci compared to 332±59 in controls; $p<0.0001$,
234 Mann-Whitney *U*-test; Fig. 2b), suggesting a role of FIGNL1 in the dynamic
235 behavior of an RPA-associated recombination event. We also analyzed the
236 histone γH2AX staining as a marker of DSB formation and its repair. Interestingly,
237 *Fignl1* cKO spermatocytes with increased RPA2 foci showed a similar or slightly
238 reduced intensity of γH2AX from leptonema to the late zygonema stage
239 compared to controls (Supplementary Fig. 2a, b).
240 In meiotic recombination, previous cytological analyses showed that RPA2
241 foci persist longer than DMC1/RAD51 foci from mid/late zygonema to early/mid
242 pachynema, suggesting a role of RPA in a late stage of meiotic recombination [71].
243 In zygonema (from early zygonema), foci containing the MutSγ complex with
244 MSH4 and MSH5, which regulate recombination events for CO formation, appear
245 specifically on synapsed regions and show similar behavior to RPA on meiotic
246 chromosomes [72]. We analyzed MSH4 focus formation and found that the number
247 of MSH4 foci in *Fignl1* cKO was lower than in controls in mid/late zygonema
248 (50±22 foci versus 107±47 foci in controls; Fig. 2c, d). Given the possibility that
249 the reduction in MSH4-focus number is an indirect consequence of synapsis
250 defects in *Fignl1* cKO, we also analyzed the density of MSH4 foci per unit length
251 of SC. MSH4-focus number and SC length (total SYCP1 length) showed a linear
252 relationship in control mid-zygonema ($r=0.89$; Fig. 2e). In *Fignl1* cKO, a
253 correlation between MSH4-focus number and SC length was also positive, but
254 lower than in controls ($r=0.58$). Importantly, the density of MSH4 foci per unit
255 length of SC is reduced in *Fignl1* cKO relative to controls (0.73±0.22 foci per μm
256 of SC versus 0.98±0.18 foci per μm of SC in controls; Fig. 2f). These suggest that
257 FIGNL1 is required for efficient loading of MSH4 for meiotic recombination.
258 CO formation is a key outcome of meiotic recombination. The CO sites on
259 meiotic chromosomes are marked with the foci of MutLγ complex such as MLH1
260 [73]. Control late pachytene cells show ~25 MLH1 foci per nucleus. On the other
261 hand, we could not detect any MLH1 foci on late zygotene/pachytene-like
262 chromosomes of *Fignl1* cKO spermatocytes (Supplementary Fig. 2c). This is
263 consistent with the observation that FIGNL1 is essential for the progression of
264 spermatocytes into a pachytene stage with MLH1 foci.

265
266 **FIGNL1 promotes the disassembly of DMC1 in male meiosis**
267 We next examined the localization of DMC1 on meiotic chromosomes. As shown
268 previously [74-76], in control spermatocytes, DMC1 foci appear in leptonema, peak
269 in their number at early zygonema, and gradually decrease throughout zygonema
270 (Fig. 3a, b). In *Fignl1* cKO, DMC1 foci followed similar kinetics as seen in controls.
271 However, at any stages, the number of DMC1 foci in *Fignl1* cKO was more than
272 that in controls. In early zygonema, ~500 DMC1 foci (449±89 foci) are observed
273 in *Fignl1* cKO, which is 2.3-fold more than in controls (194±32 foci). DMC1-focus
274 number in *Fignl1* cKO clearly increased through meiotic prophase I progression.
275 In late zygonema, the number of DMC1 foci in *Fignl1* cKO was reduced by half
276 of that in early zygonema (220±70 foci compared to 449±89 foci), indicating a
277 turnover of the foci. These results suggest that FIGNL1 suppresses excess
278 DMC1-focus formation and/or timely progression of DMC1-mediated
279 recombination.
280 In *Fignl1* cKO spermatocytes, we always observed two populations: cells
281 with a high number of DMC1 foci and cells with a similar number of foci to controls.
282 We assumed that the latter is *Fignl1*$^{flox/\Delta}$ cells where Cre recombinase failed
283 excision of the *Fignl1*^{flox} allele into *Fignl1*$^{\Delta}$. Note that we included these foci for
284 our quantification and that this population becomes an internal control for our
285 analysis.
286
287 **FIGNL1 promotes the disassembly of RAD51 in spermatocytes**
288 In human cultured cells, FIGNL1 regulates RAD51 assembly [51, 56]. We examined
289 the localization of RAD51 on meiotic chromosomes. As reported previously [74-76],
290 in control spermatocytes, RAD51 foci are observed from mid/late leptonema and
291 peak in early zygonema, and then decrease toward pachynema (Fig. 3c, d). The
292 average number of RAD51 foci is 107±56 and 181±27 foci per nucleus in control
293 mid/late leptotene and early zygotene stages, respectively. As seen for DMC1,
294 we detected an increased number of RAD51 foci in *Fignl1* cKO cells. The average
295 number of RAD51 foci in early zygonema is 380±98 foci, which is more than twice
296 compared to that of controls (181±27 foci). The number of RAD51 foci in
297 zygonema is similar to that of DMC1 foci, with ~600 RAD51 foci in some early
298 zygotene nuclei. When the zygotene stage progressed from early to late, the
299 RAD51-focus number in *Fignl1* cKO gradually decreased as in controls. However,
300 even at late zygonema, we detected a significant increase in RAD51-focus

301 number in *Fignl1* cKO relative to controls (182±86 foci compared to 128±32 foci
302 in controls; p=0.0163, Mann-Whitney U-test; Fig. 2d). These results show that
303 FIGNL1 promotes the timely resolution of RAD51 ensembles during the zygotene
304 stage.
305 We note that the focus intensities of RAD51 and DMC1 in *Fignl1* cKO
306 spermatocytes were slightly decreased compared to controls (Supplementary Fig.
307 3), suggesting that in *Fignl1* cKO spermatocytes, more sites for the accumulation
308 of RAD51/DMC1 molecules are present, fewer molecules of RAD51/DMC1
309 protein are on each accumulation site because of a limited number of
310 RAD51/DMC1 protein in a cell.
311
312 **Increased RAD51/DMC1 foci in early leptonema in *Fignl1* cKO**
313 In contrast to the zygotene stage where the numbers of DMC1 and RAD51 foci
314 are comparable in both controls and *Fignl1* cKO, focus numbers of DMC1 and
315 RAD51 were clearly different at early leptonema only in *Fignl1* cKO (Fig. 3a-d).
316 In mid/late leptonema when DMC1 and RAD51 foci appear on elongating SYCP3
317 stretches in controls, the number of DMC1 foci in *Fignl1* cKO is 369±156 foci per
318 cell, which is about 3-4 times more of that in controls (96±57 foci). The number
319 of RAD51 foci in mid/late leptonema in *Fignl1* cKO is 387±134 foci, 3-4 times
320 more than in controls (107±56 foci). In early leptonema, where SYCP3 short
321 stretches are yet to be elongated, DMC1 and RAD51 foci rarely appear in control
322 spermatocytes. However, *Fignl1* cKO formed a relatively larger number of RAD51
323 foci than DMC1: the number of RAD51 foci was 355±178, which exceeds the
324 number of DMC1 foci (194±148 foci) in early leptonema. These suggest that
325 FIGNL1 suppresses the formation of excess numbers of RAD51 and DMC1 foci
326 in early meiosis I, and that, in the absence of FIGNL1, RAD51 and DMC1 loading
327 is uncoupled (see below).
328
329 **Pre-meiotic S-phase in *Fignl1* cKO accumulates RAD51/DMC1 foci**
330 In wild-type meiosis, the focus formation of both RAD51 and DMC1 is mediated
331 by SPO11-induced DSBs in leptonema [77, 78]. The increased number of RAD51
332 and DMC1 foci on the early leptotene chromosome of *Fignl1* cKO spermatocytes
333 led us to analyze preleptotene (pre-meiotic S-phase) spermatocytes in order to
334 characterize the origin of excess RAD51/DMC1 foci that form in the absence of
335 FIGNL1. For *in vitro* labeling of DNA replication, we incubated testis cell
336 suspension with EdU for 1 hour in a culture medium. The preleptotene

337 spermatocytes, where a limited number of SYCP3 short stretches forms along
338 with a numerous number of “tiny” SYCP3 dots, were categorized into two classes:
339 pan dotty staining of EdU in early preleptonema and clustered dotty staining of
340 EdU in mid/late preleptonema. In controls, both early and mid/late preleptotene
341 EdU-positive spermatocytes showed very few foci of RAD51 (Fig. 4a, b). On the
342 other hand, we could detect RAD51 foci in EdU-positive spermatocytes of *Fignl1*
343 cKO, indicating RAD51-focus formation during pre-meiotic S phase. The number
344 of RAD51 foci during pre-meiotic S-phase is around 300 in focus-positive nuclei
345 (298±110 foci and 337±108 foci in early and mid/late preleptonema, respectively),
346 which is ~3/4 of the RAD51 focus number in meiotic prophase I of *Fignl1* cKO
347 mice, but ~1.5-fold more of that in early zygonema of control mice (compare Figs.
348 3d and 4b). Some RAD51 foci in pre-meiotic S-phase are colocalized with EdU
349 dots/lines (38.8±12.6% of RAD51 foci colocalized with EdU; Supplementary Fig.
350 4d), suggesting that RAD51 foci are associated with DNA replication. However,
351 when DNA replication labeling with another thymidine analog IdU was shortened
352 for 10 min, most of RAD51 foci did not colocalize with IdU foci (Supplementary
353 Fig. 4a-c), though the degree of colocalization was significantly higher than
354 random colocalization (3.7±1.9% of IdU foci colocalized with RAD51 compared
355 to 2.5±1.3%, p=0.0261, Mann-Whitney U-test; 9.1±4.5% of RAD51 foci
356 colocalized with IdU compared to 6.2±3.3%, p=0.0439, Mann-Whitney U-test;
357 Supplementary Fig. 4c). It is unlikely that RAD51 is associated with ongoing DNA
358 replication forks in *Fignl1* cKO spermatocytes.
359 Further evaluation of DMC1 localization in *Fignl1* cKO revealed the
360 presence of preleptotene spermatocytes containing DMC1 foci (Fig. 4c, d). The
361 number of DMC1 foci in focus-positive nuclei is around 150 (136±71 foci and
362 164±70 foci in early and mid/late preleptonema, respectively), about half of
363 RAD51 foci in *Fignl1* cKO. As seen for RAD51, most of DMC1 foci did not
364 colocalize with ongoing DNA replication forks when DNA replication was labeled
365 with EdU for 10 min (23.0±7.9% of DMC1 foci colocalized with EdU;
366 Supplementary Fig. 5a-c). Of note is that very few DMC1 foci were detected in
367 control preleptotene spermatocytes. This suggests that FIGNL1 limits the
368 assembly of mitotic recombination machinery with RAD51 on chromatin during
369 pre-meiotic S-phase as well as meiotic recombination machinery containing
370 DMC1.
371 In contrast to compromised meiotic recombination and homolog synapsis
372 as described above, pre-meiotic DNA replication in *Fignl1 c*KO seemed largely

373 normal, as the number of RPA2 foci, which are expected to correspond to
374 replication fork-associated ssDNAs, and IdU foci with 10 min labeling, which
375 indicates ongoing DNA replication forks, in early preleptotene spermatocytes
376 were comparable between *Fignl1* cKO and controls (624±241 RPA2 foci in *Fignl1*
377 cKO compared to 607±217 foci in controls; p=0.9414, Mann-Whitney U-test;
378 500±131 IdU foci in *Fignl1* cKO compared to 476±140 foci in controls; p=0.4652,
379 Mann-Whitney U-test; Supplementary Fig, 6a-c). However, we cannot exclude
380 the possibility that FIGNL1 plays a role in pre-meiotic DNA replication as recently
381 shown in *FIGNL1* KO human cell lines [79].
382
383 **Uncoupled loading of RAD51 and DMC1 in *Fignl1* cKO spermatocytes**
384 Despite the overall increase in RAD51 and DMC1 focus numbers at each
385 analyzed stage of *Fignl1* cKO spermatocytes, we observed ~2-fold more RAD51
386 foci compared to DMC1 foci in preleptotene and early leptotene stages,
387 suggesting uncoupling of RAD51 and DMC1 loading onto chromosomes in the
388 absence of FIGNL1. Co-staining of RAD51 and DMC1 confirmed different
389 kinetics of RAD51 and DMC1 in *Fignl1* cKO (Fig. 3e, f, Supplementary Fig. 7);
390 DMC1 focus numbers gradually increase from preleptonema to late
391 leptonema/early zygonema (177±74, 325±136, and 407±69 foci in preleptonema,
392 early leptonema, and late leptonema/early zygonema, respectively; Fig. 3f),
393 whereas RAD51-focus numbers are nearly constant in those stages (399±120,
394 476±109, and 480±95 foci in preleptonema, early leptonema, and late
395 leptonema/early zygonema, respectively). Colocalization analysis revealed a
396 gradual increase in the number of RAD51-DMC1 co-foci as DMC1 foci increased.
397 In preleptotene and early leptotene spermatocytes, 50-60% of DMC1 foci
398 colocalized with RAD51 foci (57.0±10.6% and 53.1±11.0% in preleptonema and
399 early leptonema, respectively; Fig, 3f) and less than 40% of RAD51 foci
400 colocalized with DMC1 foci (25.7±9.9% and 35.3±12.0% in preleptonema and
401 early leptonema, respectively). The degree of colocalization at these stages is
402 significantly lower than that in the late leptotene/early zygotene stage where
403 comparable levels of colocalization with controls were observed (65.8±10.1% and
404 67.2±7.6% of DMC1 foci colocalized with RAD51 in *Fignl1* cKO and controls,
405 respectively; 56.2±9.6% and 59.3±8.9% of RAD51 foci colocalized with DMC1
406 foci in *Fignl1* cKO and controls, respectively; Fig. 3f). These suggest that coupled
407 loading of RAD51 and DMC1 in pre-meiotic S-phase and early meiotic prophase
408 I is compromised in *Fignl1* cKO spermatocytes. On the other hand, the fact that

409 more than half of DMC1 foci are colocalized with RAD51 in preleptonema
410 suggests that DMC1 preferentially binds to meiotic chromatin where RAD51 is
411 already bound.
412
413 **RAD51/DMC1-focus formation in *Spo11* KO *Fignl1* cKO spermatocytes**
414 Both RAD51 and DMC1 foci appear in pre-meiotic S-phase in *Fignl1* cKO
415 spermatocytes, which is much earlier than meiotic prophase I with programmed
416 DSB formation by SPO11. To examine whether RAD51/DMC1-focus formation in
417 *Fignl1* cKO mice is independent of meiotic DSB formation or not, we constructed
418 *Spo11* KO *Fignl1* cKO mice (*Spo11*$^{-/-}$ *Fignl1*$^{flox/\Delta}$ *Stra8-Cre*$^{+}$), which are expected
419 to be defective in SPO11-mediated DSB formation [77, 78]. As shown previously,
420 spermatocytes from control *Spo11* KO mice (*Spo11*$^{-/-}$ *Fignl1*$^{flox/\Delta}$) did not show
421 any RAD51 foci on meiotic chromosomes (Fig. 5a, b, Supplementary Fig. 8a). On
422 the other hand, spermatocytes from *Spo11* KO *Fignl1* cKO show on average 300-
423 400 RAD51 foci from leptotene to zygotene(-like) stages (407±77, 390±64, and
424 292±34 foci for focus-positive nuclei in leptonema, early zygonema, and late
425 zygonema, respectively; Fig. 5b). Moreover, *Spo11* KO *Fignl1* cKO also
426 accumulates DMC1 foci with similar numbers to RAD51 foci (374±108, 391±57,
427 and 342±54 foci for focus-positive nuclei in leptonema, early zygonema, and mid-
428 zygonema, respectively; Fig. 5c, d, Supplementary Fig. 8b). Comparable
429 numbers of RAD51 and DMC1 foci between *Fignl1* cKO and *Spo11* KO *Fignl1*
430 cKO indicate that a large fraction of RAD51 and DMC1 foci on meiotic chromatin
431 in the absence of FIGNL1 is independent of SPO11, thus meiotic DSBs. Like
432 *Spo11* KO, *Spo11* KO *Fignl1* cKO spermatocytes lack pan-nuclear γH2AX
433 staining and form few RPA2 foci (Supplementary Fig. 8c-f), supporting the
434 assembly of RAD51/DMC1 complexes in the absence of endogenous DSBs and
435 ssDNAs. *Spo11* KO *Fignl1* cKO spermatocytes died in the pachytene-like stage
436 with the formation of the pseudo-sex body (Supplementary Fig. 8c) as seen in
437 *Spo11* KO spermatocytes [77, 78]. We also detected RAD51/DMC1 foci in
438 preleptotene spermatocytes of *Spo11* KO *Fignl1* cKO mice (Fig. 5f). This confirms
439 that the formation of RAD51 and DMC1 foci during pre-meiotic S-phase is
440 independent of the SPO11 function. Importantly, the degree of RAD51-DMC1
441 colocalization from preleptonema to early zygonema in *Spo11* KO *Fignl1* cKO is
442 comparable to that in *Fignl1* cKO and more than half of DMC1 foci are colocalized
443 with RAD51 at those stages in *Spo11* KO *Fignl1* cKO (Fig. 5e-g). This supports
444 the idea that DMC1 preferentially binds to RAD51-bound meiotic chromatin,

445 which is most likely dsDNA in the absence of meiotic DSB formation.
446
447 **RAD51 binds to and persists on meiotic recombination sites in *Fignl1* cKO**
448 **spermatocytes**
449 As described above, the absence of FIGNL1 increases the SPO11-independent
450 formation of RAD51 and DMC1 foci in meiotic prophase I, some of which would
451 come from pre-meiotic S-phase. Comparable numbers of RAD51 and DMC1 foci
452 in the presence and absence of SPO11 (i.e., meiotic DSBs) prompted us to check
453 whether RAD51/DMC1 can bind to meiotic recombination hotspots, especially
454 ssDNA. Chromatin immunoprecipitation followed by single-stranded DNA
455 sequencing (ChIP-SSDS) for RAD51 [80-82] revealed that in *Fignl1* cKO testes, like
456 in controls, RAD51 binds to recombination hotspots where DMC1 strongly binds
457 in wild-type testes (Fig. 6a, Supplementary Fig. 9a). Importantly, when RAD51
458 binding around hotspots is ranked based on the number of SPO11-oligos in wild-
459 type, a similar binding profile of RAD51 is seen between *Fignl1* cKO and controls,
460 with a small increase in RAD51 ChIP-SSDS signals in two out of three *Fignl1*
461 cKO mice (Fig. 6b, Supplementary Fig. 9b-d). We also ran RAD51 ChIP-SSDS
462 in *Spo11* KO and *Spo11* KO *Fignl1* cKO testes, confirming no RAD51 enrichment
463 at recombination hotspots and lower RAD51 enrichment in the entire genome
464 (Supplementary Fig. 10a-c). Most of non-overlapping 2-kb bins with high RAD51
465 enrichment in *Spo11* KO *Fignl1* cKO testes were common to *Spo11* KO testes
466 (94.1%; 241/256; Supplementary Fig. 10d), indicating a similar binding profile of
467 RAD51 on ssDNAs between *Spo11* KO and *Spo11* KO *Fignl1* cKO mice. These
468 suggest that, in the absence of FIGNL1, RAD51 does not bind to any specific
469 regions with ssDNAs in *Spo11* KO spermatocytes.
470 To address whether RAD51 persists on meiotic recombination sites in the
471 absence of FIGNL1, we also measured the colocalization frequency of RAD51
472 and RPA2 in mid/late zygonema, given that RPA2 localizes to recombination sites
473 even after RAD51/DMC1 disassembly in wild-type meiosis and can be a marker
474 of recombination sites on mid/late zygotene chromosomes. In control mid/late
475 zygotene spermatocytes, out of 234±44 RPA2 foci, 41±15 foci were colocalized
476 with RAD51 foci, which corresponds to 17.2±4.3% of RPA2 foci (Fig. 6c-e). *Fignl1*
477 cKO exhibited two classes of populations; one is similar to controls (~30%) and
478 the other shows 40-80% of colocalization, with 45.4±21.9% of RPA2 foci
479 colocalized with RAD51 for all populations. This is consistent with the idea that
480 RAD51 binds to ssDNA on meiotic recombination sites in the absence of FIGNL1,

481 suggesting that RAD51 persists on RPA2-associated recombination sites.
482
483 ***Fignl1* deficiency rescues RAD51/DMC1 assembly defects in *Swsap1***
484 Our previous study in human cells showed that FIGNL1 antagonizes the function
485 of the RAD51 mediator, SWSAP1 [51]. In mouse male meiosis, SWSAP1 is
486 necessary for efficient RAD51/DMC1 focus formation [17, 51]. We tested the effect
487 of *Fignl1* cKO on RAD51/DMC1 assembly in *Swsap1* KO cells by generating
488 *Swsap1* KO *Fignl1* cKO male mice (*Swasp1*$^{-/-}$ *Fignl1*$^{flox/\Delta}$ *Stra8-Cre*$^{+}$). As reported
489 [17, 51], surface-spread chromosomes from *Swasp1* KO spermatocytes (*Swsap1*$^{-/-}$
490 *Fignl1*$^{flox/\Delta}$) showed a large reduction of RAD51 foci with 10-30 foci (~1/10 of
491 control *Fignl1*$^{flox/\Delta}$) in leptonema and zygonema (29±26, 22±15, and 20±14 foci in
492 leptonema, early zygonema, and mid zygonema, respectively; Fig. 7a, b). Like
493 *Fignl1* cKO, *Swsap1* KO *Fignl1* cKO spermatocytes showed an accumulation of
494 RAD51 foci on meiotic chromosomes. The number of RAD51 foci from leptonema
495 to mid-zygonema in *Swsap1* KO *Fignl1* cKO is very similar to that in *Fignl1* cKO
496 (320±217, 308±221, and 194±179 foci in *Swsap1* KO *Fignl1* cKO and 399±145,
497 377±98, and 282±91 foci in *Fignl1* cKO in leptonema, early zygonema, and mid
498 zygonema, respectively). This indicates that in mouse spermatogenesis without
499 FIGNL1, RAD51 assembly does not depend on SWSAP1. This is consistent with
500 the results in human cultured cells. On the other hand, in late zygonema, the
501 number of RAD51 foci in *Swsap1* KO *Fignl1* cKO was comparable to *Swsap1* KO
502 and much lower than that in *Fignl1* cKO (10±12, 7±8, and 189±79 foci in *Swsap1*
503 KO *Fignl1* cKO, *Swsap1* KO, and *Fignl1* cKO, respectively; Fig. 7b). This
504 suggests that only *Swsap1*$^{-/-}$ *Fignl1*$^{flox/\Delta}$ cells where Cre recombinase failed
505 excision of *Fignl1*^{flox} allele can progress into late zygotene stage in *Swsap1* KO
506 *Fignl1* cKO testes. Moreover, similar results were observed for DMC1; the
507 number of DMC1 foci in *Swsap1* KO *Fignl1* cKO was comparable to *Fignl1* cKO
508 (Fig. 7c, d). Thus, reduced DMC1-focus formation in *Swsap1* KO is also
509 suppressed by *Fignl1* cKO. It is likely that the activity of FIGNL1 to suppress
510 RAD51/DMC1 assembly on intact dsDNAs is independent of SWSAP1-mediated
511 stable assembly of RAD51/DMC1 on DSB-induced ssDNAs.
512
513 **FIGNL1 disrupts RAD51-dsDNA complex *in vitro***
514 We previously showed that FIGNL1 promotes the dissociation of RAD51 from
515 ssDNAs *in vitro* [51]. The above results in mouse spermatocytes suggest that
516 FIGNL1 can disrupt RAD51 filaments on chromosomal DNAs, both ssDNAs and

517 dsDNAs. To address whether FIGNL1 promotes the dissociation of RAD51
518 filaments on dsDNAs *in vitro*, we purified human FIGNL1ΔN, which lacks N-
519 terminal 284 amino acids [51], since a full-length human FIGNL1 protein was
520 insoluble when expressed in *E. coli*, and performed the electrophoretic mobility
521 shift assay (EMSA). First, we confirmed that a purified human FIGNL1ΔN
522 disrupted the pre-formed RAD51-ssDNA complexes in the presence of ATP (Fig.
523 8a, b). Under this condition, FIGNL1ΔN could disrupt ~30% of RAD51-ssDNA
524 complex (24.6±6.9% of unbound DNAs were increased to 42.9±2.1% by the
525 addition of 1.2 μM of FIGNL1ΔN). When FIGNL1ΔN was incubated with a pre-
526 formed RAD51-dsDNA complex, the most of dsDNA was recovered as an
527 unbound form (25.8±11.1% of unbound DNAs were increased to 80.0±11.6%).
528 This suggests that FIGNL1ΔN could disrupt the RAD51-dsDNA complex more
529 efficiently than the RAD51-ssDNA complex *in vitro*, supporting the *in vivo* results.
530 Alternatively, RAD51-ssDNA *in vitro* might form an aggregate more than RAD51-
531 dsDNA, which may affect the accessibility by FIGNL1 protein to disrupt the
532 complexes.
533
534 **Discussion**
535 In this study, we analyzed the role of FIGNL1 AAA+ ATPase, which plays a critical
536 role in homologous recombination in somatic cells, in mouse male meiosis. *Fignl1*
537 cKO mice displayed higher levels of RAD51 and DMC1 foci than controls, as well
538 as defective chromosome synapsis. Our analysis revealed the dual function of
539 FIGNL1 during spermatogenesis (Fig. 8c). One is to promote meiotic
540 recombination by regulating the dissociation of RAD51/DMC1 ensembles on the
541 ssDNA. The other is to protect the genome by disrupting the non-functional form
542 of RAD51/DMC1 ensembles on the dsDNA. Consistent with the idea, purified
543 FIGNL1 can disrupt the RAD51-dsDNA complex as well as the RAD51-ssDNA
544 complex *in vitro*. The same conclusion was obtained by Baudat's group by
545 characterizing the *Fignl1* cKO as well as *Firrm* cKO (accompanying paper).
546
547 **FIGNL1 promotes the post-assembly step of RAD51/DMC1 in meiotic**
548 **recombination**
549 In meiotic recombination, RAD51/DMC1 filaments on ssDNAs play a critical role
550 in homology search and strand exchange with homologous dsDNA, leading to
551 the formation of the D-loop, in which the 3'-OH end of the invading strand
552 becomes a substrate for recombination-associated DNA synthesis. Biochemical

553 analyses showed that RAD51/DMC1-mediated D-loop is a poor substrate for *in*
554 *vitro* DNA synthesis by DNA polymerase δ and its accessory factors [83-85]. To
555 promote efficient DNA synthesis on the recombination intermediate,
556 RAD51/DMC1 bound to the intermediate should be removed by factors such as
557 RAD54, a RAD51 remodeler [83-85]. Although the male KO mice for *Rad54* and
558 *Rad54b*, a *Rad54* paralog, and the double KO mice for *Rad54* and *Rad54b* are
559 fertile, the *Rad54 Rad54b* double KO spermatocytes show abnormal loading of
560 RAD51 on chromosomes in pachynema and diplonema [54]. This is consistent with
561 the role of RAD54 in the post-assembly step of RAD51 (DMC1 had not been
562 analyzed in detail). Our *in vivo* and *in vitro* studies suggest the role of FIGNL1 in
563 the post-assembly step of the RAD51/DMC1 filaments. It is likely that FIGNL1
564 disrupts not only RAD51 but also DMC1 filaments on recombination
565 intermediates for subsequent DNA synthesis [84, 86] (Fig. 8c), though other
566 possibilities including that proper disassembly of RAD51 and DMC1 filaments
567 promotes strand invasion won't be excluded. Post-assembly role of FIGNL1 in
568 RAD51-mediated homologous recombination was reported previously in human
569 cells with DNA damage [56]. Consistent with the post-assembly role of FINGL1,
570 *Fignl1* cKO spermatocytes reduce the formation of MSH4 foci, which appears
571 after the loading and dissociation of RAD51/DMC1 [72]. *Fignl1* cKO spermatocytes
572 seem not to enter the pachytene stage for the loading of the MutLγ complex such
573 as MLH1 and most *Fignl1* KO cells die around late zygonema. The meiotic
574 defects seen in *Fignl1* cKO are similar to those in the mutants where
575 RAD51/DMC1 foci accumulate in a higher number than normal such as *Msh4*,
576 *Msh5*, *Mcm8*, *Trip13,* and *Mcmdc2* mutant spermatocytes [87-93]. In mouse
577 spermatocytes, FIGNL1 seems to promote ZMM-dependent CO formation. This
578 is different from the role of FIGNL1 ortholog, FIGL1, in *A. thaliana*. *Arabidopsis*
579 *FIGL1* mutant meiocytes showed normal or slightly elevated CO formation [57, 58].
580 Indeed, the depletion of FIGL1 or its partner FLIP suppresses reduced CO
581 formation in the absence of pro-CO proteins, ZMM [57, 58]. This suggests the role
582 of plant FIGL1-FLIP as an anti-CO factor, which disrupts early recombination
583 intermediates such as RAD51/DMC1 filaments on the ssDNA prior to or during
584 the strand invasion. Although our attempt to analyze the role of FIGNL1 in mouse
585 oocytes failed due to insufficient excision of the *Fignl1*^{flox} allele in oocytes by the
586 *Stra8-Cre* transgene used in this study, a recent study by Yu and colleagues
587 demonstrated the accumulation of RAD51 in not only *Firrm/Flip* cKO
588 spermatocytes but also in oocytes with infertility in both male and female mice [79],

589 suggesting that the essential role of the FIGNL1-FIRRM complex in meiotic
590 recombination is shared between males and females.
591
592 **FIGNL1 disrupts non-productive RAD51 and DMC1 ensembles on duplex**
593 **DNAs**
594 RAD51/DMC1 focus formation normally occurs at sites of ssDNA tracks that are
595 associated with mitotic or meiotic DSBs. The most striking phenotypes seen in
596 *Fignl1* cKO spermatocytes are the accumulation of RAD51 and DMC1 foci in
597 unchallenged pre-meiotic S-phase cells and spermatocytes in the absence of
598 SPO11-dependent meiotic DSBs. This accumulation of RAD51/DMC1 foci in the
599 absence of DSBs, therefore the ssDNAs, could be simply explained by the non-
600 specific assembly of RAD51/DMC1 filaments on chromatin DNAs, thus the
601 binding to dsDNA (Fig. 8c). Interestingly, human RAD51 and DMC1 bind to both
602 ssDNAs and dsDNA with similar affinity *in vitro* [16, 94] and RAD51 bears an activity
603 to remodel the nucleosome upon the dsDNA binding [95-97]. On the other hand,
604 detection of RAD51/DMC1 foci *in vivo* normally requires the presence of tracts of
605 ssDNAs. How cells discriminate ssDNAs among lots of competitors, dsDNAs, in
606 the RAD51/DMC1 binding remains unsolved. Based on the results described
607 here, we propose that FIGNL1 actively dismantles RAD51 and DMC1 filaments
608 on dsDNAs, which is otherwise non-productive for the recombination and/or
609 might become obstacles to chromosomal events on duplex DNAs such as DNA
610 replication, transcription, and others. Indeed, Bishop, Heyer and their colleagues
611 reported activities of the RAD54 translocase family to remove RAD51 and DMC1
612 from dsDNAs. In yeast meiosis, Spo11-independent focus formation of Dmc1, but
613 not of Rad51, depends on Tid1/Rdh54, a Rad54 homolog [98]. And mitotic
614 spontaneous Rad51-focus formation on yeast chromosomes is increased in the
615 absence of three translocases, Rad54, Tid1/Rdh54, and Uls1 [99]. Moreover, in
616 unchallenged human cells, the absence of two RAD54 family proteins RAD54 (or
617 RAD54L) and RAD54B leads to the accumulation of spontaneous RAD51 foci
618 particularly when RAD51 is over-expressed [100]. These *in vivo* studies were further
619 supported by biochemical analysis showing that Rad54 dissociates RAD51 from
620 dsDNAs [101-103]. Further studies are necessary to reveal the relationship between
621 FIGNL1 and RAD54 translocases in the disassembling of RAD51/DMC1 on
622 duplex DNAs. We stress that, distinct from RAD54, which dismantles RAD51
623 filaments only on dsDNAs (not on ssDNAs), FIGNL1 can disrupt RAD51
624 ensembles on both ss- and dsDNAs.

One of the striking features of RAD51/DMC1 assembles on duplex DNAs is that these ensembles are quite stable. The number of RAD51 in both pre-meiotic S-phase and early meiotic prophase I from early leptonema to early zygonema is constant. Little increase in RAD51-focus number during early meiotic prophase I suggest that spermatocytes show very limited additional assembly of RAD51 foci during this stage. On the other hand, DMC1 shows a 2-fold increase in focus number from early leptonema (and pre-meiotic S-phase) to early zygonema. This increase could be induced by SPO11-mediated DSBs. Interestingly, the colocalization frequency of RAD51 with DMC1 in *Fignl1* cKO increased from ~30% to ~60%, which is similar to the colocalization frequency seen in control early zygonema, while the colocalization frequency of DMC1 with RAD51 is nearly constant (with 60-70% frequency). This suggests that RAD51 ensembles even on the dsDNA tend to recruit DMC1 to form co-ensembles.

FIGNL1 antagonizes SWSAP1 for RAD51/DMC1 assembly on meiotic chromosomes

FIGNL1 shows antagonism to the RAD51 mediator. In human cells, *FIGNL1* depletion suppresses RAD51-assembly defect induced by the *SWSAP1* depletion [51]. In meiosis of the *A. thaliana*, *FIGL1* (*A. thaliana FIGNL1*) and/or *FLIP* deletion restores reduced RAD51/DMC1-focus formation in the mutants of the *BRCA2* [61] as well as defective DMC1-focus formation in the mutant of the *SDS1*, which promotes DMC1 assembly [57]. Since *Swsap1* KO spermatocytes reduced the RAD51 and DMC1 foci [17, 51], we asked whether *Fignl1* cKO could also suppress these meiotic defects in *Swsap1* KO spermatocytes and found that the number of both RAD51/DMC1 foci in *Swsap1* KO *Fignl1* cKO is similar to those in *Fignl1* cKO. This is simply interpreted as, like in human cells, *Fignl1* cKO suppresses RAD51/DMC1-assembly defect in *Swsap1* KO. However, at this point, we do not know whether RAD51/DMC1 foci are associated with ssDNAs in meiotic prophase I cells of *Swsap1* KO *Fignl1* cKO as shown in *Fignl1* cKO, although it is likely. In addition, different from RAD51/DMC1 assembly on ssDNAs, these suggest that RAD51/DMC1 assembly on the dsDNA in the absence of FIGNL1 does not require the RAD51/DMC1 mediator, SWSAP1.

658 **Methods**

659

660 **Mice**

661 The care and use of mice in this study were performed under the guideline for
662 the proper conduct of animal experiments (Society Council of Japan). These
663 procedures were approved by the Institutional Animal Care Committee at Institute
664 for Protein Research, Osaka University (approval ID; 25-03-0).

665 All mice used in this study were congenic to the C57BL/6 background.
666 Genotyping of mice was performed by PCR on genomic DNA isolated from mice.
667 Primers used for genotyping are listed in Supplementary table 1. Mature adult
668 mice (8-20 weeks old) were used for experiments otherwise mentioned.

669 *Fignl1*^{flox} allele was constructed by Cyagen Bioscience Co. Ltd. ES cells with
670 the *Fignl1*^{flox} allele were injected into C57BL/6 albino blastocytes, which were
671 transplanted into CD-1 pseudo-pregnant female mice. The founder mice with the
672 correct *Fignl1*^{flox} allele were backcrossed to C57BL/6 mice. *Fignl1*$^{+/\Delta}$ allele was
673 constructed by breeding *Fignl1*$^{flox/+}$ with *CAG-Cre* mice. *Stra8-Cre* transgenic
674 mice were previously described [104] and provided *by* the RIKEN Animal Resource
675 Center. *Spo11*$^{-/-}$ mouse was previously described [77] and *Spo11*$^{+/-}$ mice with a
676 mixed background of C57BL/6 and 129/SvJ were backcrossed to C57BL/6 mice
677 prior to experiments. *Swsap1*$^{-/-}$ mice were described in our previous study [51].

678

679 **Histology**

680 Testes from adult mice were fixed in 10% buffered formalin overnight at room
681 temperature, washed twice with PBS, and stored in 70% EtOH at 4ºC prior to
682 embedding in paraffin and sectioning. The sections of 5 μm thickness were
683 deparaffinized and stained with periodic acid-Schiff (PAS).

684

685 **Spermatocyte-chromosome spreads**

686 Surface-spread chromosomes of spermatocytes were prepared as described
687 previously [105, 106] with slight modification. Testes were dissected, the tunica
688 albuginea was removed, and adherent extra-tubular tissues were removed by
689 rinsing and dissociating seminiferous tubules in PBS using a pair of 25-gauge
690 needles in a 35 mm petri dish (Corning, 430165). Dissociated seminiferous
691 tubules were incubated in hypotonic extraction buffer (30 mM Tris-HCl pH 8.0, 50
692 mM sucrose, 17 mM trisodium citrate dihydrate, 5 mM EDTA, 0.5 mM
693 Dithiothreitol (DTT) and 0.5 mM phenylmethylsulphonyl fluoride (PMSF), pH 8.2-

694 8.3; HEB) for 15-45 min at room temperature. After quickly rinsing seminiferous
695 tubules in 100 mM sucrose, some tubules were placed in 40 μl of 100 mM sucrose
696 on a glass depression slide. Tubules were torn to pieces using two fine forceps,
697 and pieces of tubular remnants were removed. The cell suspension was made by
698 pipetting, and 20 μl of cell suspension was placed on a clean glass slide
699 (Matsunami, MAS-01) coated with freshly made 1% paraformaldehyde (PFA)
700 solution pH 9.2 (pH set by 1.25 M sodium borate) containing 0.15% Triton X-100.
701 Slides were placed and dried in a closed humid chamber with hot tap water
702 overnight at room temperature, followed by drying with lids ajar for 3 h and then
703 with lids removed for 1-2 hr. Slides were washed once for 5 min in deionized
704 water and twice for 5 min in 0.4% DryWell (Fujifilm) in a coplin jar and air-dried at
705 room temperature. Slides were either directly processed for immunostaining as
706 below or stored in aluminum foil at -80°C prior to immunostaining.
707 For the preparation of testicular cell suspension, testes were dissected, the
708 tunica albuginea was removed, and seminiferous tubules were transferred into 1
709 ml of testis cell isolation medium (104 mM NaCl, 45 mM KCl, 1.2 mM $MgSO_4$, 0.6
710 mM $NaHPO_4$, 0.15 (w/v) glucose; TIM) containing 2 mg of collagenase
711 (Worthington, LS004186) for incubation at 32°C for 55 min with shaking at 53 rpm.
712 Tubules were washed three times with 3 ml of TIM, and suspended in 1 ml of TIM
713 containing 0.7 mg of Trypsin (Worthington, LS003740) and 4 μg of DNase I
714 (Roche, 104159) for incubation at 32°C for 15 min with shaking at 53 rpm.
715 Trypsinization was stopped by adding 5 mg of Trypsin inhibitor (Sigma, T9003)
716 and 10 μg of DNase I, and cells were separated by pipetting and filtered through
717 a 70 μm cell strainer (Corning, 431751). Cells were washed once with 0.75 μg of
718 DNase I and 7.5 ml of TIM, and suspended in 0.75 μg of DNase I and PBS
719 (Nakarai, 14249-24) to 1 x10^6 cell/ml. 1 ml of cell suspension was centrifuged at
720 200 x *g* for 5 min at room temperature. After carefully removing the supernatant,
721 cells were suspended in 30 μl of HEB and incubated for 15-45 min at room
722 temperature. 30 μl of 100 mM sucrose was added, and 20 μl of cell suspension
723 was placed on a clean glass slide (Matsunami, MAS-01) coated with 100 μl of
724 freshly made 1% paraformaldehyde (PFA) solution pH 9.2 containing 0.15%
725 Triton X-100. Slides were placed and dried in a closed humid chamber, washed,
726 and stored as described above.
727
728 **Immunofluorescence staining**
729 Slides were rehydrated with Tris-buffered saline (TBS) pH 8.0 containing 0.05%

730 of Triton X-100 (TBST) for 3 min, blocked twice with blocking buffer (1% normal
731 goat or donkey serum, 3% bovine serum albumin (BSA), 1x TBS pH 8.0, 0.05%
732 of Triton X-100, 0.05% sodium azide) for 15 min at room temperature and
733 incubated with primary antibodies in antibody dilution buffer (10% normal goat or
734 donkey serum, 3% BSA, 1x TBS pH 8.0, 0.05% of Triton X-100, 0.05% sodium
735 azide) in a humid chamber overnight at room temperature. Slides were quickly
736 rinsed with TBST, washed twice with TBST for 5 min, blocked twice with blocking
737 buffer for 15 min at room temperature, and incubated with secondary antibodies
738 in antibody dilution buffer in a humid chamber for 1 h at 37°C. Slides were quickly
739 rinsed with TBST, washed three times with TBST for 5 min, washed once with
740 Milli-Q water for 2 min, and air-dried before mounting with ProLong Diamond
741 Antifade Mountant (Thermo Fisher Scientific, P36970). For detection of IdU,
742 rehydrated slides were denatured with 4N HCl for 10 min at room temperature
743 before blocking. EdU was detected using Click-iT EdU Imaging Kit with Alexa
744 Fluor 647 azides according to the manufacturer's instruction (Invitrogen). All
745 primary and secondary antibodies used are listed in Supplementary table 2.
746
747 **Testicular cell squashes**
748 Testes were dissected, the tunica albuginea was removed, and adherent extra-
749 tubular tissues were removed by rinsing and dissociating seminiferous tubules in
750 PBS using a pair of 25-gauge needles in a 35 mm petri dish (Corning, 430165).
751 Dissociated seminiferous tubules were fixed in freshly prepared 2%
752 formaldehyde containing 0.1% Triton X-100 for 10 min at room temperature.
753 Small pieces of tubules were placed on a clean glass slide (Matsunami, MAS-01),
754 torn using two fine forceps, and squashed under a coverslip with pressure from
755 the blunt end of pencil followed by a thumb. Slides were frozen briefly in liquid
756 nitrogen and either directly processed for immunostaining or stored at -80°C prior
757 to immunostaining. After the removal of coverslips, slides were washed three
758 times with PBS for 5 min and immunostaining was performed as described above.
759
760 **Image acquisition**
761 Images of mouse spermatocyte spreads testicular cell squashes were acquired
762 using a computer-assisted fluorescence microscope system (DeltaVision;
763 Applied Precision) with a 60× NA 1.4 oil immersion objective. Image
764 deconvolution was performed using an image workstation (SoftWorks; Applied
765 Precision) and afterward processed using Imaris (Oxford Instruments, UK) and

766 Photoshop (Adobe, USA) software tools. Images in each figure are matched
767 exposure.
768
769 **Image analysis**
770 Comparisons were made between animals that were either littermate or matched
771 by age. Single cells were manually cropped, and numbers of foci were counted
772 by the auto-thresholding signal intensity in Imaris software (Oxford Instrument)
773 and clear foci that were missed by auto-thresholding, especially adjacent foci,
774 were manually counted. Signal intensities were measured using Image J software
775 by subtracting signal intensities of single cells from those of regions of interest
776 (ROIs) manually drawn next to cells as backgrounds.
777 Meiotic prophase I stages on spermatocyte spreads were defined by
778 SYCP3 and SYCP1 staining using standard criteria. Leptonema was defined by
779 short SYCP3 stretches without evidence of synapsis determined by SYCP1
780 staining. Zygonema was defined by longer stretches of SYCP3 with various
781 degrees of synapsis: early, mid- and late zygonema was defined by having <25%,
782 25-75%, and >75% of synapsis, respectively. Pachynema was defined by the full
783 synapsis of all autosomes. Diplonema was defined by de-synapsis beginning
784 from mostly the middle of chromosomes with various degrees of residual
785 synapsis. Preleptonema was defined by very short SYCP3 stretches with EdU or
786 IdU-positive staining.
787
788 **EdU incorporation**
789 1 ml of 1 x10^6 cell/ml testicular cell suspension in PBS was centrifuged at 200 x
790 *g* for 5 min at room temperature, and after removal of the supernatant, cells were
791 suspended in 500 μl of D-MEM (Wako, 044-29765) / 10% FBS containing 10 μM
792 EdU. After incubation at 37°C for 10 min or 1 h in a well of a 12-well dish (Violamo),
793 cells were pelleted by centrifugation at 200 x *g* for 5 min at room temperature,
794 washed in 1 ml of PBS once, and suspended in 30 μl HEB for incubation for 15-
795 30 min at room temperature. After adding 30 μl of 100 mM sucrose, cells were
796 fixed, and the slides were dried, washed, and stored as described above.
797
798 **IdU pulse incorporation**
799 1 ml of 1 x10^6 cell/ml testicular cell suspension in PBS was centrifuged at 200 x
800 *g* for 5 min at room temperature, and after removal of the supernatant, cells were
801 suspended in 500 μl of D-MEM (Wako, 044-29765) / 10% FBS containing 20 μM

802 IdU (Sigma, I7125). After incubation at 37°C for 10 min in a well of a 12-well dish
803 (Violamo), cells were subjected to chromosome spreads as described above.
804
805 **Rad51 Chromatin immuno-precipitation – single-stranded DNA sequencing**
806 **(ChIP-SSDS)**
807 ChIP was performed as described previously [80]. One testis from the control and
808 a pair of testes from *Fignl1* cKO, *Spo11* KO, and *Spo11* KO *Fignl1* cKO mice (9-
809 20 weeks, except a *Spo11* KO mouse at 31 weeks) were dissected, the tunica
810 albuginea was removed, and seminiferous tubules were crosslinked in 10 ml of
811 1% formaldehyde (Pierce, 28908) in PBS (Nakarai, 14249-24) for 10 min at room
812 temperature. Crosslinking was quenched by adding 2.5 M glycine to a final
813 concentration of 125 mM. After 5 min of incubation at room temperature, cells
814 were washed once with 10 ml of cold PBS, and the cell pellet was snap-frozen
815 on liquid nitrogen and stored at -80°C. The frozen cell pellet was suspended in
816 500 µl of cell lysis buffer (0.25% Triton X-100, 10 mM EDTA, 0.5 mM EGTA, 10
817 mM Tris-HCl pH 8.0) supplemented with protease inhibitor (Roche,
818 04693159001), incubated for 10 min on ice, and centrifuged at 300 x *g* for 3 min
819 at 4°C. The nuclei pellet was washed in 500 µl of lysis wash buffer (200 mM NaCl,
820 1 mM EDTA, 0.5 mM EGTA, 10 mM Tris-HCl pH 8.0) supplemented with protease
821 inhibitor, resuspended in 200 µl of RIPA buffer (10 mM Tris-HCl pH 8.0, 1 mM
822 EDTA, 0.5 mM EGTA, 1% Triton X-100, 0.1% sodium deoxycholate, 0.1% SDS,
823 140 mM NaCl) supplemented with protease inhibitor, split into two ~130 µl
824 aliquots and sonicated on the Covaris M220 for 5 min 30 sec at 5-9°C with a
825 setting of Peak Power 50.0, Duty Factor 20.0, and Cycles/Burst 200. Sheared
826 nuclei were combined, and after adding 700 µl of RIPA buffer, centrifuged at
827 15,000 rpm for 15 min at 4°C to remove insoluble debris. 800 µl of the chromatin-
828 containing supernatant was mixed with 50 µl of Dynabeads protein G bound to
829 9.7 µg of RAD51 antibody (Novus, NB100-148) and incubated overnight on a
830 rotating wheel at 4°C for immunoprecipitation. Beads were washed once with 1
831 ml of cold ChIP wash buffer 1 (0.1% SDS, 1% Triton X-100, 2 mM EDTA, 20 mM
832 Tris-HCl pH 8.0, 150 mM NaCl), 1 ml of cold ChIP wash buffer 2 (0.1% SDS, 1%
833 Triton X-100, 2 mM EDTA, 20 mM Tris-HCl pH 8.0, 500 mM NaCl), 1 ml of cold
834 ChIP wash buffer 3 (0.25 M LiCl, 1% NP-40, 1% sodium deoxycholate, 1 mM
835 EDTA, 10 mM Tris-HCl pH 8.0), and twice with 1 ml of cold TE (1 mM EDTA and
836 10 mM Tris-HCl pH 8.0), followed by elution with 100 µl of elution buffer (0.1 M
837 $NaHCO_3$ and 1% SDS) for 30 min at 65°C with vortexing every 10 min. The elutes

838 were incubated overnight at 65°C for de-crosslinking, neutralized by adding 4 μl
839 of 1M Tris-HCl (pH 6.5) and 2 μl of 0.5 M EDTA, and RNA was digested by adding
840 2 μl of 10 mg/ml RNase-A and incubation for 15 min 37°C. After adding 5 μl of 10
841 mg/ml Proteinase-K (Wako, 165-21043) and incubation for 1 h at 55°C, DNA was
842 purified using QIAquick PCR Purification Kit (QIAGEN).
843 SSDS was performed as described previously (Brick et al., 2018). 7-10 ng
844 of ChIP DNA was further sonicated on the Covaris M220 for 8 min 30 sec at room
845 temperature with a setting of Peak Power 75.0, Duty Factor 10.0, and
846 Cycles/Burst 200, followed by end-repair and dA-tailing using ChIP-Seq Library
847 Prep Reagent Set for Illumina (NEB, E6200L). DNA was incubated for 3 min at
848 95°C and returned to room temperature for kinetic enrichment for single-stranded
849 DNA. After adapter ligation using IDT for Illumina TruSeq DNA UD Indexes
850 (Illumina, 20022370), SSDS libraries were amplified during 15 cycles of PCR
851 using TruSeq DNA Nano LP (Illumina, 20016328), purified with AMPureXP beads
852 (Beckman Coulter, A63880), and sequenced on HiSeq2500 in the rapid mode in
853 a 50 bp PE run. Around 70 million paired reads were generated per sample.
854 A published bioinformatic pipeline (https://nf-co.re/ssds/dev) was run for the
855 resulting reads for the identification of single-stranded sequences and mapping
856 to the mm10 genome [107]. Heatmaps were generated using Deeptools [108].
857
858 **Western blot**
859 Testes were dissected, the tunica albuginea was removed, and seminiferous
860 tubules were snap frozen on liquid nitrogen and stored at -80°C before cell lysis.
861 Tubules from either one testis (*Fignl1*$^{+/+}$ *Stra8-Cre*$^{+}$ and *Fignl1*$^{flox/\Delta}$) or two testes
862 (*Fignl1*$^{flox/\Delta}$ *Stra8-Cre*$^{+}$) were homogenized in 1 ml of RIPA buffer (50 mM Tris-HCl
863 pH 7.5, 150 mM NaCl, 1 mM EDTA, 1% NP-40, 0.5% sodium deoxycholate, 0.1%
864 sodium dodecyl sulfate (SDS)) supplemented with protease inhibitor (Roche,
865 04693159001)) on ice, incubated for 15 min on ice, sonicated with a Bioruptor for
866 30 min (30 cycles of 30 sec ON / 30 sec OFF) at 4°C with a setting of High
867 intensity, and incubated for 15 min on ice. The samples were centrifuged at
868 14,000 rpm for 15 min at 4°C and the supernatants were collected as whole-testis
869 extracts. Protein concentrations were measured by Bradford assay and the
870 concentrations between samples were made constant by adding RIPA buffer
871 supplemented with protease inhibitor. Whole-testis extract was mixed with 4x
872 SDS-PAGE loading buffer (250 mM Tris-HCl pH 6.8, 8% SDS, 40% glycerol, 572
873 mM β-mercaptoethanol, 0.05% bromophenol blue) and boiled for 5 min at 100°C

874 and subjected to immunoblotting.
875 Protein samples were separated on 10% gels by SDS-PAGE and
876 transferred to PVDF membranes by wet transfer method in Towbin buffer (25 mM
877 Tris, 192 mM glycine, 20% ethanol) at 60 V for 150 min at 4°C. Membranes were
878 blocked with PBS containing 2.5% non-fat milk for 1 h at room temperature and
879 incubated with primary antibodies in 2.5% non-fat milk in PBS overnight at 4°C.
880 Membranes were washed three times with PBS containing 0.05% Tween-20
881 (PBST) for 10 min and incubated with HRP-conjugated secondary antibodies in
882 PBST for 1 h at room temperature. Membranes were washed three times with
883 PBST for 10 min and the signal was developed by ECL Prime Western Blotting
884 Detection Reagent (Amersham) and detected by ImageQuant LAS4000 (GE
885 Healthcare).
886
887 **Antibody generation**
888 His-tagged mouse SYCP3 was overexpressed from pET28c-SYCP3 plasmid by
889 the addition of 0.2 mM IPTG in BL21(DE3) at 37°C for 4 h. Cell extracts were
890 prepared in Lysis buffer (50 mM Tris-HCl pH 7.5, 500 mM NaCl) by sonication
891 and the supernatants were collected after centrifugation at 20,400 x *g* for 30 min
892 at 4°C. After adding Tween-20 to a final concentration of 0.2%, the cell lysates
893 were incubated with Ni-NTA Agarose (QIAGEN) for 2 h at 4°C and the lysate-
894 resin slurry was washed in Lysis buffer containing 50 mM Imidazole, 100 mM
895 Imidazole, 300 mM Imidazole. Ni-NTA-bound His-SYCP3 was eluted in Lysis
896 buffer containing 3M Imidazole and 3M Urea (elution 1) by incubation for 1 h at
897 4°C and in Lysis buffer containing 0.1% SDS (elution 2) by incubation for 30 min
898 at room temperature. Elution 2 was concentrated using MICROCON Centrifugal
899 Filter Device YM-10 (Millipore) and subjected to immunization to a rat.
900
901 **Purification of RAD51 and FINGL1ΔN**
902 GST-tagged human FIGNL1ΔN (N-terminal 284 aa deletion) was overexpressed
903 from pGEX-6P-1-*FignI1ΔN* plasmid by the addition of 0.25 mM IPTG in
904 BL21(DE3) pLysS at 30°C for overnight. Cell extracts were prepared in Lysis
905 buffer (25 mM Tris-HCl pH 7.6, 150 mM NaCl, 10% Glycerol, 1 mM DTT) and
906 GST-FIGNL1ΔN was recovered by GSTrap HP column (Cytiva). FIGNL1ΔN was
907 eluted from the GSTrap column by the cleavage of GST tag by Prescission
908 protease (#27-0843-01, Cytiva) in SP buffer (20 mM HEPES-NaOH pH 7.5, 10%
909 Glycerol, 1 mM DTT) supplemented with 100 mM NaCl. FIGNL1ΔN was further

910 purified by HiTrap SP column (Cytiva) with a linear gradient of 100 mM-1M in SP
911 buffer. The peak fractions are dialyzed against SP buffer supplemented with 100
912 mM NaCl, concentrated with Amicon Ultra 30K (Millipore), and stored at -80°C.
913 Human RAD51 was purified as described previously using pET-HsRad51 plasmid
914 [109].
915
916 **Electrophoresis mobility shift assay (EMSA)**
917 Double-stranded DNA substrate was prepared by annealing 5'-Cy5-labeled, 40-
918 mer oligo DNA (Oligo 1, Cy5-
919 TAATACAAAATAAGTAAATGAATAAACAGAGAAAATAAAG, IDT) and its
920 complementary DNA (Oligo 2,
921 CTTTATTTTCTCTGTTTATTCATTTACTTATTTTGTATTA, Fasmac). Oligo 1
922 was used as an ssDNA substrate. For the assay, DNA (0.8 μM in bp/nt) was pre-
923 incubated with 1 μM of RAD51 in 10 μl of the buffer (20 mM HEPES-NaOH pH7.5,
924 100 ug/ml BSA, 1 mM DTT, 10 mM $MgCl_2$, 2 mM ATP) at 37°C for 5 min to form
925 RAD51-DNA complex. Then the indicated concentration of FIGNL1ΔN was added
926 to the reaction and further incubated at 37°C for 15 min. In the control reaction
927 without FIGNL1ΔN, the same volume of dialysis buffer was added instead of the
928 protein. DNA-protein complexes were analyzed using 8% native polyacrylamide
929 gel electrophoresis with 1×TBE. Cy5-labelled DNA was visualized by LAS4000
930 (GE healthcare) and unbound DNA was quantified using ImageQuant TL (GE
931 healthcare). Images were further processed to adjust brightness using Photoshop
932 (Adobe, USA) software.
933
934 **Statistical analysis and reproducibility**
935 Statistical analyses were performed using Graphpad Prism software v.9 and R
936 version 4.2.2 (https://www.r-project.org). Bars in figures and values in
937 manuscripts indicate means ± standard deviations (SDs) otherwise mentioned.
938 Statistic parameters and tests and sample sizes are described in the figures
939 and/or figure legends. Sample sizes were not predetermined using any statistical
940 tests.
941 At least two animals of each genotype were analyzed and similar results
942 were obtained otherwise mentioned. Three independent experiments were
943 performed for biochemical analysis.
944
945 **Data availability**

The raw and processed sequencing data have been deposited in the Gene Expression Omnibus (GEO) repository under accession number GSE227944. Uncropped immunoblotting images and an unprocessed image of electrophoresis mobility shift assay are provided in Source Data. The raw data used in plots and graphs are also provide in Source Data. The raw microscopy images used for figures and quantification are available from corresponding authors upon request.

Code availability

A published bioinformatic pipeline for single-stranded DNA sequencing analysis is available at https://nf-co.re/ssds/dev.

Acknowledgments

We thank Drs. F. Baudat and B. de Massy for sharing unpublished results. We acknowledge Drs. F. Pratto and V. Jayakumar for SSDS analysis. We are grateful to Ms. S. Kondo for the generation of anti-SYCP3. We acknowledge Drs. S. Keeney, Y. Fujiwara, and K. Ishiguro for *spo11* mice and Dr. H. Kurumizaka for the RAD51 expression plasmid. We are also indebted to members of the Shinohara lab, particularly Ms. S. Aoyama, A. Maeda, C. Watanabe, and S. Hashimoto for mouse care. This work was supported by JSPS KAKENHI Grant Numbers; 19H00981 to A.S., 20K15716 and 16H06279 (PAGS) to M.I., and 19H03157 to A.F.

Author contributions

M.I. and A.S. conceived and designed the experiments. M.I. performed all experiments on mouse meiosis. M.I., Y.F., and A.T. analyzed SSDS data. A.F. performed biochemical experiments. K.M. set up Fignl1 mice. M.I. and A.S. analyzed the data. A.S. prepared the original draft and wrote the manuscript with help from M.I.

Competing interest

The authors declare no competing interests.

References

1. Sonoda, E. *et al.* Rad51-deficient vertebrate cells accumulate chromosomal breaks prior to cell death. *EMBO J* **17**, 598-608 (1998).
2. Tashiro, S., Walter, J., Shinohara, A., Kamada, N. & Cremer, T. Rad51 accumulation at sites of DNA damage and in postreplicative chromatin. *J Cell Biol* **150**, 283-291 (2000).
3. Mason, J.M., Chan, Y.L., Weichselbaum, R.W. & Bishop, D.K. Non-enzymatic roles of human RAD51 at stalled replication forks. *Nat Commun* **10**, 4410 (2019).
4. Schlacher, K. *et al.* Double-strand break repair-independent role for BRCA2 in blocking stalled replication fork degradation by MRE11. *Cell* **145**, 529-542 (2011).
5. Ogawa, T., Yu, X., Shinohara, A. & Egelman, E.H. Similarity of the yeast RAD51 filament to the bacterial RecA filament. *Science* **259**, 1896-1899 (1993).
6. Shinohara, A., Ogawa, H. & Ogawa, T. Rad51 protein involved in repair and recombination in S. cerevisiae is a RecA-like protein. *Cell* **69**, 457-470 (1992).
7. Sung, P. Catalysis of ATP-dependent homologous DNA pairing and strand exchange by yeast RAD51 protein. *Science* **265**, 1241-1243 (1994).
8. Sung, P. & Robberson, D.L. DNA strand exchange mediated by a RAD51-ssDNA nucleoprotein filament with polarity opposite to that of RecA. *Cell* **82**, 453-461 (1995).
9. Jensen, R.B., Carreira, A. & Kowalczykowski, S.C. Purified human BRCA2 stimulates RAD51-mediated recombination. *Nature* **467**, 678-683 (2010).
10. Zhao, W. *et al.* BRCA1-BARD1 promotes RAD51-mediated homologous DNA pairing. *Nature* **550**, 360-365 (2017).
11. New, J.H., Sugiyama, T., Zaitseva, E. & Kowalczykowski, S.C. Rad52 protein stimulates DNA strand exchange by Rad51 and replication protein A. *Nature* **391**, 407-410 (1998).
12. Shinohara, A. & Ogawa, T. Stimulation by Rad52 of yeast Rad51-mediated recombination. *Nature* **391**, 404-407 (1998).
13. Van Dyck, E., Stasiak, A.Z., Stasiak, A. & West, S.C. Binding of double-strand breaks in DNA by human Rad52 protein. *Nature* **398**, 728-731 (1999).

1014 14. Akamatsu, Y., Dziadkowiec, D., Ikeguchi, M., Shinagawa, H. & Iwasaki, H.
1015 Two different Swi5-containing protein complexes are involved in mating-
1016 type switching and recombination repair in fission yeast. *Proc Natl Acad*
1017 *Sci U S A* **100**, 15770-15775 (2003).
1018 15. Tsai, S.P. *et al.* Rad51 presynaptic filament stabilization function of the
1019 mouse Swi5-Sfr1 heterodimeric complex. *Nucleic Acids Res* **40**, 6558-
1020 6569 (2012).
1021 16. Masson, J.Y. *et al.* Identification and purification of two distinct complexes
1022 containing the five RAD51 paralogs. *Genes Dev* **15**, 3296-3307 (2001).
1023 17. Abreu, C.M. *et al.* Shu complex SWS1-SWSAP1 promotes early steps in
1024 mouse meiotic recombination. *Nat Commun* **9**, 3961 (2018).
1025 18. Liu, T., Wan, L., Wu, Y., Chen, J. & Huang, J. hSWS1.SWSAP1 is an
1026 evolutionarily conserved complex required for efficient homologous
1027 recombination repair. *J Biol Chem* **286**, 41758-41766 (2011).
1028 19. Martino, J. *et al.* The human Shu complex functions with PDS5B and
1029 SPIDR to promote homologous recombination. *Nucleic Acids Res* **47**,
1030 10151-10165 (2019).
1031 20. Tanaka, K., Kagawa, W., Kinebuchi, T., Kurumizaka, H. & Miyagawa, K.
1032 Human Rad54B is a double-stranded DNA-dependent ATPase and has
1033 biochemical properties different from its structural homolog in yeast,
1034 Tid1/Rdh54. *Nucleic Acids Res* **30**, 1346-1353 (2002).
1035 21. Zhang, Z., Fan, H.Y., Goldman, J.A. & Kingston, R.E. Homology-driven
1036 chromatin remodeling by human RAD54. *Nat Struct Mol Biol* **14**, 397-405
1037 (2007).
1038 22. Liang, F. *et al.* Promotion of RAD51-Mediated Homologous DNA Pairing
1039 by the RAD51AP1-UAF1 Complex. *Cell Rep* **15**, 2118-2126 (2016).
1040 23. Parplys, A.C. *et al.* NUCKS1 is a novel RAD51AP1 paralog important for
1041 homologous recombination and genome stability. *Nucleic Acids Res* **43**,
1042 9817-9834 (2015).
1043 24. Wiese, C. *et al.* Promotion of homologous recombination and genomic
1044 stability by RAD51AP1 via RAD51 recombinase enhancement. *Mol Cell*
1045 **28**, 482-490 (2007).
1046 25. Bugreev, D.V., Mazina, O.M. & Mazin, A.V. Bloom syndrome helicase
1047 stimulates RAD51 DNA strand exchange activity through a novel
1048 mechanism. *J Biol Chem* **284**, 26349-26359 (2009).
1049 26. Bugreev, D.V., Yu, X., Egelman, E.H. & Mazin, A.V. Novel pro- and anti-

1050 recombination activities of the Bloom's syndrome helicase. *Genes Dev* **21**,
1051 3085-3094 (2007).
1052 27. Xue, C. *et al.* Single-molecule visualization of human BLM helicase as it
1053 acts upon double- and single-stranded DNA substrates. *Nucleic Acids Res*
1054 **47**, 11225-11237 (2019).
1055 28. Sommers, J.A. *et al.* FANCJ uses its motor ATPase to destabilize protein-
1056 DNA complexes, unwind triplexes, and inhibit RAD51 strand exchange. *J*
1057 *Biol Chem* **284**, 7505-7517 (2009).
1058 29. Schwendener, S. *et al.* Physical interaction of RECQ5 helicase with
1059 RAD51 facilitates its anti-recombinase activity. *J Biol Chem* **285**, 15739-
1060 15745 (2010).
1061 30. Xue, C. *et al.* Single-molecule visualization of human RECQ5 interactions
1062 with single-stranded DNA recombination intermediates. *Nucleic Acids Res*
1063 **49**, 285-305 (2021).
1064 31. Chu, W.K. *et al.* FBH1 influences DNA replication fork stability and
1065 homologous recombination through ubiquitylation of RAD51. *Nat Commun*
1066 **6**, 5931 (2015).
1067 32. Simandlova, J. *et al.* FBH1 helicase disrupts RAD51 filaments in vitro and
1068 modulates homologous recombination in mammalian cells. *J Biol Chem*
1069 **288**, 34168-34180 (2013).
1070 33. Moldovan, G.L. *et al.* Inhibition of homologous recombination by the
1071 PCNA-interacting protein PARI. *Mol Cell* **45**, 75-86 (2012).
1072 34. Croteau, D.L., Popuri, V., Opresko, P.L. & Bohr, V.A. Human RecQ
1073 helicases in DNA repair, recombination, and replication. *Annu Rev*
1074 *Biochem* **83**, 519-552 (2014).
1075 35. Heyer, W.D., Li, X., Rolfsmeier, M. & Zhang, X.P. Rad54: the Swiss Army
1076 knife of homologous recombination? *Nucleic Acids Res* **34**, 4115-4125
1077 (2006).
1078 36. Scully, R., Panday, A., Elango, R. & Willis, N.A. DNA double-strand break
1079 repair-pathway choice in somatic mammalian cells. *Nat Rev Mol Cell Biol*
1080 **20**, 698-714 (2019).
1081 37. Grey, C. & de Massy, B. Chromosome Organization in Early Meiotic
1082 Prophase. *Front Cell Dev Biol* **9**, 688878 (2021).
1083 38. Ito, M. & Shinohara, A. Chromosome architecture and homologous
1084 recombination in meiosis. *Front Cell Dev Biol* **10**, 1097446 (2022).
1085 39. Yadav, V.K. & Claeys Bouuaert, C. Mechanism and Control of Meiotic DNA

1086 Double-Strand Break Formation in S. cerevisiae. *Front Cell Dev Biol* **9**,
1087 642737 (2021).
1088 40. Bishop, D.K., Park, D., Xu, L. & Kleckner, N. DMC1: a meiosis-specific
1089 yeast homolog of E. coli recA required for recombination, synaptonemal
1090 complex formation, and cell cycle progression. *Cell* **69**, 439-456 (1992).
1091 41. Brown, M.S. & Bishop, D.K. DNA strand exchange and RecA homologs in
1092 meiosis. *Cold Spring Harb Perspect Biol* **7**, a016659 (2014).
1093 42. Crickard, J.B. & Greene, E.C. The biochemistry of early meiotic
1094 recombination intermediates. *Cell Cycle* **17**, 2520-2530 (2018).
1095 43. Deans, B., Griffin, C.S., Maconochie, M. & Thacker, J. Xrcc2 is required
1096 for genetic stability, embryonic neurogenesis and viability in mice. *EMBO*
1097 *J* **19**, 6675-6685 (2000).
1098 44. Kuznetsov, S.G., Haines, D.C., Martin, B.K. & Sharan, S.K. Loss of
1099 Rad51c leads to embryonic lethality and modulation of Trp53-dependent
1100 tumorigenesis in mice. *Cancer Res* **69**, 863-872 (2009).
1101 45. Lim, D.S. & Hasty, P. A mutation in mouse rad51 results in an early
1102 embryonic lethal that is suppressed by a mutation in p53. *Mol Cell Biol* **16**,
1103 7133-7143 (1996).
1104 46. Pittman, D.L. & Schimenti, J.C. Midgestation lethality in mice deficient for
1105 the RecA-related gene, Rad51d/Rad51l3. *Genesis* **26**, 167-173 (2000).
1106 47. Prakash, R. *et al.* XRCC3 loss leads to midgestational embryonic lethality
1107 in mice. *DNA Repair (Amst)* **108**, 103227 (2021).
1108 48. Shu, Z., Smith, S., Wang, L., Rice, M.C. & Kmiec, E.B. Disruption of
1109 muREC2/RAD51L1 in mice results in early embryonic lethality which can
1110 Be partially rescued in a p53(-/-) background. *Mol Cell Biol* **19**, 8686-8693
1111 (1999).
1112 49. Tsuzuki, T. *et al.* Targeted disruption of the Rad51 gene leads to lethality
1113 in embryonic mice. *Proc Natl Acad Sci U S A* **93**, 6236-6240 (1996).
1114 50. Huang, T. *et al.* SPIDR is required for homologous recombination during
1115 mammalian meiosis. *Nucleic Acids Res* **51**, 3855-3868 (2023).
1116 51. Matsuzaki, K., Kondo, S., Ishikawa, T. & Shinohara, A. Human RAD51
1117 paralogue SWSAP1 fosters RAD51 filament by regulating the anti-
1118 recombinase FIGNL1 AAA+ ATPase. *Nat Commun* **10**, 1407 (2019).
1119 52. Prakash, R. *et al.* Distinct pathways of homologous recombination
1120 controlled by the SWS1-SWSAP1-SPIDR complex. *Nat Commun* **12**, 4255
1121 (2021).

1122 53. Chester, N., Kuo, F., Kozak, C., O'Hara, C.D. & Leder, P. Stage-specific
1123 apoptosis, developmental delay, and embryonic lethality in mice
1124 homozygous for a targeted disruption in the murine Bloom's syndrome
1125 gene. *Genes Dev* **12**, 3382-3393 (1998).
1126 54. Wesoly, J. *et al.* Differential contributions of mammalian Rad54 paralogs
1127 to recombination, DNA damage repair, and meiosis. *Mol Cell Biol* **26**, 976-
1128 989 (2006).
1129 55. McNally, F.J. & Roll-Mecak, A. Microtubule-severing enzymes: From
1130 cellular functions to molecular mechanism. *J Cell Biol* **217**, 4057-4069
1131 (2018).
1132 56. Yuan, J. & Chen, J. FIGNL1-containing protein complex is required for
1133 efficient homologous recombination repair. *Proc Natl Acad Sci U S A* **110**,
1134 10640-10645 (2013).
1135 57. Fernandes, J.B. *et al.* FIGL1 and its novel partner FLIP form a conserved
1136 complex that regulates homologous recombination. *PLoS Genet* **14**,
1137 e1007317 (2018).
1138 58. Girard, C. *et al.* AAA-ATPase FIDGETIN-LIKE 1 and Helicase FANCM
1139 Antagonize Meiotic Crossovers by Distinct Mechanisms. *PLoS Genet* **11**,
1140 e1005369 (2015).
1141 59. Hu, Q. *et al.* Meiotic Chromosome Association 1 Interacts with TOP3alpha
1142 and Regulates Meiotic Recombination in Rice. *Plant Cell* **29**, 1697-1708
1143 (2017).
1144 60. Yang, S. *et al.* FIGNL1 Inhibits Non-homologous Chromosome
1145 Association and Crossover Formation. *Front Plant Sci* **13**, 945893 (2022).
1146 61. Kumar, R., Duhamel, M., Coutant, E., Ben-Nahia, E. & Mercier, R.
1147 Antagonism between BRCA2 and FIGL1 regulates homologous
1148 recombination. *Nucleic Acids Res* **47**, 5170-5180 (2019).
1149 62. Sharan, S.K. *et al.* Embryonic lethality and radiation hypersensitivity
1150 mediated by Rad51 in mice lacking Brca2. *Nature* **386**, 804-810 (1997).
1151 63. Sadate-Ngatchou, P.I., Payne, C.J., Dearth, A.T. & Braun, R.E. Cre
1152 recombinase activity specific to postnatal, premeiotic male germ cells in
1153 transgenic mice. *Genesis* **46**, 738-742 (2008).
1154 64. Yuan, L., Brundell, E. & Hoog, C. Expression of the meiosis-specific
1155 synaptonemal complex protein 1 in a heterologous system results in the
1156 formation of large protein structures. *Exp Cell Res* **229**, 272-275 (1996).
1157 65. Yuan, L. *et al.* The murine SCP3 gene is required for synaptonemal

1158 complex assembly, chromosome synapsis, and male fertility. *Mol Cell* **5**,
1159 73-83 (2000).
1160 66. Yuan, L. *et al.* The synaptonemal complex protein SCP3 can form
1161 multistranded, cross-striated fibers in vivo. *J Cell Biol* **142**, 331-339 (1998).
1162 67. Mahadevaiah, S.K. *et al.* Recombinational DNA double-strand breaks in
1163 mice precede synapsis. *Nat Genet* **27**, 271-276 (2001).
1164 68. Luo, M. *et al.* MEIOB exhibits single-stranded DNA-binding and
1165 exonuclease activities and is essential for meiotic recombination. *Nat*
1166 *Commun* **4**, 2788 (2013).
1167 69. Souquet, B. *et al.* MEIOB targets single-strand DNA and is necessary for
1168 meiotic recombination. *PLoS Genet* **9**, e1003784 (2013).
1169 70. Yoshida, K. *et al.* The mouse RecA-like gene Dmc1 is required for
1170 homologous chromosome synapsis during meiosis. *Mol Cell* **1**, 707-718
1171 (1998).
1172 71. Shi, B. *et al.* Dual functions for the ssDNA-binding protein RPA in meiotic
1173 recombination. *PLoS Genet* **15**, e1007952 (2019).
1174 72. Moens, P.B. *et al.* The time course and chromosomal localization of
1175 recombination-related proteins at meiosis in the mouse are compatible
1176 with models that can resolve the early DNA-DNA interactions without
1177 reciprocal recombination. *J Cell Sci* **115**, 1611-1622 (2002).
1178 73. Baker, S.M. *et al.* Involvement of mouse Mlh1 in DNA mismatch repair and
1179 meiotic crossing over. *Nat Genet* **13**, 336-342 (1996).
1180 74. Ashley, T. *et al.* Dynamic changes in Rad51 distribution on chromatin
1181 during meiosis in male and female vertebrates. *Chromosoma* **104**, 19-28
1182 (1995).
1183 75. Ikeya, T., Shinohara, A., Sato, S., Tabata, S. & Ogawa, T. Localization of
1184 mouse Rad51 and Lim15 proteins on meiotic chromosomes at late stages
1185 of prophase 1. *Genes Cells* **1**, 379-389 (1996).
1186 76. Tarsounas, M., Morita, T., Pearlman, R.E. & Moens, P.B. RAD51 and
1187 DMC1 form mixed complexes associated with mouse meiotic
1188 chromosome cores and synaptonemal complexes. *J Cell Biol* **147**, 207-
1189 220 (1999).
1190 77. Baudat, F., Manova, K., Yuen, J.P., Jasin, M. & Keeney, S. Chromosome
1191 synapsis defects and sexually dimorphic meiotic progression in mice
1192 lacking Spo11. *Mol Cell* **6**, 989-998 (2000).
1193 78. Romanienko, P.J. & Camerini-Otero, R.D. The mouse Spo11 gene is

1194 required for meiotic chromosome synapsis. *Mol Cell* **6**, 975-987 (2000).
1195 79. Zhang, Q. *et al.* The FLIP-FIGNL1 complex regulates the dissociation of
1196 RAD51/DMC1 in homologous recombination and replication fork restart.
1197 *Nucleic Acids Res* (2023).
1198 80. Hinch, A.G. *et al.* The Configuration of RPA, RAD51, and DMC1 Binding
1199 in Meiosis Reveals the Nature of Critical Recombination Intermediates.
1200 *Mol Cell* **79**, 689-701 e610 (2020).
1201 81. Khil, P.P., Smagulova, F., Brick, K.M., Camerini-Otero, R.D. & Petukhova,
1202 G.V. Sensitive mapping of recombination hotspots using sequencing-
1203 based detection of ssDNA. *Genome Res* **22**, 957-965 (2012).
1204 82. Smagulova, F. *et al.* Genome-wide analysis reveals novel molecular
1205 features of mouse recombination hotspots. *Nature* **472**, 375-378 (2011).
1206 83. Altmannova, V. *et al.* The role of bivalent ions in the regulation of D-loop
1207 extension mediated by DMC1 during meiotic recombination. *iScience* **25**,
1208 105439 (2022).
1209 84. Li, X. & Heyer, W.D. RAD54 controls access to the invading 3'-OH end
1210 after RAD51-mediated DNA strand invasion in homologous recombination
1211 in Saccharomyces cerevisiae. *Nucleic Acids Res* **37**, 638-646 (2009).
1212 85. Li, X., Stith, C.M., Burgers, P.M. & Heyer, W.D. PCNA is required for
1213 initiation of recombination-associated DNA synthesis by DNA polymerase
1214 delta. *Mol Cell* **36**, 704-713 (2009).
1215 86. Bugreev, D.V. *et al.* The resistance of DMC1 D-loops to dissociation may
1216 account for the DMC1 requirement in meiosis. *Nat Struct Mol Biol* **18**, 56-
1217 60 (2011).
1218 87. Finsterbusch, F. *et al.* Alignment of Homologous Chromosomes and
1219 Effective Repair of Programmed DNA Double-Strand Breaks during
1220 Mouse Meiosis Require the Minichromosome Maintenance Domain
1221 Containing 2 (MCMDC2) Protein. *PLoS Genet* **12**, e1006393 (2016).
1222 88. Her, C., Wu, X., Bailey, S.M. & Doggett, N.A. Mouse MutS homolog 4 is
1223 predominantly expressed in testis and interacts with MutS homolog 5.
1224 *Mamm Genome* **12**, 73-76 (2001).
1225 89. Kneitz, B. *et al.* MutS homolog 4 localization to meiotic chromosomes is
1226 required for chromosome pairing during meiosis in male and female mice.
1227 *Genes Dev* **14**, 1085-1097 (2000).
1228 90. Li, X.C. & Schimenti, J.C. Mouse pachytene checkpoint 2 (trip13) is
1229 required for completing meiotic recombination but not synapsis. *PLoS*

1230 *Genet* **3**, e130 (2007).
1231 91. Lutzmann, M. *et al.* MCM8- and MCM9-deficient mice reveal
1232 gametogenesis defects and genome instability due to impaired
1233 homologous recombination. *Mol Cell* **47**, 523-534 (2012).
1234 92. McNairn, A.J., Rinaldi, V.D. & Schimenti, J.C. Repair of Meiotic DNA
1235 Breaks and Homolog Pairing in Mouse Meiosis Requires a
1236 Minichromosome Maintenance (MCM) Paralog. *Genetics* **205**, 529-537
1237 (2017).
1238 93. Roig, I. *et al.* Mouse TRIP13/PCH2 is required for recombination and
1239 normal higher-order chromosome structure during meiosis. *PLoS Genet* **6**
1240 (2010).
1241 94. Benson, F.E., Stasiak, A. & West, S.C. Purification and characterization of
1242 the human Rad51 protein, an analogue of E. coli RecA. *EMBO J* **13**, 5764-
1243 5771 (1994).
1244 95. Dupaigne, P. *et al.* Rad51 polymerization reveals a new chromatin
1245 remodeling mechanism. *PLoS One* **3**, e3643 (2008).
1246 96. North, J.A. *et al.* ATP-dependent nucleosome unwrapping catalyzed by
1247 human RAD51. *Nucleic Acids Res* **41**, 7302-7312 (2013).
1248 97. Senavirathne, G., Mahto, S.K., Hanne, J., O'Brian, D. & Fishel, R. Dynamic
1249 unwrapping of nucleosomes by HsRAD51 that includes sliding and
1250 rotational motion of histone octamers. *Nucleic Acids Res* **45**, 685-698
1251 (2017).
1252 98. Holzen, T.M., Shah, P.P., Olivares, H.A. & Bishop, D.K. Tid1/Rdh54
1253 promotes dissociation of Dmc1 from nonrecombinogenic sites on meiotic
1254 chromatin. *Genes Dev* **20**, 2593-2604 (2006).
1255 99. Shah, P.P. *et al.* Swi2/Snf2-related translocases prevent accumulation of
1256 toxic Rad51 complexes during mitotic growth. *Mol Cell* **39**, 862-872 (2010).
1257 100. Mason, J.M. *et al.* RAD54 family translocases counter genotoxic effects of
1258 RAD51 in human tumor cells. *Nucleic Acids Res* **43**, 3180-3196 (2015).
1259 101. Kiianitsa, K., Solinger, J.A. & Heyer, W.D. Rad54 protein exerts diverse
1260 modes of ATPase activity on duplex DNA partially and fully covered with
1261 Rad51 protein. *J Biol Chem* **277**, 46205-46215 (2002).
1262 102. Kiianitsa, K., Solinger, J.A. & Heyer, W.D. Terminal association of Rad54
1263 protein with the Rad51-dsDNA filament. *Proc Natl Acad Sci U S A* **103**,
1264 9767-9772 (2006).
1265 103. Solinger, J.A., Kiianitsa, K. & Heyer, W.D. Rad54, a Swi2/Snf2-like

1266 recombinational repair protein, disassembles Rad51:dsDNA filaments.
1267 *Mol Cell* **10**, 1175-1188 (2002).
1268 104. Tokuhiro, K. *et al.* Calreticulin is required for development of the cumulus
1269 oocyte complex and female fertility. *Sci Rep* **5**, 14254 (2015).
1270 105. de Boer, E., Lhuissier, F.G. & Heyting, C. Cytological analysis of
1271 interference in mouse meiosis. *Methods Mol Biol* **558**, 355-382 (2009).
1272 106. Peters, A.H., Plug, A.W., van Vugt, M.J. & de Boer, P. A drying-down
1273 technique for the spreading of mammalian meiocytes from the male and
1274 female germline. *Chromosome Res* **5**, 66-68 (1997).
1275 107. Brick, K., Pratto, F., Sun, C.Y., Camerini-Otero, R.D. & Petukhova, G.
1276 Analysis of Meiotic Double-Strand Break Initiation in Mammals. *Methods*
1277 *Enzymol* **601**, 391-418 (2018).
1278 108. Ramirez, F. *et al.* deepTools2: a next generation web server for deep-
1279 sequencing data analysis. *Nucleic Acids Res* **44**, W160-165 (2016).
1280 109. Matsuo, Y., Sakane, I., Takizawa, Y., Takahashi, M. & Kurumizaka, H.
1281 Roles of the human Rad51 L1 and L2 loops in DNA binding. *FEBS J* **273**,
1282 3148-3159 (2006).
1283 110. Lange, J. *et al.* The Landscape of Mouse Meiotic Double-Strand Break
1284 Formation, Processing, and Repair. *Cell* **167**, 695-708 e616 (2016).
1285 111. Boekhout, M. *et al.* REC114 Partner ANKRD31 Controls Number, Timing,
1286 and Location of Meiotic DNA Breaks. *Mol Cell* **74**, 1053-1068 e1058 (2019).
1287
1288

1289 **Figure legends**

1290

1291 **Fig. 1. Defective spermatogenesis in *Fignl1* cKO mice.**

1292 (a) Scheme of mouse *Fignl1 flox* and *Δ* alleles. Yellow and blue boxes and black
1293 triangles represent untranslated regions (UTRs), coding sequence (CDS), and
1294 *loxP* sequences, respectively.

1295 (b) Representative image of testes in *Fignl1*$^{+/+}$ *Stra8-Cre*$^{+}$ (left) and *Fignl1*$^{flox/\Delta}$
1296 *Stra8-Cre*$^{+}$ (right) mice.

1297 (c) Testis weights of mice with different combinations of genotypes. Adult testes
1298 (9-20 weeks) were analyzed. The red bars are means.

1299 (d) Immunoblotting of FIGNL1 from whole-testis extracts of mice with different
1300 genotypes. α-tubulin is a loading control.

1301 (e) Sperm numbers in *Fignl1*$^{+/+}$ *Stra8-Cre*$^{+}$ (black circles) and *Fignl1*$^{flox/\Delta}$ *Stra8-*
1302 *Cre*$^{+}$ (blue open circles) mice. Sperms from adult Cauda epididymis (11-17
1303 weeks) were counted. The red bars are means.

1304 (f) Representative images of seminiferous tubule sections from the testis of
1305 *Fignl1*$^{+/+}$ *Stra8-Cre*$^{+}$ (Ctrl) and *Fignl1*$^{flox/\Delta}$ *Stra8-Cre*$^{+}$ (*Fignl1* cKO) mice. The
1306 sections were stained with periodic acid-Schiff (PAS). Sg, spermatogonia; Sc (L),
1307 leptotene spermatocytes; Sc (P), pachytene spermatocytes; St, spermatids.

1308 (g) Distribution of different meiotic prophase I stages in Ctrl (gray bars) and *Fignl1*
1309 cKO (blue open bars). >100 cells were counted from each animal. The red bars
1310 are SDs from three animals of each genotype.

1311 (h) Distribution of FIGNL1-positive and -negative cells at different meiotic
1312 prophase I stages in Ctrl (gray bars) and *Fignl1* cKO (blue open bars). Squashed
1313 testicular cells were immunostained for FIGNL1, γH2AX, and SYCP3. >100
1314 leptotene/zygotene cells (with pan-nuclear γH2AX staining) and
1315 pachytene/diplotene cells (with the sex body-specific γH2AX staining) were
1316 analyzed from each animal. The means of two mice of each genotype are
1317 indicated. Lept., leptonema; Zyg., zygonema; Pach., pachynema; dipl.,
1318 diplonema. Representative images of testicular cell squashes are shown in
1319 Supplementary Fig. 1b.

1320 (i) Representative images of spermatocyte-chromosome spreads immunostained
1321 for SYCP1 (green) and SYCP3 (magenta) at zygonema in Ctrl and *Fignl1* cKO.
1322 The bottom panels are magnified images of regions with yellow dotted rectangles.

1323 (j) Quantification of the frequency of synapsis defects in Ctrl (gray bars) and
1324 *Fignl1* cKO (blue open bars). >90 cells were analyzed from each animal. The red

1325 bars are SDs from three mice of each genotype.
1326 In (f)-(i), genotypes of indicated animals are Ctrl, *Fignl1*$^{+/+}$ *Stra8-Cre*$^{+}$; *Fignl1* cKO,
1327 *Fignl1*$^{flox/\Delta}$ *Stra8-Cre*$^{+}$. The results of unpaired *t*-tests are indicated in the graphs:
1328 ****$p \leq 0.0001$.
1329 Scale bars, 50 μm in (f) and 10 μm for whole-nucleus images and 2 μm for
1330 magnified images in (i).
1331
1332 **Fig. 2. Deregulated meiotic recombination in *Fignl1* cKO spermatocytes.**
1333 (a) Representative images of spermatocyte-chromosome spreads
1334 immunostained for RPA2 (white in the top panels and green in the bottom panels)
1335 and SYCP3 (magenta) at indicated meiotic prophase I stages in Ctrl and *Fignl1*
1336 cKO.
1337 (b) Quantification of RPA2 focus numbers at different meiotic prophase I stages
1338 in Ctrl (black circles) and *Fignl1* cKO (blue open circles). The red bars are means.
1339 (c) Representative images of spermatocyte-chromosome spreads
1340 immunostained for MSH4 (white in the left panels and green in the right panels),
1341 SYCP1 (magenta) and SYCP3 (blue) at mid-zygonema in Ctrl and *Fignl1* cKO.
1342 The bottom panels are magnified images of regions with dotted yellow.
1343 (d) Quantification of MSH4 focus numbers at mid-zygonema in Ctrl (black circles)
1344 and *Fignl1* cKO (blue open circles). The red bars are means.
1345 (e) The correlation between MSH4 focus number and total SC length at mid-
1346 zygonema in Ctrl (black circles) and *Fignl1* cKO (blue open circles). Pearson's *r*
1347 is shown in parentheses. A black solid line and a blue dashed line indicate linear
1348 regression for Ctrl and *Fignl1* cKO, respectively.
1349 (f) Quantification of MSH4 focus density on the SCs at mid-zygonema in Ctrl
1350 (black circles) and *Fignl1* cKO (blue open circles). The red bars are means. In (e)
1351 and (f), mid-zygotene nuclei with 40-120 μm of total SC length per nucleus were
1352 analyzed.
1353 Genotypes of indicated animals are: Ctrl, *Fignl1*$^{+/+}$ *Stra8-Cre*$^{+}$; *Fignl1* cKO,
1354 *Fignl1*$^{flox/\Delta}$ *Stra8-Cre*$^{+}$. The results of the Mann-Whitney *U*-test are indicated in
1355 the graphs: ****$p \leq 0.0001$. The total number of cells analyzed is indicated below
1356 the graphs.
1357 Scale bars in (a) and (c), 10 μm and 2 μm for magnified images in (c).
1358
1359 **Fig. 3. Accumulation of RAD51 and DMC1 in meiotic prophase I in *Fignl1***
1360 **cKO spermatocytes.**

1361 (a) Representative images of spermatocyte-chromosome spreads
1362 immunostained for DMC1 (white in the top panels and green in the bottom panels)
1363 and SYCP3 (magenta) at indicated meiotic prophase I stages in Ctrl and *Fignl1*
1364 cKO.
1365 (b) Quantification of DMC1 focus numbers at different meiotic prophase I stages
1366 in Ctrl (black circles) and *Fignl1* cKO (blue open circles). The red bars are means.
1367 (c) Representative images of spermatocyte-chromosome spreads
1368 immunostained for RAD51 (white in the top panels and green in the bottom
1369 panels) and SYCP3 (magenta) at indicated meiotic prophase I stages in Ctrl and
1370 *Fignl1* cKO.
1371 (d) Quantification of RAD51 focus numbers at different meiotic prophase I stages
1372 in Ctrl (black circles) and *Fignl1* cKO (blue open circles). The red bars are means.
1373 (e) Quantification of focus numbers of RAD51 (green), DMC1 (magenta), and
1374 RAD51-DMC1 colocalization (brown) at different meiotic prophase I stages in Ctrl
1375 (filled circles) and *Fignl1* cKO (open circles). The black bars are means.
1376 Representative images of spermatocyte-chromosome spreads are shown in
1377 Supplementary Fig. 7.
1378 (f) Quantification of the frequency of RAD51-DMC1 colocalization at different
1379 meiotic prophase I stages in Ctrl (filled circles) and *Fignl1* cKO (open circles). The
1380 degrees of RAD51 foci colocalizing with DMC1 (left, green) and DMC1 foci
1381 colocalizing with RAD51 (right, magenta) are shown. The black bars are means.
1382 Genotypes of indicated animals are Ctrl, *Fignl1*$^{+/+}$ *Stra8-Cre*$^{+}$; *Fignl1* cKO,
1383 *Fignl1*$^{flox/\Delta}$ *Stra8-Cre*$^{+}$. The results of the Mann-Whitney *U*-test are indicated in
1384 the graphs: ****$p \leq 0.0001$. The total number of cells analyzed is indicated below
1385 the graphs.
1386 Scale bars in (a) and (c), 10 μm. Prelept., preleptonema; lept., leptonema; zyg.,
1387 zygonema.
1388
1389 **Fig. 4. Accumulation of RAD51 and DMC1 in preleptotene *Fignl1* cKO**
1390 **spermatocytes.**
1391 (a) Representative images of spermatocyte-chromosome spreads
1392 immunostained for RAD51 (left), SYCP3 (middle) and EdU (right) at
1393 preleptonema in Ctrl and *Fignl1* cKO.
1394 (b) Quantification of RAD51 focus numbers at preleptonema in Ctrl (black circles)
1395 and *Fignl1* cKO (blue open circles). The red solid bars and dashed bars are
1396 means for total cells and RAD51-positive cells (with >10 RAD51 foci; 26/38 and

1397 25/48 cells in early and mid/late preleptonema, respectively), respectively.
1398 (c) Representative images of spermatocyte-chromosome spreads
1399 immunostained for DMC1 (left), SYCP3 (middle), and EdU (right) at
1400 preleptonema in Ctrl and *Fignl1* cKO.
1401 (d) Quantification of DMC1 focus numbers at preleptonema in Ctrl (black circles)
1402 and *Fignl1* cKO (blue open circles). The red solid bars and dashed bars are
1403 means for total cells and DMC1-positive cells (with >30 DMC1 foci; 28/39 and
1404 26/45 cells in early and mid/late preleptonema, respectively), respectively.
1405 Genotypes of indicated animals are Ctrl, *Fignl1*$^{+/+}$ *Stra8-Cre*$^{+}$; *Fignl1* cKO,
1406 *Fignl1*$^{flox/\Delta}$ *Stra8-Cre*$^{+}$. The results of the Mann-Whitney *U*-test are indicated in
1407 the graphs: ****$p \leq 0.0001$. The total number of cells analyzed is indicated below
1408 the graphs.
1409 Scale bars in (a) and (c), 10 μm.
1410
1411 **Fig. 5. SPO11-independent accumulation of RAD51 and DMC1 in *Fignl1* cKO**
1412 **spermatocytes.**
1413 (a) Representative images of spermatocyte-chromosome spreads
1414 immunostained for RAD51 (white in the top panels and green in the bottom
1415 panels) and SYCP3 (magenta) at leptonema in *Spo11* KO, *Fignl1* cKO and *Spo11*
1416 KO *Fignl1* cKO.
1417 (b) Quantification of RAD51 focus numbers at different meiotic prophase I stages
1418 in *Spo11* KO (orange circles), *Fignl1* cKO (blue open circles), and *Spo11* KO
1419 *Fignl1* cKO (purple open circles). The red bars are means. Cells in which Stra8-
1420 Cre recombinase seemed to fail excision of the *Fignl1*$^{\Delta}$ allele in *Spo11* KO *Fignl1*
1421 cKO (<30 RAD51 foci) are excluded. Quantification including these cells is shown
1422 in Supplementary Fig. 8a.
1423 (c) Representative images of spermatocyte-chromosome spreads
1424 immunostained for DMC1 (white in the top panels and green in the bottom panels)
1425 and SYCP3 (magenta) at early zygonema in *Spo11* KO, *Fignl1* cKO and *Spo11*
1426 KO *Fignl1* cKO.
1427 (d) Quantification of DMC1 focus numbers at different meiotic prophase I stages
1428 in *Spo11* KO (orange circles), *Fignl1* cKO (blue open circles), and *Spo11* KO
1429 *Fignl1* cKO (purple open circles). The red bars are means. Cells in which Stra8-
1430 Cre recombinase seemed to fail excision of the *Fignl1*$^{\Delta}$ allele in *Spo11* KO *Fignl1*
1431 cKO (<60 DMC1 foci) are excluded. Quantification including these cells is shown
1432 in Supplementary Fig. 8b.

1433 (e) Representative images of spermatocyte-chromosome spreads
1434 immunostained for RAD51 (green), DMC1 (magenta), and SYCP3 (blue) at late
1435 zygonema/early leptonema in *Spo11* KO *Fignl1* cKO. The bottom panels are
1436 magnified images of regions with yellow dotted rectangles.
1437 (f) Quantification of focus numbers of RAD51 (green open circles), DMC1
1438 (magenta open circles), and RAD51-DMC1 colocalization (brawn open circles) at
1439 different meiotic prophase I stages in *Spo11* KO *Fignl1* cKO. The black bars are
1440 means.
1441 (g) Quantification of the frequency of RAD51-DMC1 colocalization at different
1442 meiotic prophase I stages in *Spo11* KO *Fignl1* cKO. The degrees of RAD51 foci
1443 colocalizing with DMC1 (left, green open circles) and DMC1 foci colocalizing with
1444 RAD51 (right, magenta open circles) are shown. The black bars are means.
1445 Genotypes of indicated animals are: *Spo11* KO, *Spo11*$^{-/-}$ *Fignl1*$^{flox/\Delta}$; *Fignl1* cKO,
1446 *Fignl1*$^{flox/\Delta}$ *Stra8-Cre*$^{+}$; *Spo11* KO *Fignl1* cKO, *Spo11*$^{-/-}$ *Fignl1*$^{flox/\Delta}$ *Stra8-Cre*$^{+}$. The
1447 results of the Mann-Whitney *U*-test are indicated in the graphs: ****$p \leq 0.0001$.
1448 The total number of cells analyzed is indicated below the graphs.
1449 Scale bars in (a), (c) and (e), 10 μm and 2 μm for magnified images in (e). Prelept.,
1450 preleptonema; lept., leptonema; zyg., zygonema.
1451
1452 **Fig. 6. Persistent RAD51 binding at recombination sites in *Fignl1* cKO**
1453 **spermatocytes.**
1454 (a) RAD51 ChIP-SSDS signals (green) in Ctrl and *Fignl1* cKO with Spo11-oligo
1455 counts (blue) and DMC1 ChIP-SSDS signals (black) in wild-type at an indicated
1456 chromosomal region with a hotspot on mouse chromosome 2.
1457 (b) The heatmap of RAD51 ChIP-SSDS signals (green) in Ctrl and *Fignl1* cKO
1458 and Spo11-oligo counts (blue) and DMC1 ChIP-SSDS signals (black) in wild-type.
1459 The 4,000 most active meiotic recombination hotspots on autosomes identified
1460 by Spo11-oligo in wild-type are ordered by SPO11-oligos counts [110]. ChIP-SSDS
1461 signals are centered relative to hotspot centers. In (a) and (b), Spo11-oligo and
1462 DMC1 ChIP-SSDS data are from previous studies [110, 111].
1463 (c) Representative images of spermatocyte-chromosome spreads
1464 immunostained for RAD51 (green), RPA2 (magenta), and SYCP3 (blue) at mid-
1465 zygonema in Ctrl and *Fignl1* cKO. The bottom panels are magnified images of
1466 regions with yellow dotted rectangles. Scale bars, 10 μm for whole-nucleus
1467 images and 2 μm for magnified images.
1468 (d) Quantification of focus numbers of RAD51 (green), RPA2 (magenta) and

1469 RAD51-RPA2 colocalization (brawn) at mid zygonema in Ctrl (filled circles) and
1470 *Fignl1* cKO (open circles). The black bars are means.
1471 (e) Quantification of the frequency of RAD51-RPA2 colocalization at mid-
1472 zygonema in Ctrl (black circles) and *Fignl1* cKO (blue open circles). The degree
1473 of RPA2 foci colocalizing with RAD51 is shown. The red bars are means.
1474 Genotypes of indicated animals are: Ctrl, *Fignl1*$^{+/+}$ *Stra8-Cre*$^{+}$; *Fignl1* cKO,
1475 *Fignl1*$^{flox/\Delta}$ *Stra8-Cre*$^{+}$. The results of the Mann-Whitney *U*-test are indicated: ****p
1476 ≤ 0.0001. The total number of cells analyzed is indicated below the graphs.
1477
1478 **Fig. 7. *Fignl1* deficiency rescues defects in RAD51 and DMC1 assembly**
1479 **caused by *Swsap1* deficiency.**
1480 (a) Representative images of spermatocyte-chromosome spreads
1481 immunostained for RAD51 (white in the top panels and green in the bottom
1482 panels) and SYCP3 (magenta) at early zygonema in Ctrl, *Swsap1* KO*, Fignl1*
1483 cKO and *Swsap1* KO *Fignl1* cKO.
1484 (b) Quantification of RAD51 focus numbers at different meiotic prophase I stages
1485 in Ctrl (black circles), *Swsap1* KO (orange circles), *Fignl1* cKO (blue open circles),
1486 and *Swsap1* KO *Fignl1* cKO (purple open circles). The red bars are means.
1487 (c) Representative images of spermatocyte-chromosome spreads
1488 immunostained for DMC1 (white in the top panels and green in the bottom panels)
1489 and SYCP3 (magenta) at early zygonema in Ctrl, *Swsap1* KO*, Fignl1* cKO, and
1490 *Swsap1* KO *Fignl1* cKO.
1491 (d) Quantification of DMC1 focus numbers at different meiotic prophase I stages
1492 in Ctrl (black circles), *Swsap1* KO (orange circles), *Fignl1* cKO (blue open circles),
1493 and *Swsap1* KO *Fignl1* cKO (purple open circles). The red bars are means.
1494 Genotypes of indicated animals are *Swsap1* KO, *Swsap1*$^{-/-}$ *Fignl1*$^{flox/\Delta}$; *Fignl1*
1495 cKO, *Fignl1*$^{flox/\Delta}$ *Stra8-Cre*$^{+}$; *Swsap1* KO *Fignl1* cKO, *Swsap1*$^{-/-}$ *Fignl1*$^{flox/\Delta}$ *Stra8-*
1496 *Cre*$^{+}$. The results of the Mann-Whitney *U*-test are indicated in the graphs: ****p ≤
1497 0.0001. The total number of cells analyzed is indicated below the graphs.
1498 Scale bars in (a) and (c), 10 μm.
1499
1500 **Fig. 8. FIGNL1 disrupts RAD51-DNA complexes.**
1501 (a) Electrophoresis mobility shift assay showing *in vitro* disruption of RAD51-DNA
1502 complexes by FIGNL1. A representative gel image among triplicate is shown.
1503 Human RAD51 protein was incubated with either Cy5-labelled ssDNA (40nt) or
1504 dsDNA (40bp) in the presence of ATP. After the formation of the protein-DNA

complex, purified human FINGL1ΔN was added at the indicated concentration and further incubated. The complexes were analyzed by polyacrylamide gel electrophoresis and the fluorescence from the DNAs was captured.
(b) Quantification of free ssDNA or dsDNA in (A). The red bars are means and SDs from three independent experiments.
(c) Model of FIGNL1 function in spermatocytes. In pre-meiotic S-phase and early meiotic prophase I, FIGNL1 dissociates RAD51 and DMC1 from dsDNAs. At meiotic DSB sites, FIGNL1 removes RAD51 and DMC1 from ssDNAs, which facilitates efficient loading of MutSγ (MSH4-MSH5) and further processing of homologous recombination to crossover outcome.

Supplementary information

Supplementary Figures legends

Supplementary Fig. 1. Depletion of FIGNL1 from early meiotic prophase I spermatocytes, related to Fig. 1.
(a) Representative images of testicular cell squashes immunostained for FIGNL1 (green), PLZF (top, magenta) and SYCP3 (bottom, magenta), counterstained for DNA with DAPI (blue). Cells in yellow dotted circles with condensed DAPI bodies are Sertoli cells or round spermatids. Scale bars, 10 μm.
(b) Representative images of testicular cell squashes immunostained for FIGNL1 (green), γH2AX (blue), and SYCP3 (magenta) in Ctrl (*Fignl1*$^{+/+}$ *Stra8-Cre*$^{+}$) and *Fignl1* cKO (*Fignl1*$^{flox/\Delta}$ *Stra8-Cre*$^{+}$). SYCP3-positive prophase I spermatocytes were categorized into two by γH2AX staining: leptotene/zygotene cells (L/Z) and pachytene/diplotene cells (P/D) show pan-nuclear γH2AX staining and the sex body-specific γH2AX staining, respectively. Scale bars, 10 μm.

Supplementary Fig. 2. Deregulated meiotic recombination in *Fignl1* cKO spermatocytes, related to Fig. 2.
(a) Representative images of spermatocyte-chromosome spreads immunostained for γH2AX (white in the top panels and green in the bottom panels) and SYCP3 (magenta) at indicated meiotic prophase I stages in Ctrl and *Fignl1* cKO.
(b) Quantification of γH2AX intensity at different meiotic prophase I stages in Ctrl (black circles) and *Fignl1* cKO (blue open circles). Two independent experiments

1541 showed reduced (left; pooled results from two animals of each genotype) and one
1542 experiment showed similar (right) levels of γH2AX intensity in *Fignl1* cKO
1543 spermatocytes compared to Ctrl. The red bars are means. The results of the
1544 Mann-Whitney *U*-tests are indicated: ****$p \leq 0.0001$. The total number of cells
1545 analyzed is indicated below the graphs.
1546 (c) Representative images of spermatocyte-chromosome spreads
1547 immunostained for MLH1 (white in the top panels and green in the bottom panels),
1548 SYCP1 (magenta), and SYCP3 (blue) at late pachynema in Ctrl and late
1549 zygonema (pachynema-like) in *Fignl1* cKO. The right panels are magnified
1550 images of regions with yellow dotted rectangles.
1551 Genotypes of indicated animals are Ctrl, *Fignl1*$^{+/+}$ *Stra8-Cre*$^{+}$; *Fignl1* cKO,
1552 *Fignl1*$^{flox/\Delta}$ *Stra8-Cre*$^{+}$.
1553 Scale bars in (a) and (c), 10 μm and 2 μm for magnified images in (c).
1554
1555 **Supplementary Fig. 3. Reduced focus intensity of RAD51 and DMC1 in**
1556 ***Fignl1* cKO spermatocytes, related to Fig. 3.**
1557 (a) Quantification of focus intensities of RAD51 at different meiotic prophase I
1558 stages in Ctrl (black circles) and *Fignl1* cKO (blue open circles). The red bars are
1559 means ± SDs. The total number of cells analyzed is 35 and 26 at leptonema and
1560 early zygonema in Ctrl, respectively; 54 and 30 at leptonema and early zygonema
1561 in *Fignl1* cKO, respectively.
1562 (b) Quantification of focus intensities of DMC1 at different meiotic prophase I
1563 stages in Ctrl (black circles) and *Fignl1* cKO (blue open circles). The red bars are
1564 means ± SDs. The total number of cells analyzed is 64 and 22 at leptonema and
1565 early zygonema in Ctrl, respectively; 61 and 33 at leptonema and early zygonema
1566 in *Fignl1* cKO, respectively.
1567 Genotypes of indicated animals are Ctrl, *Fignl1*$^{+/+}$ *Stra8-Cre*$^{+}$; *Fignl1* cKO,
1568 *Fignl1*$^{flox/\Delta}$ *Stra8-Cre*$^{+}$. The results of the Mann-Whitney *U*-test are indicated in
1569 the graphs: ****$p \leq 0.0001$. The total number of foci analyzed is indicated below
1570 the graphs.
1571
1572 **Supplementary Fig. 4. Infrequent localization of RAD51 at ongoing**
1573 **replication fork in preleptotene *Fignl1* cKO spermatocytes, related to Fig. 4.**
1574 (a) Representative images of spermatocyte-chromosome spreads
1575 immunostained for IdU (green), RAD51 (magenta), and SYCP3 at early
1576 preleptonema in Ctrl and *Fignl1* cKO. The bottom panels are magnified images

1577 of regions with yellow dotted rectangles. Scale bars, 10 μm for whole-nucleus
1578 images and 2 μm for magnified images.
1579 (b) Quantification of focus numbers of IdU (green open circles), RAD51 (magenta
1580 open circles), and IdU-RAD51 colocalization (brawn open circles) at early
1581 preleptonema in *Fignl1* cKO. The black bars are means.
1582 (c) Quantification of the frequency of IdU-RAD51 colocalization at early
1583 preleptonema in *Fignl1* cKO. The degrees of IdU foci colocalizing with RAD51
1584 (left, green open circles) and RAD51 foci colocalizing with IdU (right, magenta
1585 open circles) are shown. The black bars are means. The colocalization frequency
1586 was measured with and without rotating the IdU image 90° clockwise relative to
1587 the RAD51 image.
1588 (d) Comparison of the frequency of IdU-RAD51 (10' IdU labeling) and EdU-
1589 RAD51 (60' EdU labeling) colocalization at early preleptonema in *Fignl1* cKO.
1590 The degrees of RAD51 foci colocalizing with IdU (left, magenta open circles) and
1591 RAD51 foci colocalizing with EdU (right, magenta open triangles) are shown. The
1592 black bars are means.
1593 Genotypes of indicated animals are Ctrl, *Fignl1*$^{+/+}$ *Stra8-Cre*$^{+}$; *Fignl1* cKO,
1594 *Fignl1*$^{flox/\Delta}$ *Stra8-Cre*$^{+}$. The results of the Mann-Whitney *U*-test are indicated in
1595 the graphs: ****$p \leq 0.0001$. The total number of cells analyzed is indicated below
1596 the graphs.
1597
1598 **Supplementary Fig. 5. Infrequent localization of DMC1 at ongoing**
1599 **replication fork in preleptotene *Fignl1* cKO spermatocytes, related to Fig. 4.**
1600 (a) Representative images of spermatocyte-chromosome spreads
1601 immunostained for EdU (green), DMC1 (magenta), and SYCP3 at early
1602 preleptonema in Ctrl and *Fignl1* cKO. The bottom panels are magnified images
1603 of regions with yellow dotted rectangles. Scale bars, 10 μm for whole-nucleus
1604 images and 2 μm for magnified images.
1605 (b) Quantification of focus numbers of EdU (green open circles), DMC1 (magenta
1606 open circles), and EdU-DMC1 colocalization (brawn open circles) at early
1607 preleptonema in *Fignl1* cKO. The black bars are means.
1608 (c) Quantification of the frequency of EdU-DMC1 colocalization at early
1609 preleptonema in *Fignl1* cKO. The degrees of EdU foci colocalizing with DMC1
1610 (left, green open circles) and DMC1 foci colocalizing with EdU (right, magenta
1611 open circles) are shown. The black bars are means. The colocalization frequency
1612 was measured with and without rotating the EdU image 90° clockwise relative to

1613 the DMC1 image.
1614 Genotypes of indicated animals are Ctrl, *Fignl1*$^{+/+}$ *Stra8-Cre*$^{+}$; *Fignl1* cKO,
1615 *Fignl1*$^{flox/\Delta}$ *Stra8-Cre*$^{+}$. The results of the Mann-Whitney *U*-test are indicated in
1616 the graphs. The total number of cells analyzed is indicated below the graphs.
1617
1618 **Supplementary Fig. 6. Largely normal pre-meiotic DNA replication in *Fignl1***
1619 **cKO spermatocytes, related to Fig. 4.**
1620 (a) Representative images of spermatocyte-chromosome spreads
1621 immunostained for RPA2 (left), SYCP3 (middle) and EdU (right) at preleptonema
1622 in Ctrl and *Fignl1* cKO. Scale bars, 10 μm.
1623 (b) Quantification of RPA2 focus numbers at early preleptonema in Ctrl (black
1624 circles) and *Fignl1* cKO (blue open circles). The red bars are means.
1625 (c) Quantification of IdU focus numbers (10' IdU labeling) at early preleptonema
1626 in Ctrl (black circles) and *Fignl1* cKO (blue open circles). The red bars are means.
1627 Genotypes of indicated animals are Ctrl, *Fignl1*$^{+/+}$ *Stra8-Cre*$^{+}$; *Fignl1* cKO,
1628 *Fignl1*$^{flox/\Delta}$ *Stra8-Cre*$^{+}$. The results of the Mann-Whitney *U*-test are indicated in
1629 the graphs. The total number of cells analyzed is indicated below the graphs.
1630
1631 **Supplementary Fig. 7. Uncoupled loading of RAD51 and DMC1 in *Fignl1***
1632 **cKO spermatocytes, related to Fig. 3 and 4.**
1633 Representative images of spermatocyte-chromosome spreads immunostained
1634 for RAD51 (green), DMC1 (magenta), and SYCP3 (blue) at indicated meiotic
1635 prophase I stages in Ctrl (*Fignl1*$^{+/+}$ *Stra8-Cre*$^{+}$) and *Fignl1* cKO (*Fignl1*$^{flox/\Delta}$ *Stra8-*
1636 *Cre*$^{+}$). The bottom panels are magnified images of regions with yellow dotted
1637 rectangles. Scale bars, 10 μm for whole-nucleus images and 2 μm for magnified
1638 images.
1639
1640 **Supplementary Fig. 8. Accumulation of RAD51 and DMC1 with low levels of**
1641 **γH2AX and few RPA2 foci in *Spo11* KO *Fignl1* cKO spermatocytes, related**
1642 **to Fig. 5.**
1643 (a) Quantification of RAD51 focus numbers at different meiotic prophase I stages
1644 in *Spo11* KO (orange circles), *Fignl1* cKO (blue open circles), and *Spo11* KO
1645 *Fignl1* cKO (purple open circles). The red bars are means.
1646 (b) Quantification of DMC1 focus numbers at different meiotic prophase I stages
1647 in *Spo11* KO (orange circles), *Fignl1* cKO (blue open circles), and *Spo11* KO
1648 *Fignl1* cKO (purple open circles). The red bars are means.

1649 (c) Representative images of spermatocyte-chromosome spreads
1650 immunostained for γH2AX (green), SYCP3 (magenta), and RAD51 (white in
1651 insets) at indicated meiotic prophase I stages in *Fignl1* cKO, *Spo11* KO and
1652 *Spo11* KO *Fignl1* cKO. Scale bars, 10 μm.
1653 (d) Quantification of γH2AX intensity at different meiotic prophase I stages in
1654 *Fignl1* cKO (blue open circles), *Spo11* KO (orange circles), and *Spo11* KO *Fignl1*
1655 cKO (purple open circles). The red bars are means.
1656 (e) Representative images of spermatocyte-chromosome spreads
1657 immunostained for RPA2 (green) and SYCP3 (magenta) at early leptonema in
1658 *Spo11* KO and *Spo11* KO *Fignl1* cKO. Scale bars, 10 μm.
1659 (f) Quantification of RPA2 focus numbers at early leptonema in *Spo11* KO
1660 (orange circles) and *Spo11* KO *Fignl1* cKO (purple open circles). The red bars
1661 are means.
1662 Genotypes of indicated animals are: *Spo11* KO, *Spo11*$^{-/-}$ *Fignl1*$^{flox/\Delta}$; *Fignl1* cKO,
1663 *Fignl1*$^{flox/\Delta}$ *Stra8-Cre*$^{+}$; *Spo11* KO *Fignl1* cKO, *Spo11*$^{-/-}$ *Fignl1*$^{flox/\Delta}$ *Stra8-Cre*$^{+}$. The
1664 results of the Mann-Whitney *U*-test are indicated in the graphs: ****$p \leq 0.0001$.
1665 The total number of cells analyzed is indicated below the graphs.
1666
1667 **Supplementary Fig. 9. RAD51 binding at recombination sites in *Fignl1* cKO**
1668 **spermatocytes, related to Fig. 6.**
1669 (a) RAD51 ChIP-SSDS signals (green) in Ctrl and *Fignl1* cKO with Spo11-oligo
1670 counts (blue) and DMC1 ChIP-SSDS signals (black) in wild-type at an indicated
1671 chromosomal region with multiple hotspots on mouse chromosome 3.
1672 (b) The heatmap of RAD51 ChIP-SSDS signals (green) in Ctrl and *Fignl1* cKO
1673 and Spo11-oligo counts (blue) and DMC1 ChIP-SSDS signals (black) in wild-type,
1674 as shown in Fig. 6b. Three mice of each genotype were analyzed and two RAD51
1675 antibodies with different lot numbers were used for ChIP. The results of Ctrl #1
1676 and *Fignl1* cKO #1 are shown in Fig. 6a, b, Supplementary Fig. 9a.
1677 (c) Comparison of RAD51 ChIP-SSDS signals at meiotic recombination hotspots.
1678 Each spot represents the sum of RAD51 ChIP-SSDS signals around ±2,000 bp
1679 of one of the 4,000 most active meiotic recombination hotspots on autosomes
1680 (black) used for heatmap representation in Fig. 6b and Supplementary Fig. 9b
1681 and 163 active hotspots on sex chromosomes (magenta) with similar Spo11-oligo
1682 counts as the 4,000 active autosomal hotspots in wild-type [110]. Pearson's *r* for
1683 autosomal hotspots is also shown.
1684 (d) Metaplots of RAD51 ChIP-SSDS signals around meiotic recombination

1685 hotspots. Smoothed RAD51 ChIP-SSDS signals in Ctrl (top) and *Fignl1* cKO
1686 (bottom) around ±2,000 bp of the 4,000 most active meiotic recombination
1687 hotspots on autosomes used for heatmap representation are shown. Three mice
1688 of each genotype were analyzed. Black, orange and blue lines represent the
1689 results of #1, #2 and #3, respectively.
1690 Genotypes of indicated animals are: Ctrl, *Fignl1*$^{+/+}$ *Stra8-Cre*$^{+}$; *Fignl1* cKO,
1691 *Fignl1*$^{flox/\Delta}$ *Stra8-Cre*$^{+}$.
1692
1693 **Supplementary Fig. 10. RAD51 binding in *Spo11* KO and *Spo11* KO *Fignl1***
1694 **cKO spermatocytes, related to Fig. 6.**
1695 (a) The heatmap of RAD51 ChIP-SSDS signals (green) in *Spo11* KO and *Spo11*
1696 KO *Fignl1* cKO and Spo11-oligo counts (blue) and DMC1 ChIP-SSDS signals
1697 (black) in wild-type, as shown in Fig. 6b. Two mice of each genotype were
1698 analyzed.
1699 (b) Metaplots of RAD51 ChIP-SSDS signals around meiotic recombination
1700 hotspots. Smoothed RAD51 ChIP-SSDS signals in *Spo11* KO (left) and *Spo11*
1701 KO *Fignl1* cKO (right) around ±2,000 bp of the 4,000 most active meiotic
1702 recombination hotspots on autosomes used for heatmap representation are
1703 shown. Two mice of each genotype were analyzed. Black and blue lines
1704 represent the results of #1 and #2, respectively.
1705 (c) Comparison of RAD51 ChIP-SSDS profiles in the entire genome. Mouse
1706 genome was divided into non-overlapping 2-kb bins and top 1,000 bins with the
1707 highest RAD51 ChIP-SSDS signals were analyzed. The 1,000 bins were either
1708 categorized into three: high (>50), middle (50-20) and low (<20), based on sum
1709 RAD51 ChIP-SSDS signals in each bin (left) or two: overlapping with previously
1710 identified DMC1 ChIP-SSDS hotspots [1] and non-overlapping (right). The
1711 frequency of each category was plotted for each animal of Ctrl (black open
1712 circles), *Fignl1* cKO (blue open circles), *Spo11* KO (orange circles), and *Spo11*
1713 KO *Fignl1* cKO (purple open circles). The means of three (Ctrl and *Fignl1* cKO)
1714 or two (*Spo11* KO and *Spo11* KO *Fignl1* cKO) mice of each genotype are
1715 indicated.
1716 (d) Comparison of RAD51 ChIP-SSDS profiles in *Spo11* KO and *Spo11* KO
1717 *Fignl1* cKO. 262 bins with high or middle RAD51 ChIP-SSDS signals in both two
1718 of *Spo11* KO *Fignl1* cKO mice in (c) were categorized into high, middle, and low
1719 RAD51 ChIP SSDS signals in either of two *Spo11* KO mice by the same criteria
1720 as (c).

1721 Genotypes of indicated animals are: Ctrl, *Fignl1*$^{+/+}$ *Stra8-Cre*$^{+}$; *Fignl1* cKO,
1722 *Fignl1*$^{flox/\Delta}$ *Stra8-Cre*$^{+}$; *Spo11* KO, *Spo11*$^{-/-}$ *Stra8-Cre*$^{+}$; *Spo11* KO *Fignl1* cKO,
1723 *Spo11*$^{-/-}$ *Fignl1*$^{flox/\Delta}$ *Stra8-Cre*$^{+}$.
1724

1725 **Supplementary Table 1. Primers used for genotyping in this study**

1726

Primer	Sequence (5'->3')
1727 *Fignl1* wild-type and flox allele, forward	TATCCATATTGGGTGTCTCCTGTTAC
1728 *Fignl1* wild-type and flox allele, reverse	TAGCACACACACACTGGATATAACT
1729 *Fignl1* deletion allele, forward	CCGAGTATCCATATTGGGTG
1730 *Fignl1* deletion allele, reverse	TGTCTGCTGTAGTCATGAGG
1731 *Stra8-Cre* transgenic allele, forward	CTCCAAGGGGGTAAGGTGTAGC
1732 *Stra8-Cre* transgenic allele, reverse	TTCCAGGGCGCGAGTTGATAG
1733 *Swsap1* wild-type allele, forward	GAGATATCGCTTTTGATTGGTC
1734 *Swsap1* wild-type allele, reverse	GAATTGAGGATGGGTACTGG
1735 *Swsap1* deletion allele, forward	CGGTTTCCATATGGGGATTGGTGGCGACGA
1736 *Swsap1* deletion allele, reverse	TGCCTTATTTCCTGATCCAGGCTAGCTGTC
1737 *Spo11* wild-type allele, forward	TGAGATACATGGAGGAAGATGG
1738 *Spo11* deletion allele, forward	CTGAGCCCAGAAAGCGAAGGAA
1739 *Spo11,* common reverse	ATGTTAGTCGGCACAGCAGTAG

1740

1741 **Supplementary Table 2. Antibodies used in this study**

1742

Antibody	Source	Identifier	Application	Dilution
1743 Rat anti-SYCP3 (Serum)	this study	N/A	IF	1:5,000
1744 Mouse anti-SYCP3	Abcam	ab97672	IF	1:750
1745 Rabbit anti-SYCP1	Novus Biologicals	NB300-229	IF	1:500
1746 Mouse anti-MLH1	BD Pharmingen	51-1327QR	IF	1:50
1747 Rabbit anti-MSH4	Abcam	ab58666	IF	1:200
1748 Rabbit anti-RPA2	Abcam	ab76420	IF	1:200
1749 Rat anti-RPA2	Cell Signaling	2208	IF	1:100
1750 Mouse anti-γH2AX	Millipore	05-636	IF	1:500
1751 Rabbit anti-DMC1	Santa Cruz	sc-22768	IF	1:200
1752 Rabbit anti-RAD51	Santa Cruz	sc-8349	IF	1:100
1753 Mouse anti-RAD51	Novus Biologicals	NB100-148	IF, ChIP	1:100
1754 Mouse anti-BrdU	BD Biosciences	BD347580	IF	1:200
1755 Mouse anti-PLZF	Santa Cruz	sc-28319	IF	1:100
1756 Rabbit anti-FIGNL1	Proteintech	17604-1-AP	IF	1:100

			IB	1:1,000
Mouse anti-α tubulin	SIGMA	T6074	IB	1:3,000
Goat anti-mouse 488	Molecular Probes	A-11029	IF	1:1,000
Goat anti-rabbit 488	Molecular Probes	A-11034	IF	1:1,000
Goat anti-rat 488	Molecular Probes	A-11006	IF	1:1,000
Goat anti-mouse 594	Molecular Probes	A-11032	IF	1:1,000
Goat anti-rat 594	Molecular Probes	A-11007	IF	1:1,000
Goat anti-rabbit 647	Molecular Probes	A-21245	IF	1:500
Goat anti-rabbit IgG-HRP	Southern Biotech	4030-05	IB	1:10,000
Goat anti-mouse IgG-HRP	Thermo Scientific	31430	IB	1:10.000

IF, immunofluorescence; IB, immunoblotting.; ChIP, chromatin immunoprecipitation

Supplementary References

1. Brick, K., Smagulova, F., Khil, P., Camerini-Otero, R.D. & Petukhova, G.V. Genetic recombination is directed away from functional genomic elements in mice. *Nature* **485**, 642-645 (2012).

Ito et al., Figure 1

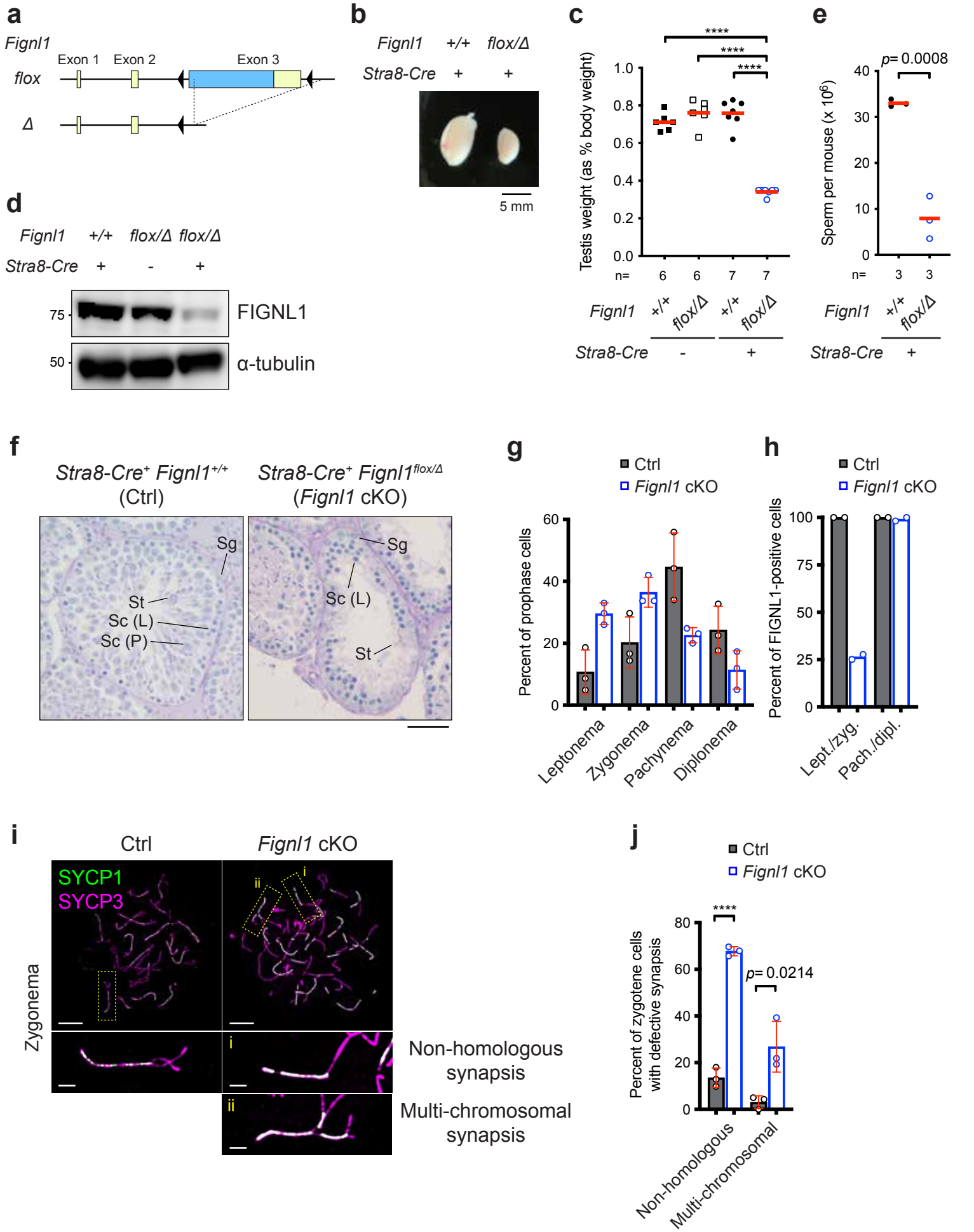

Ito et al., Figure 2

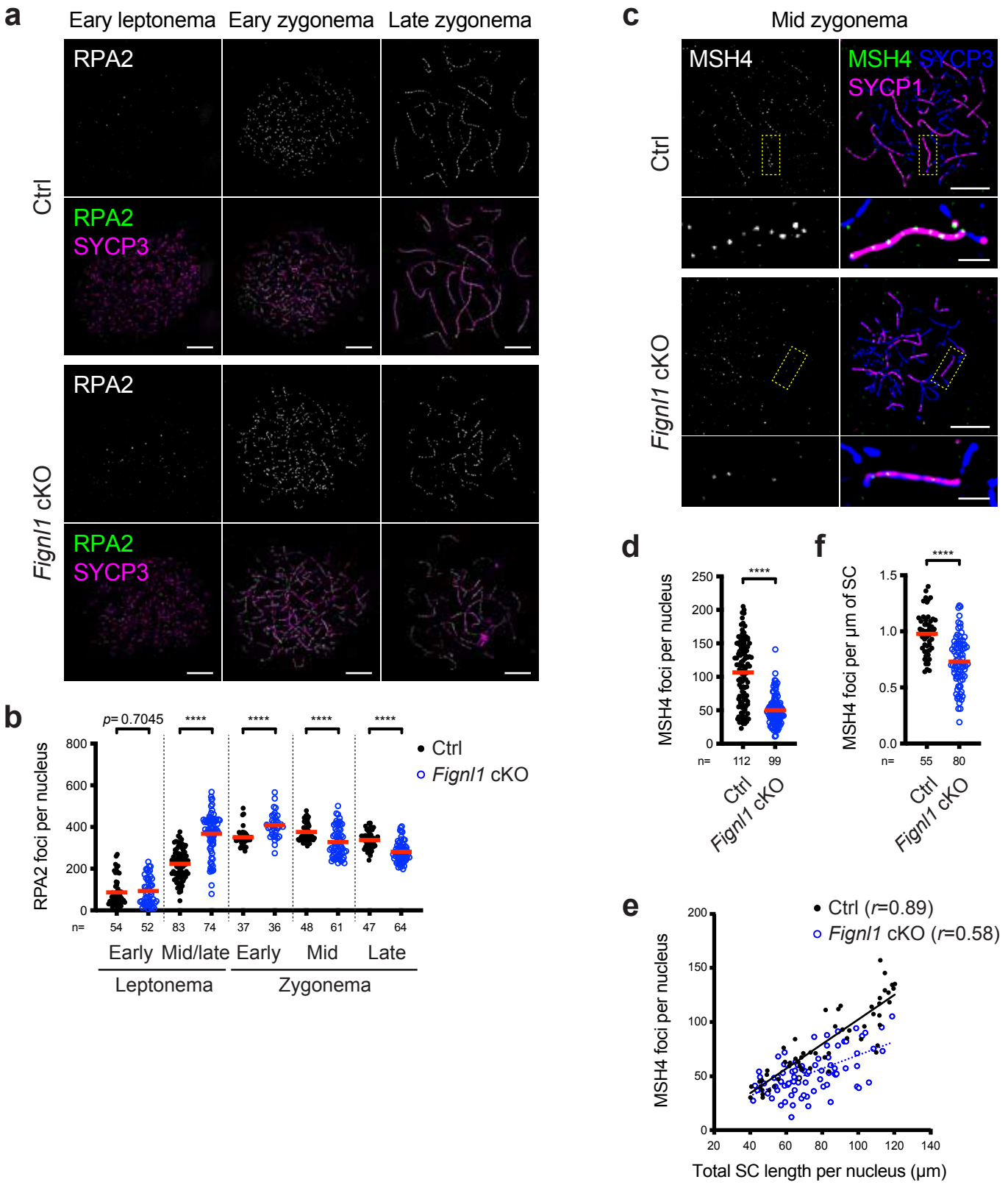

Ito et al., Figure 3

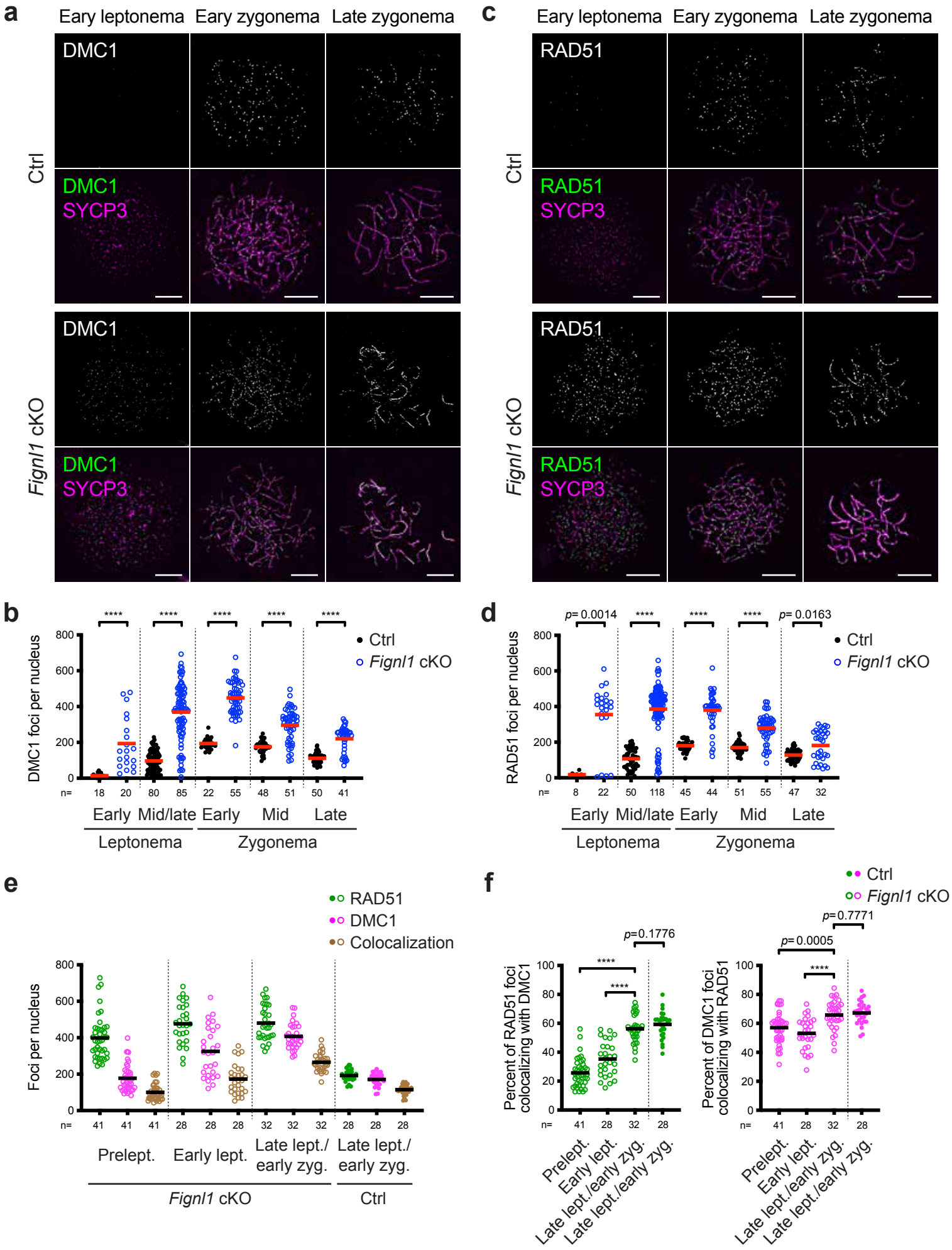

Ito et al., Figure 4

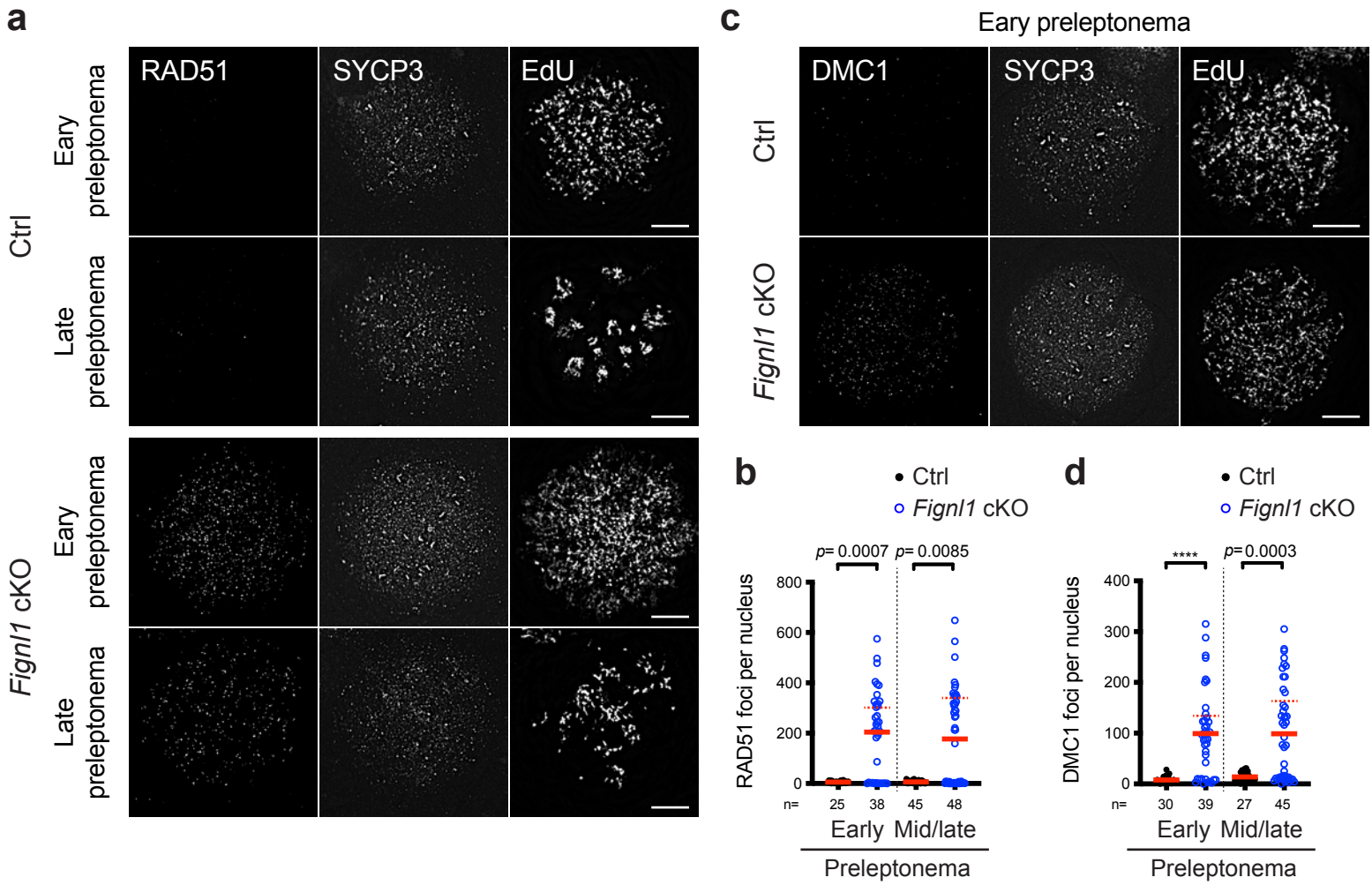

Ito et al., Figure 5

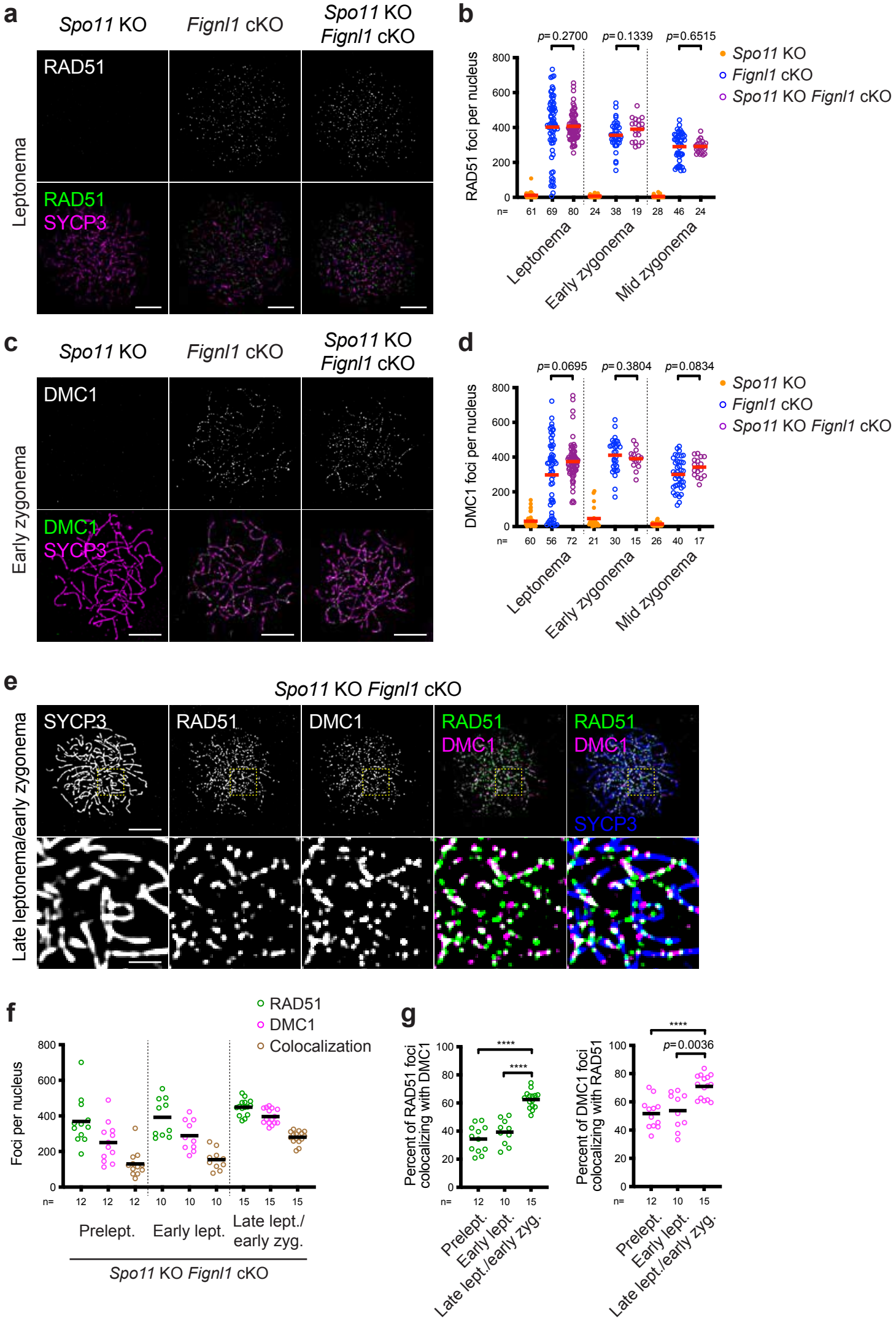

Ito et al., Figure 6

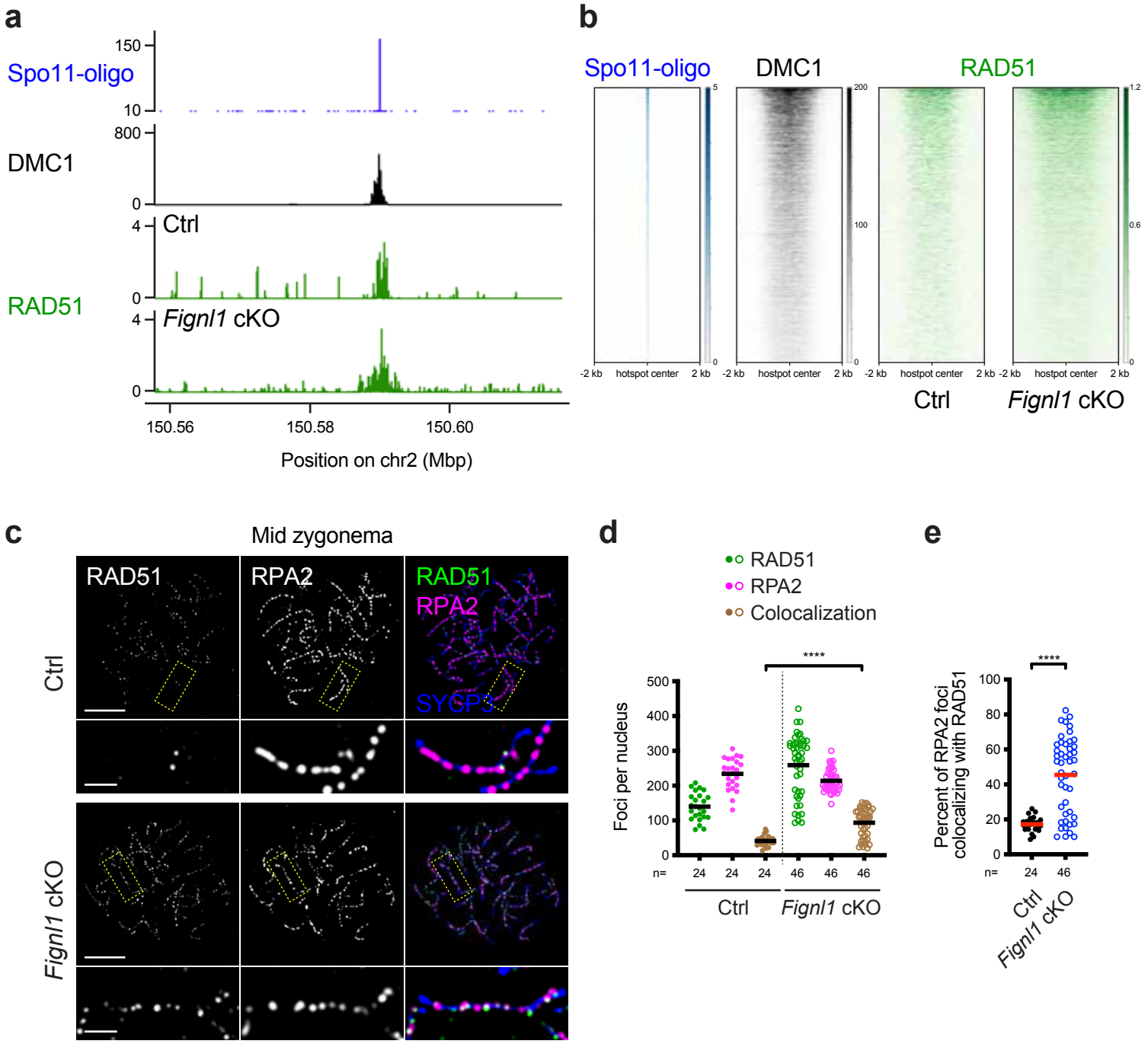

Ito et al., Figure 7

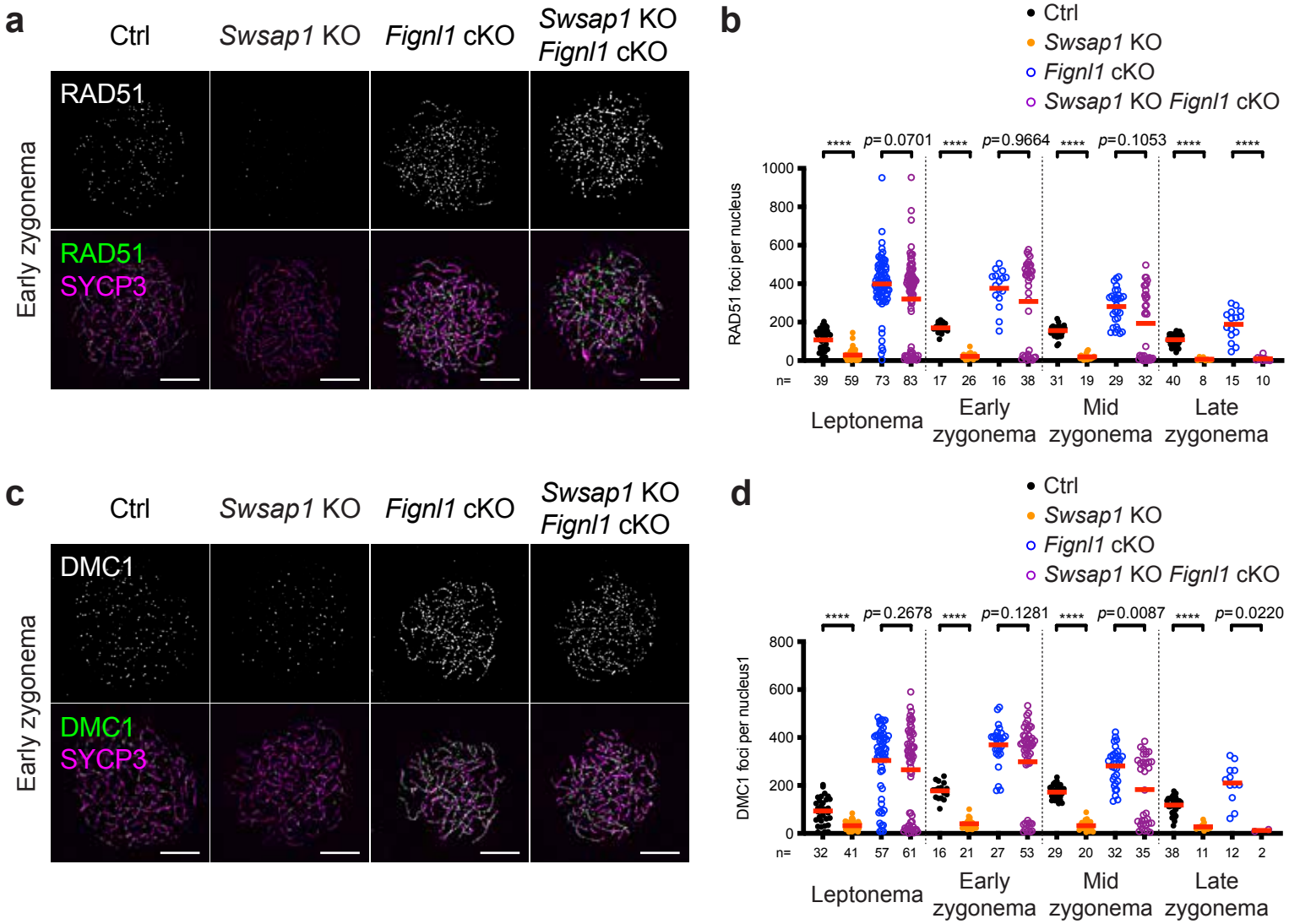

Ito et al., Figure 8

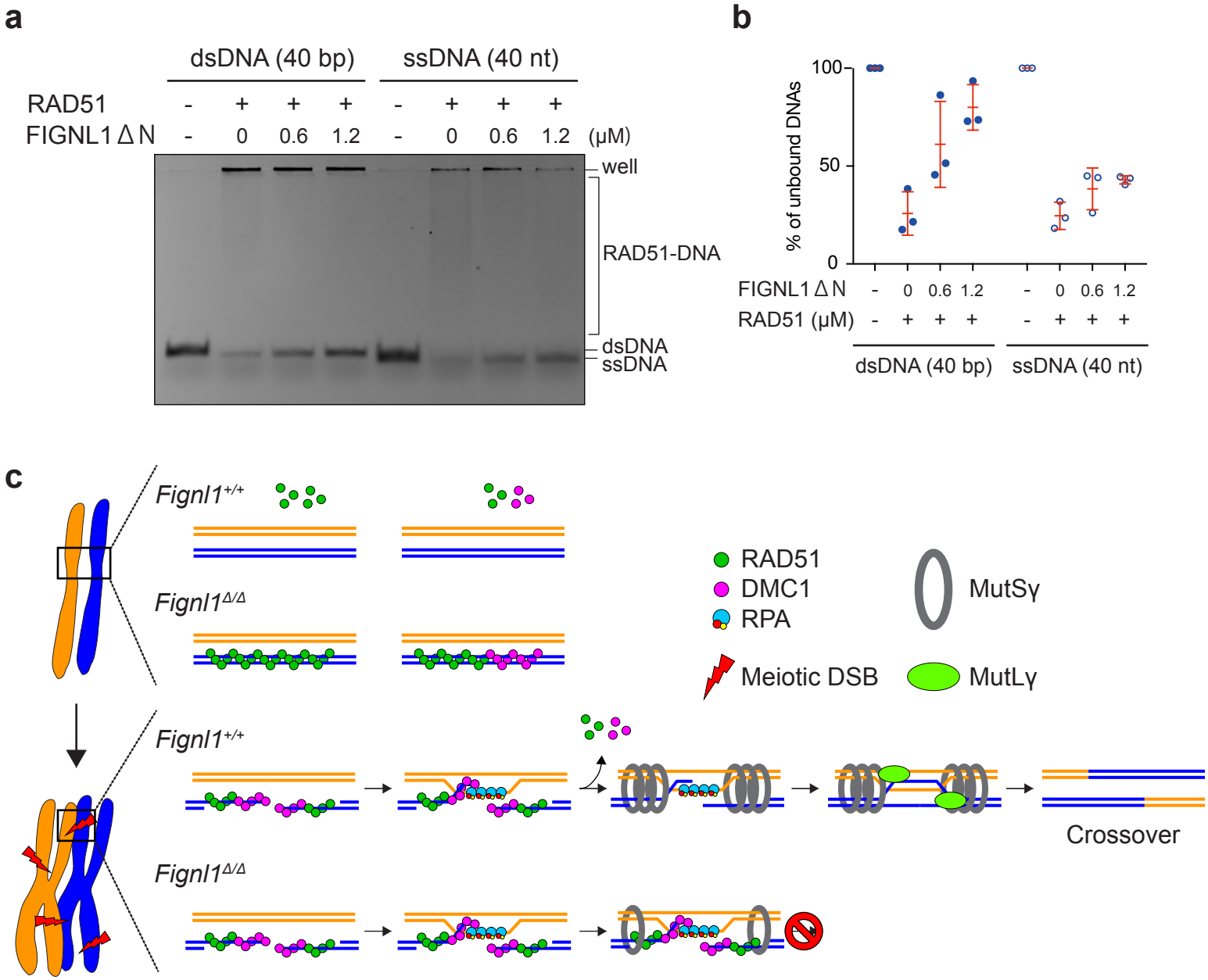

Ito et al., Supplementary Figure 1

a

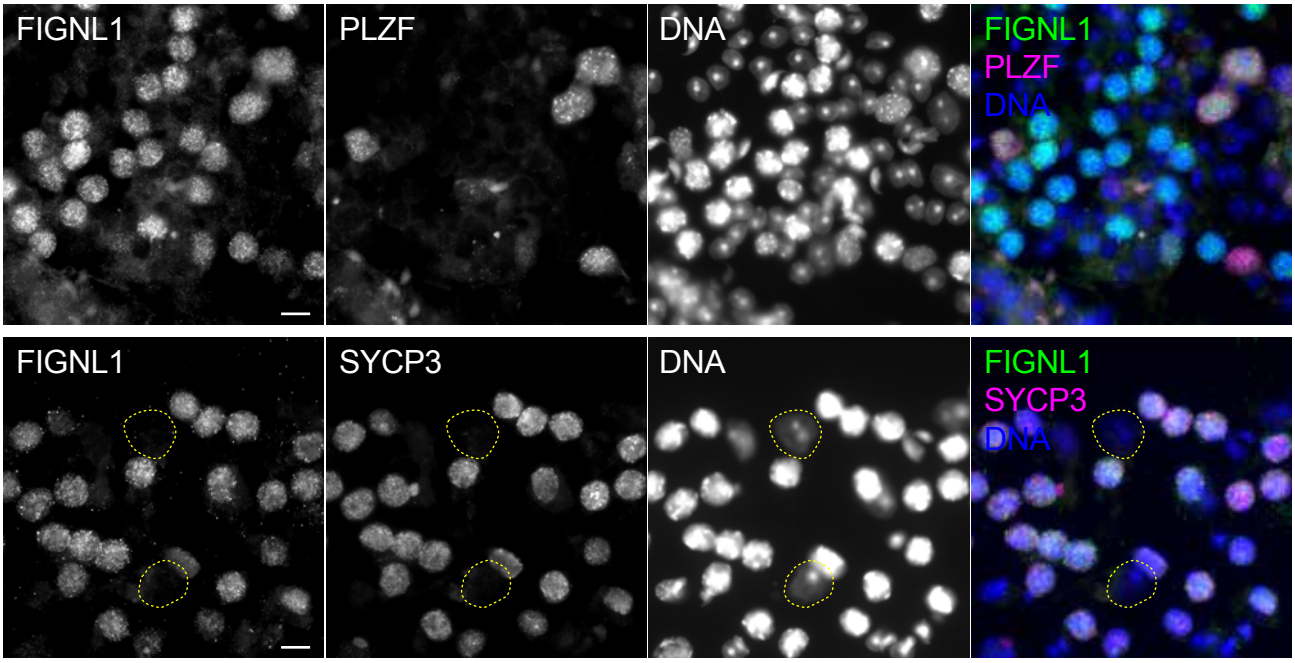

b

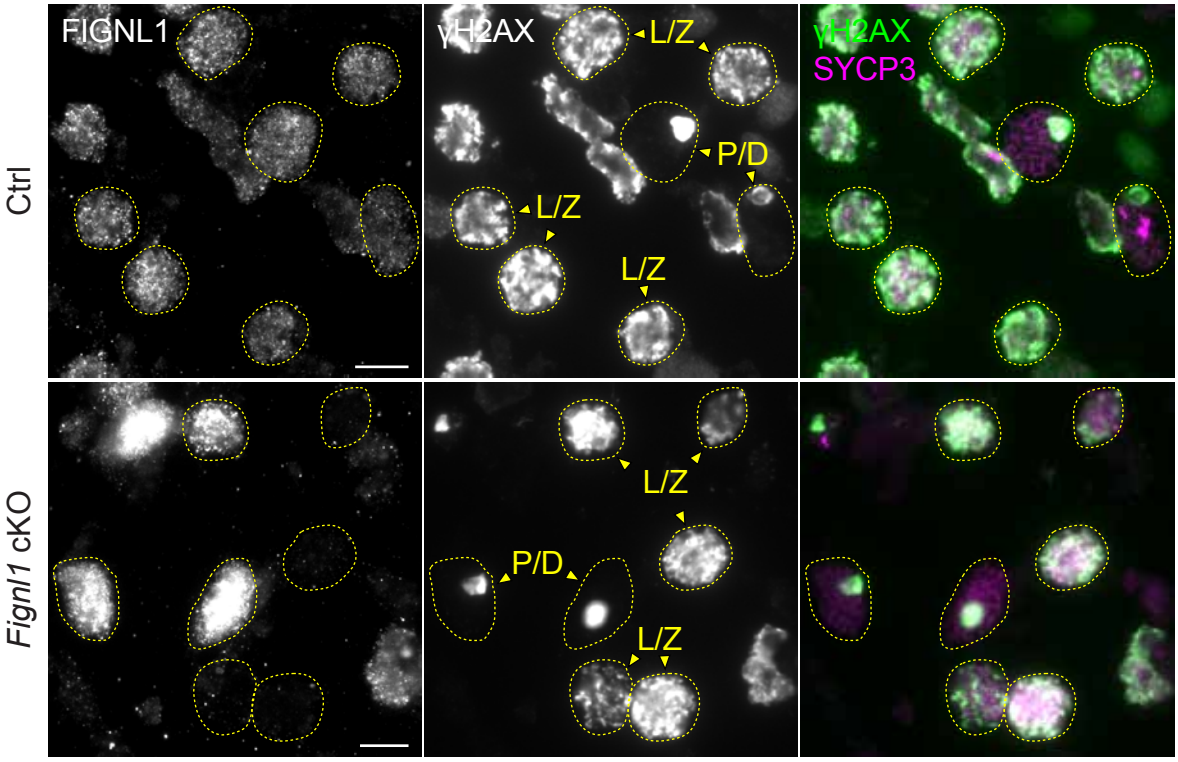

Ito et al., Supplementary Figure 2

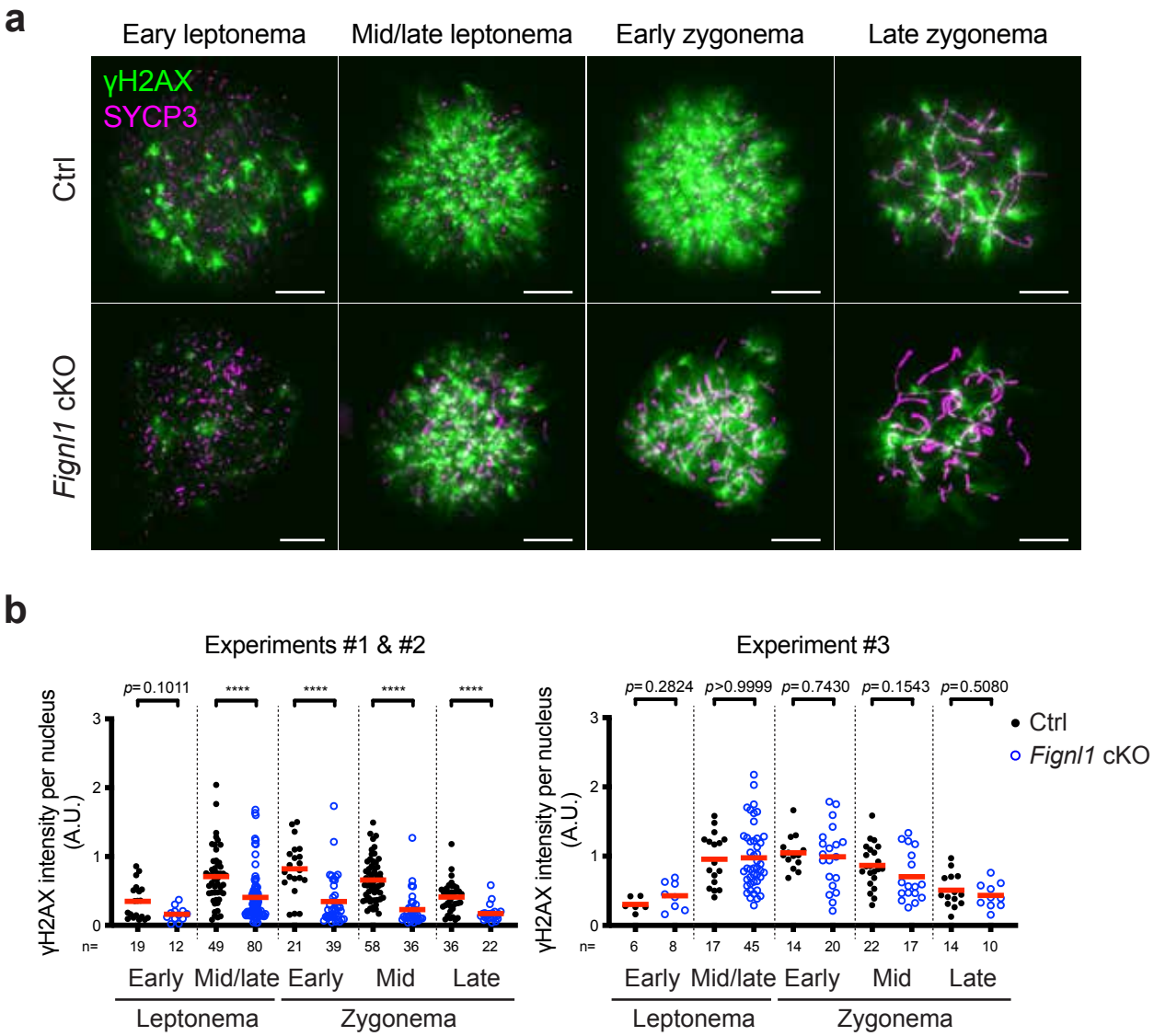

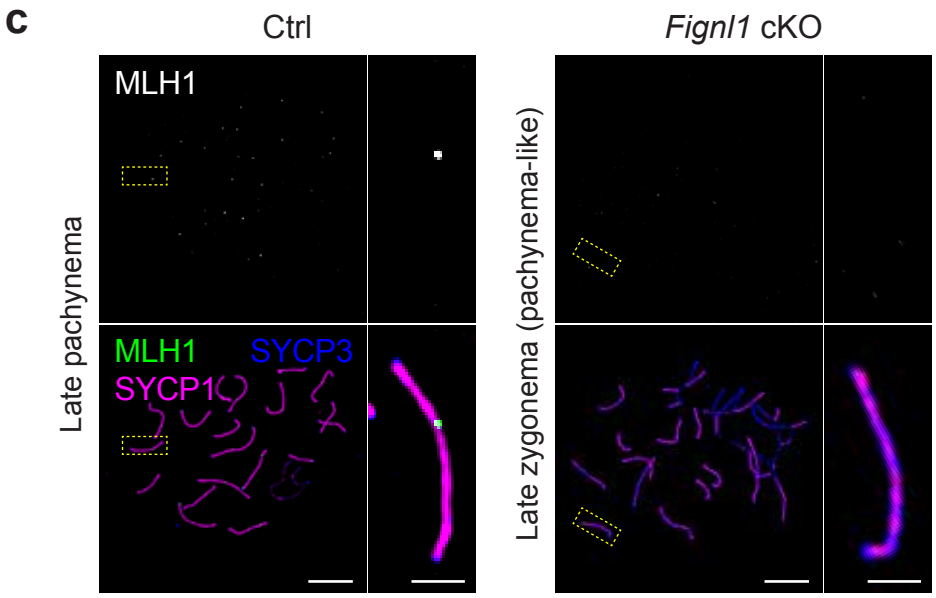

Ito et al., Supplementary Figure 3

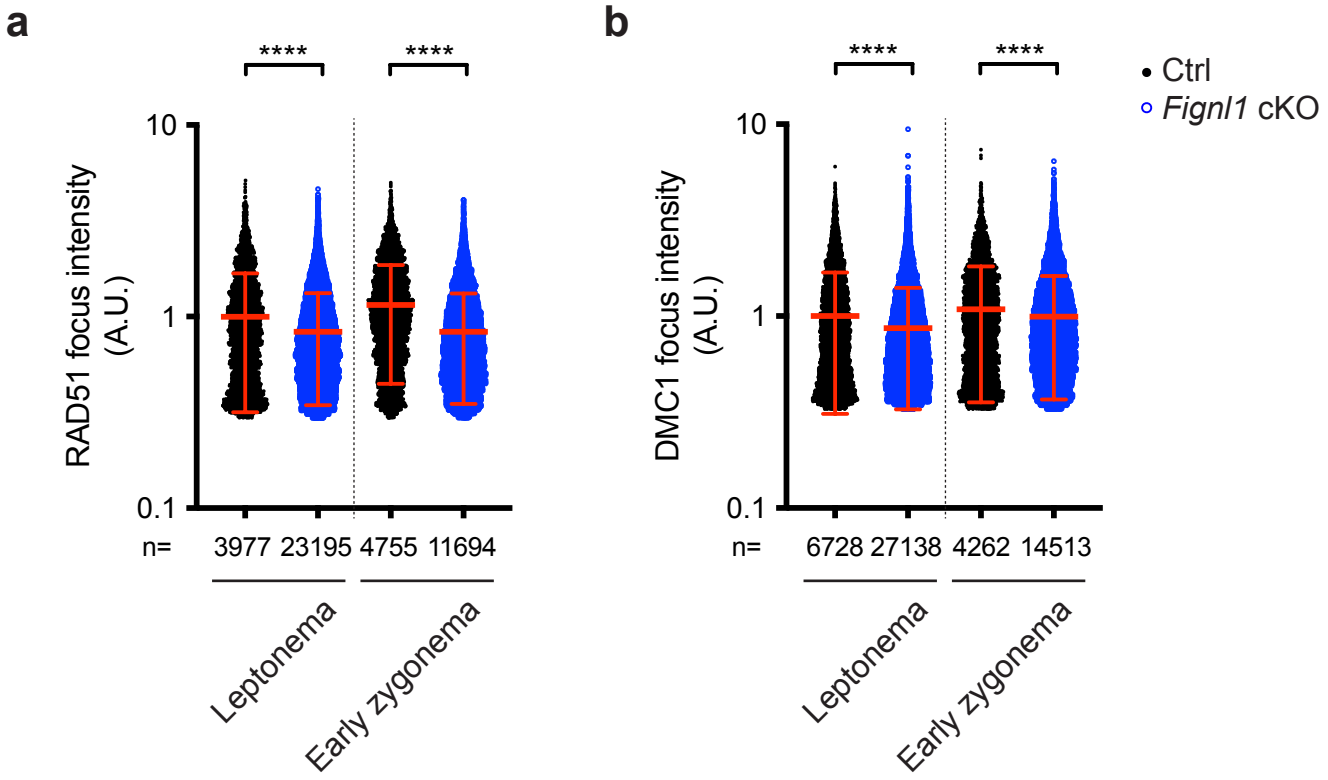

Ito et al., Supplementary Figure 4

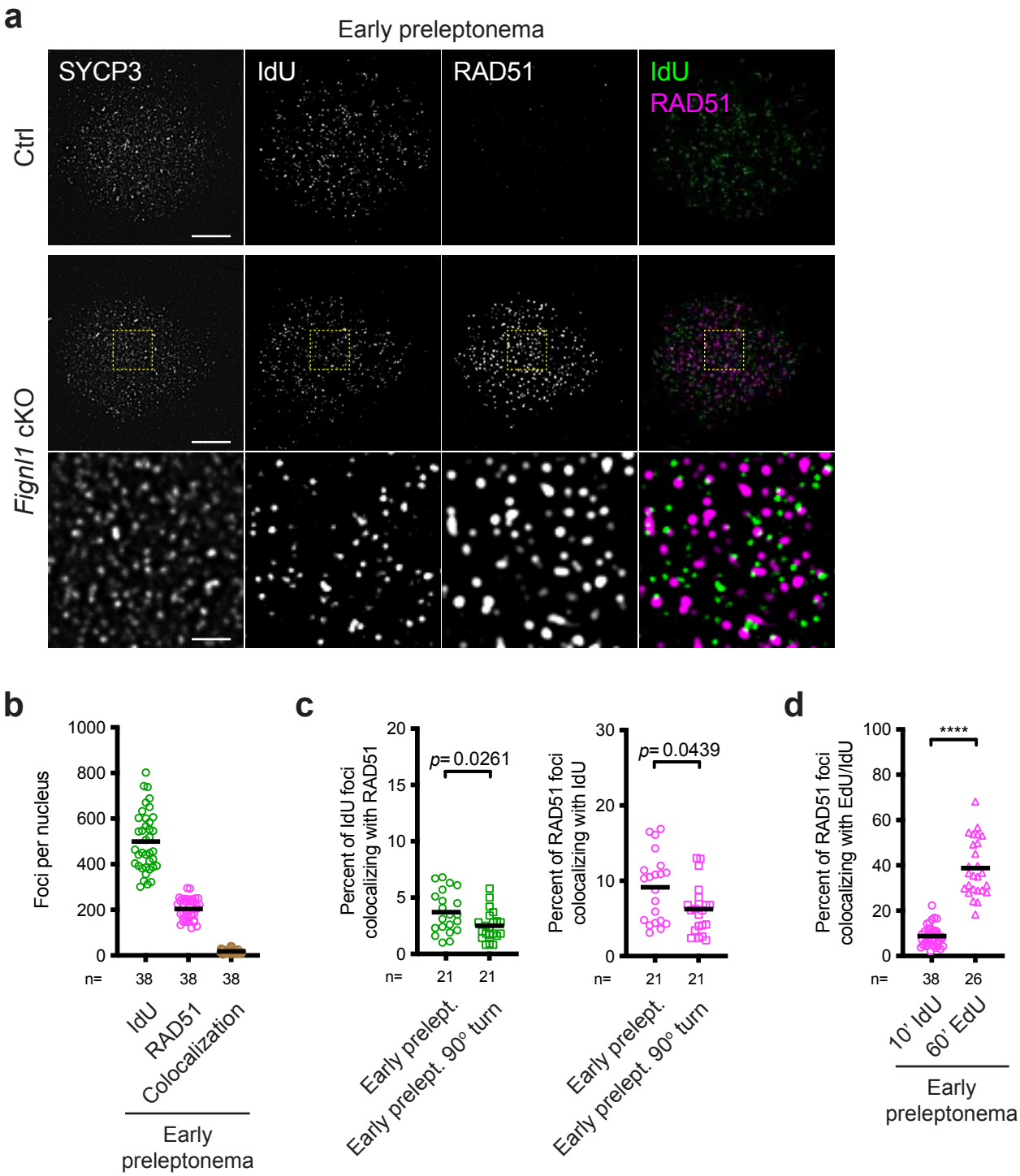

Ito et al., Supplementary Figure 5

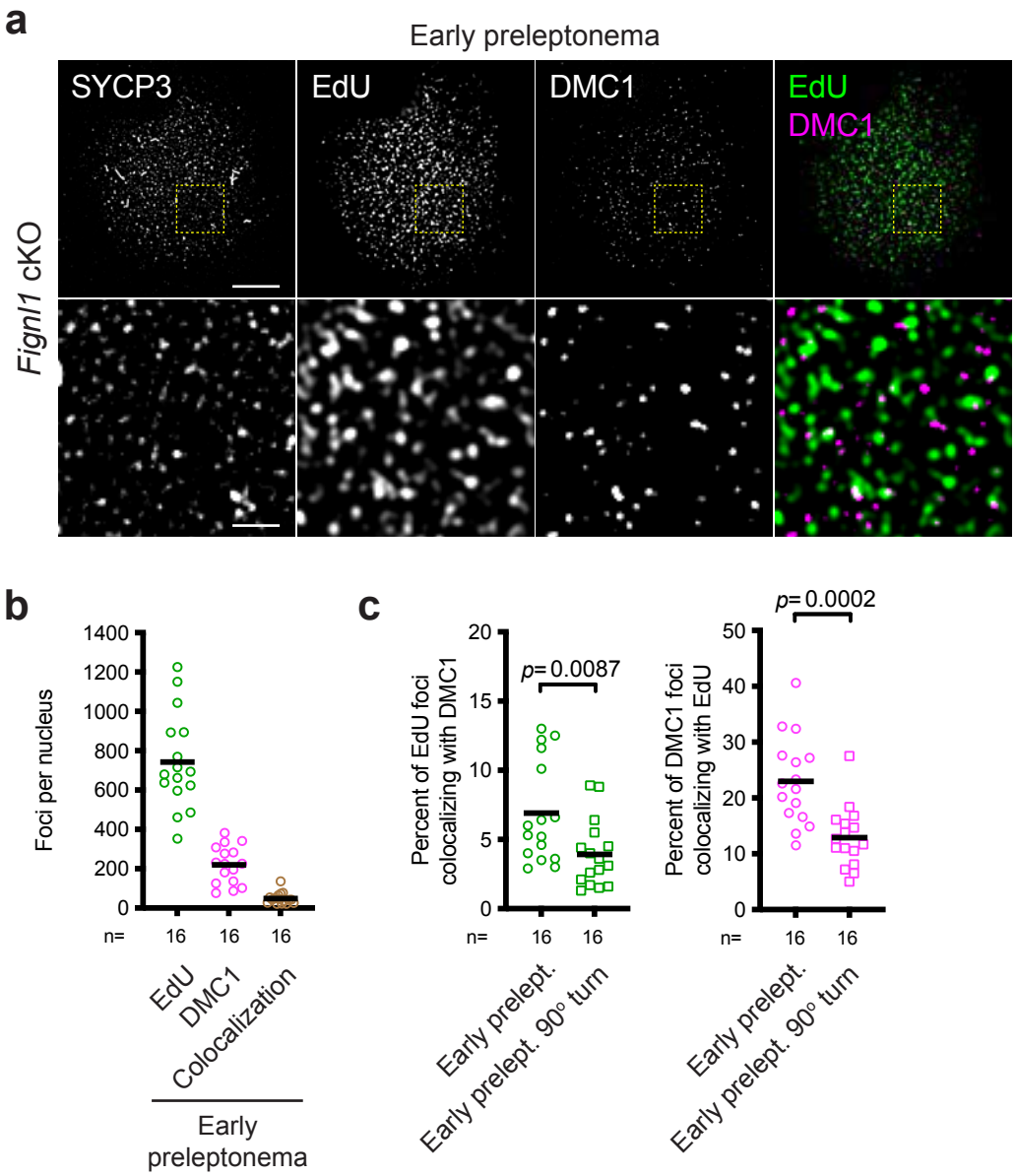

Ito et al., Supplementary Figure 6

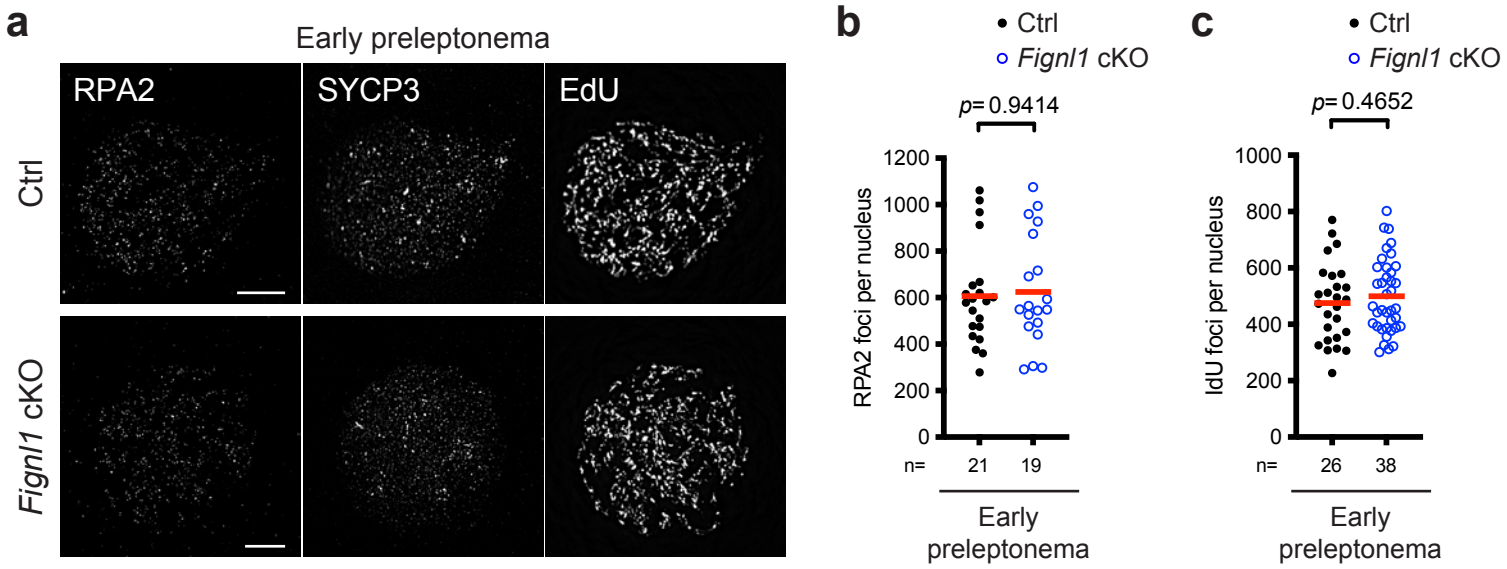

Ito et al., Supplementary Figure 7

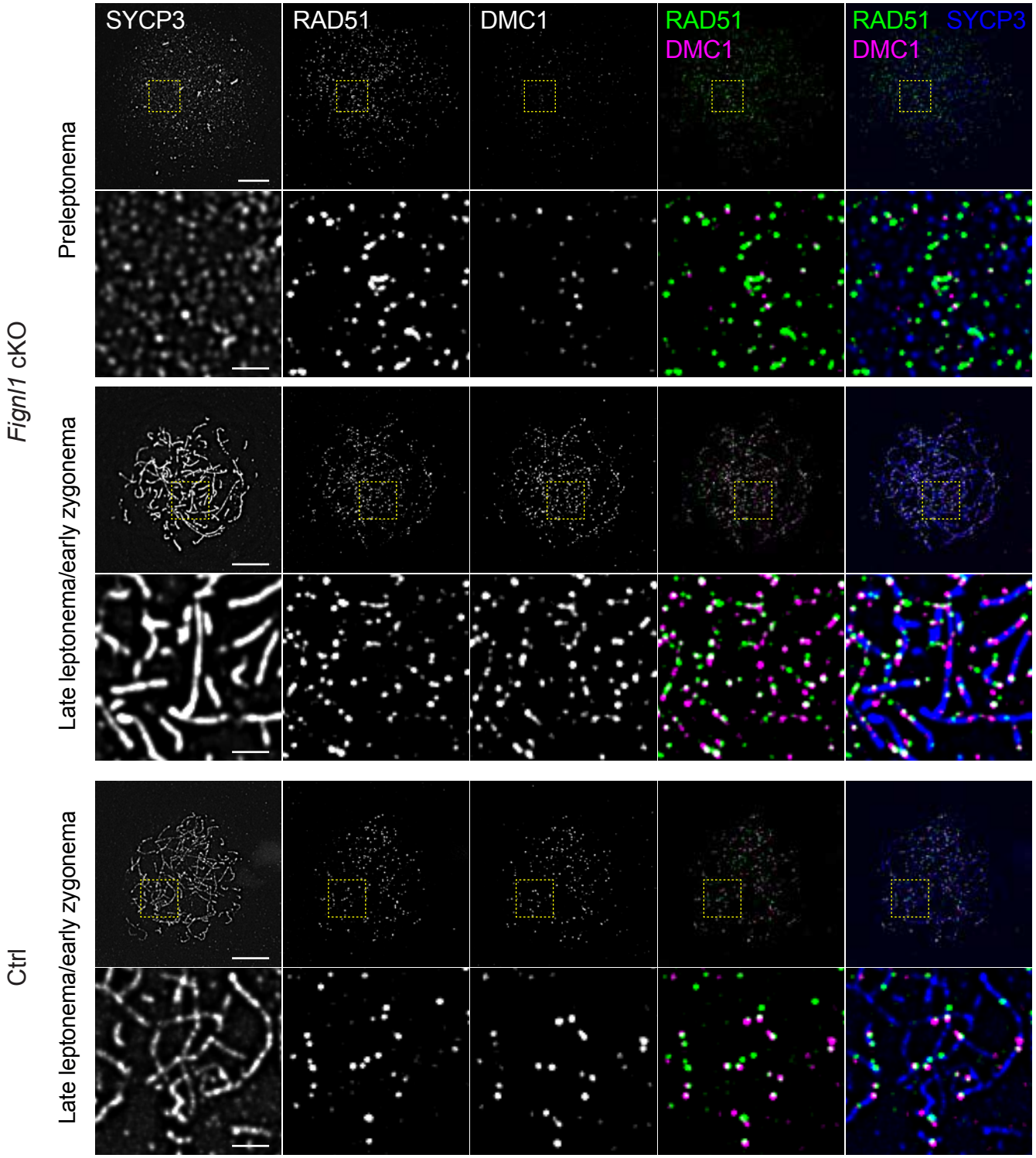

Ito et al., Supplementary Figure 8

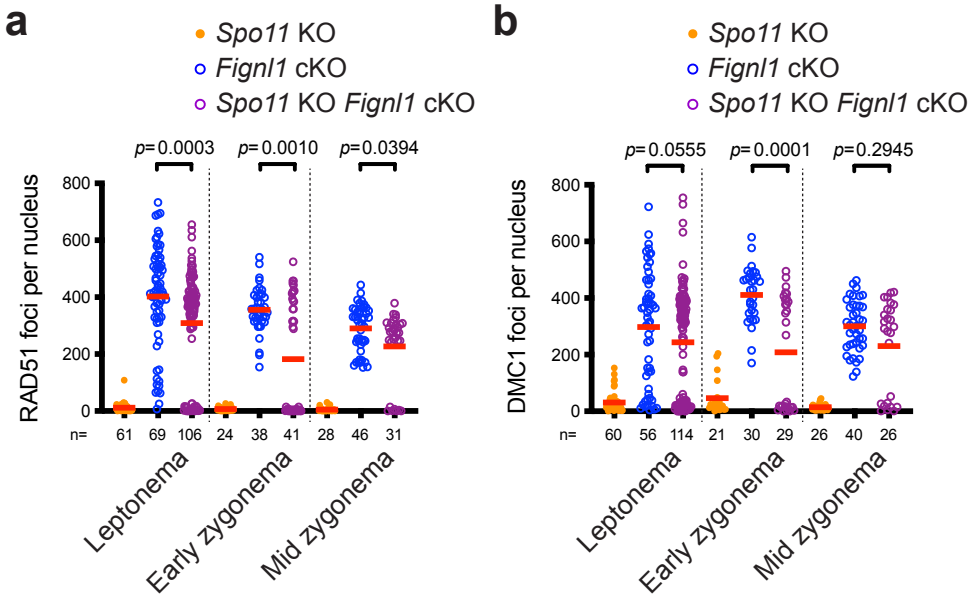

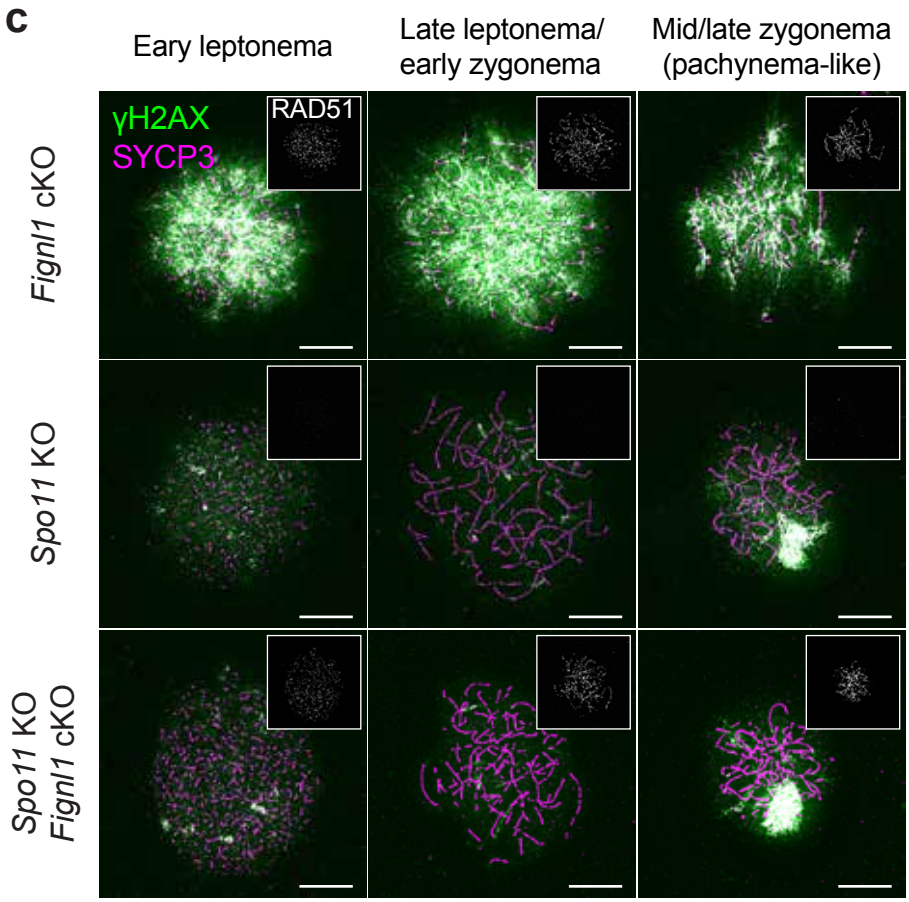

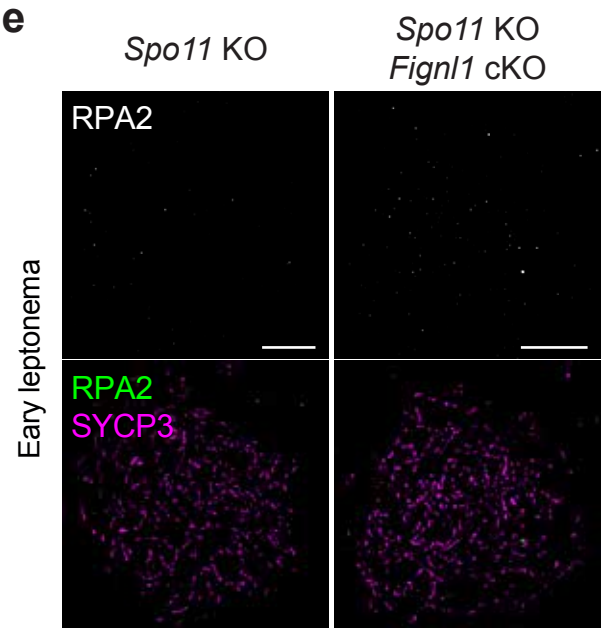

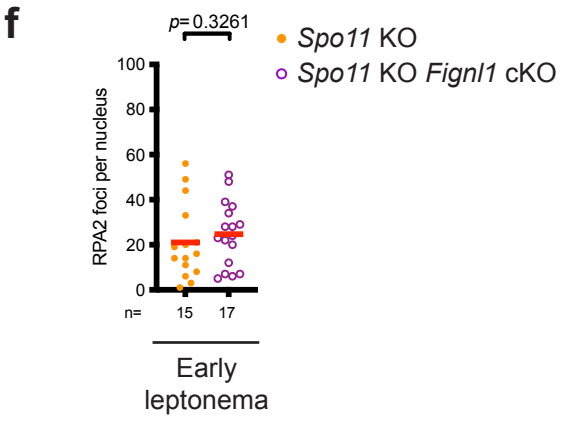

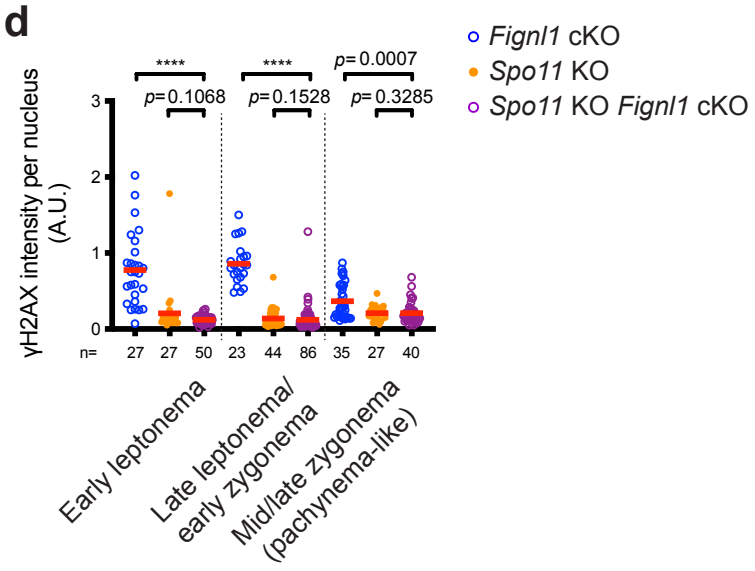

Ito et al., Supplementary Figure 9

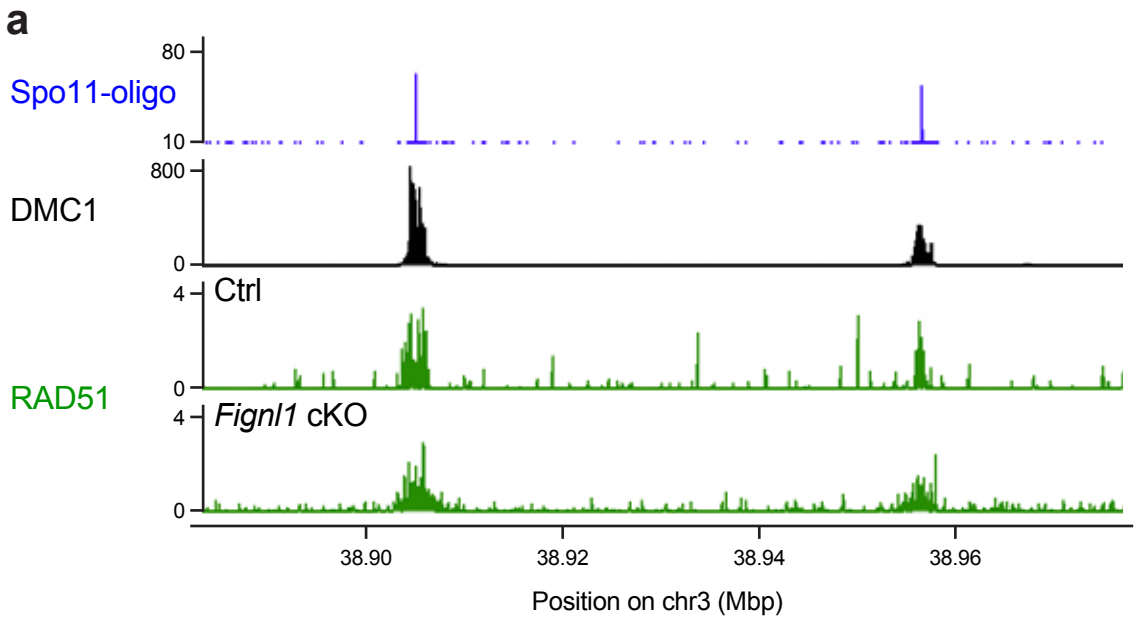

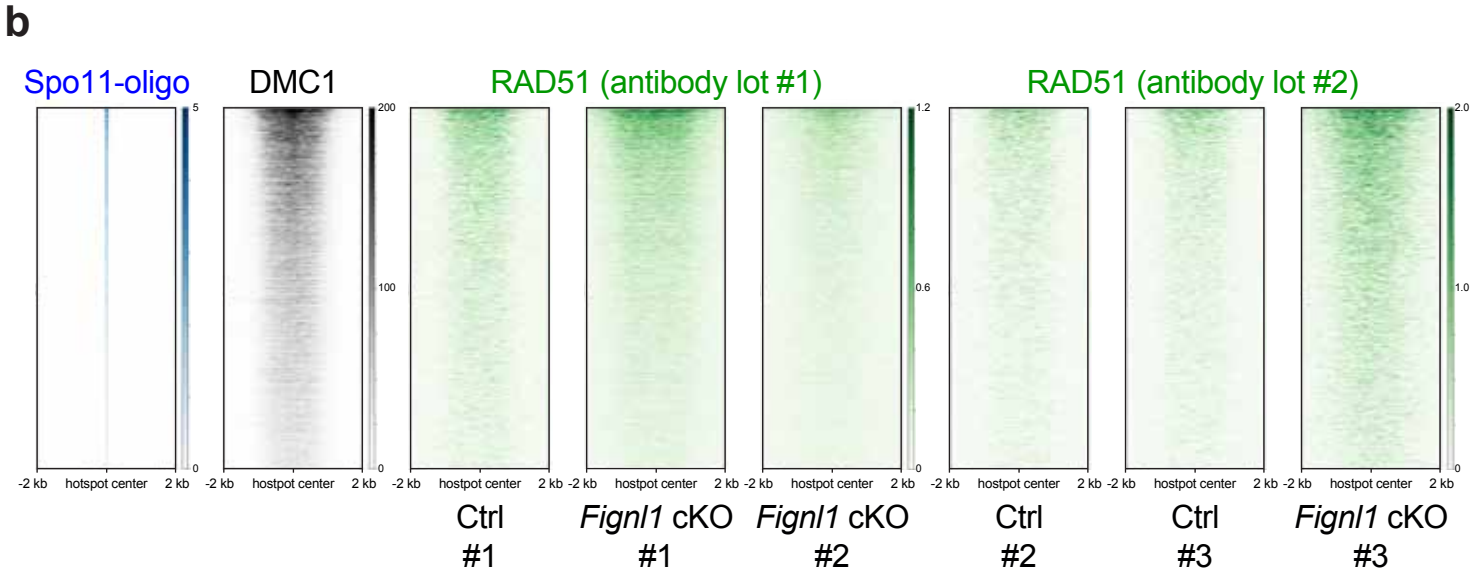

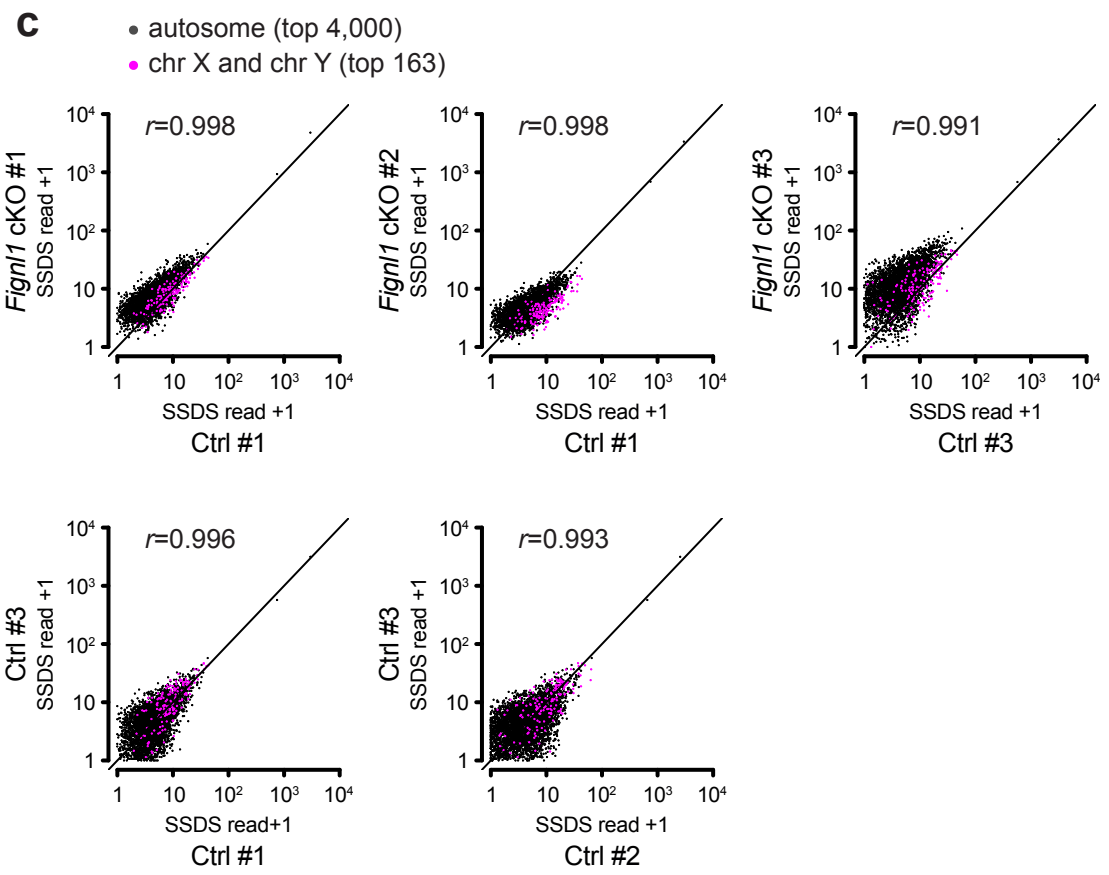

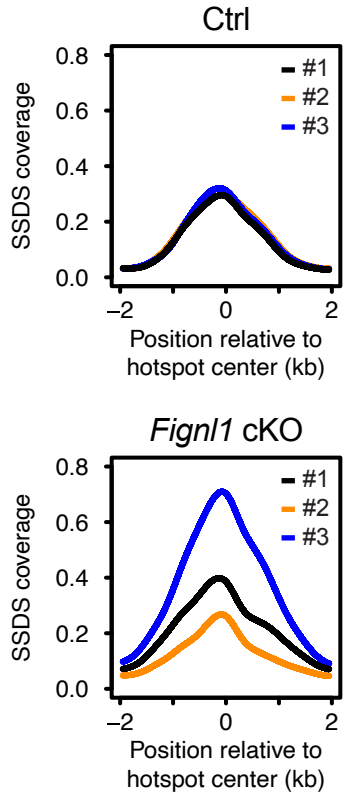

Ito et al., Supplementary Figure 10

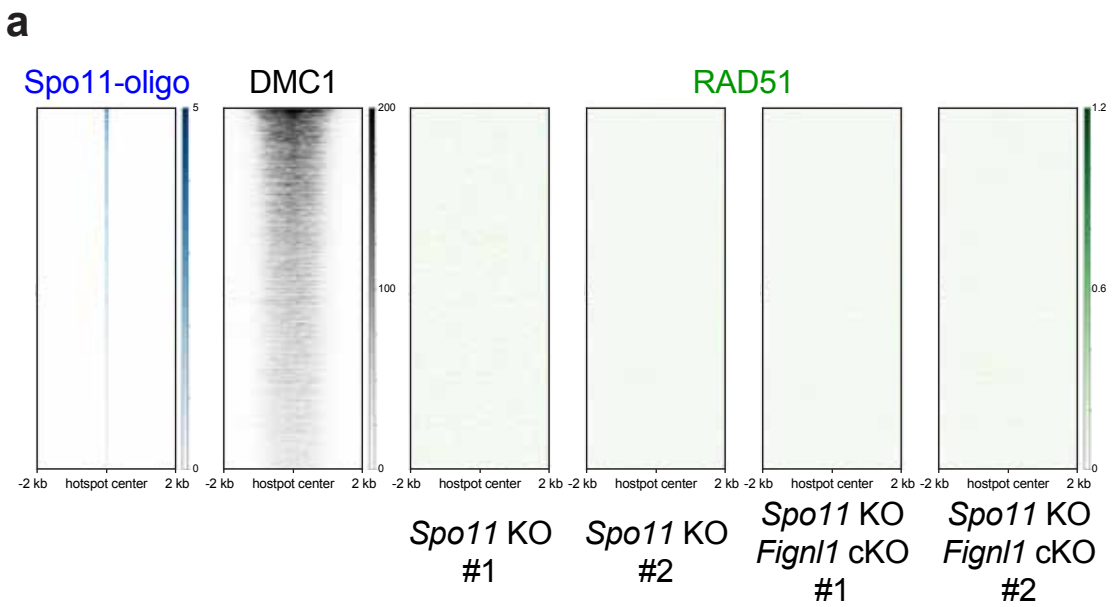

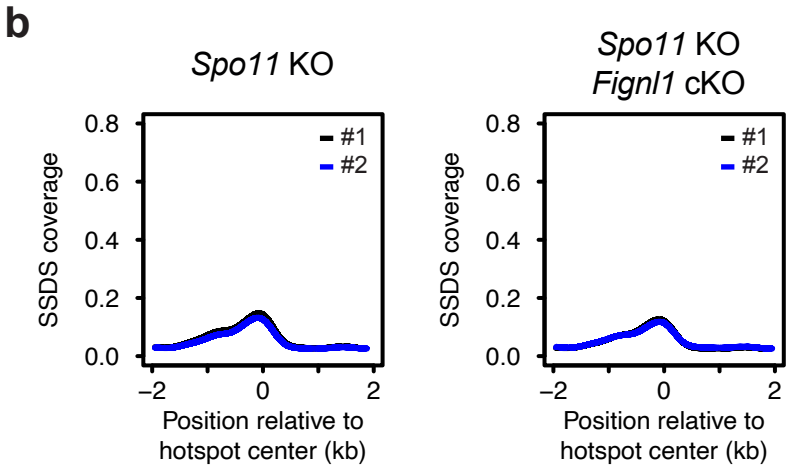

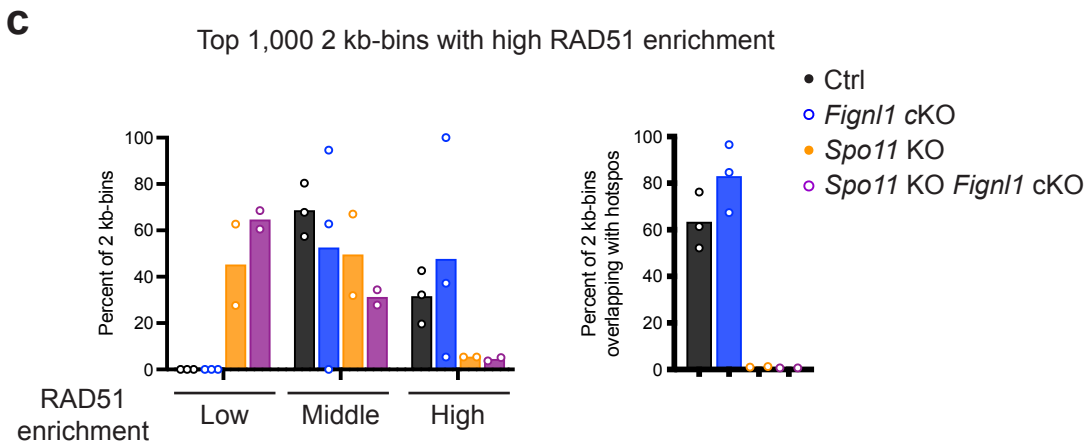

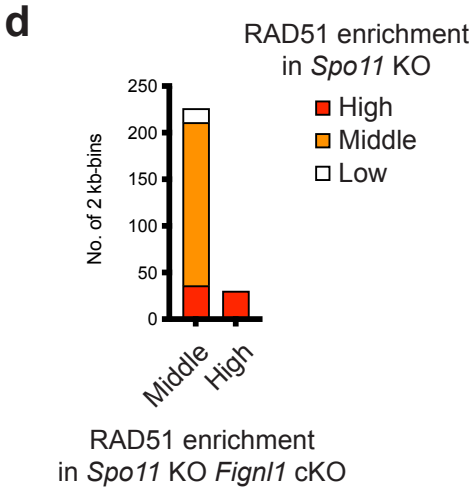

a

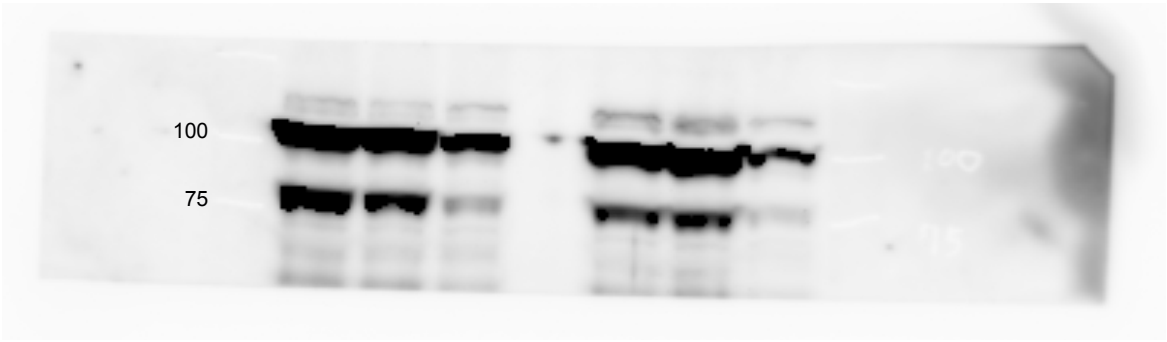

b

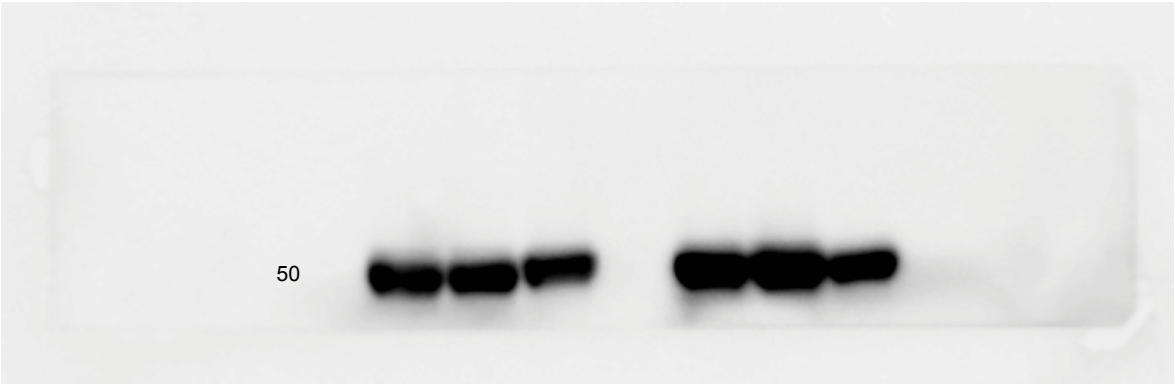

c

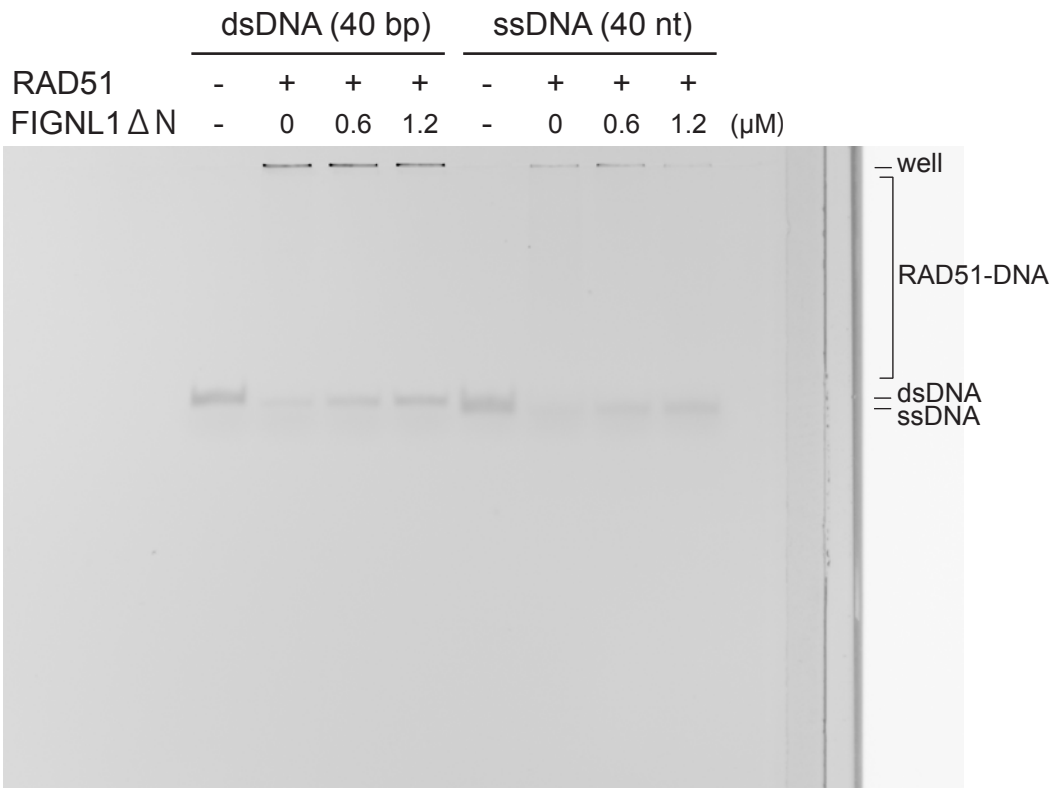

(a) An uncropped immunoblotting image for FIGNL1 shown in Fig. 1d.
(b) An uncropped immunoblotting image for α-tubulin shown in Fig. 1d.
(c) An unprocessed image of electrophoresis mobility shift assay shown in Fig. 8a.